

SPIM

Thèse de Doctorat

UFC

école doctorale sciences pour l'ingénieur et microtechniques
UNIVERSITÉ DE FRANCHE-COMTÉ

■ Numerical methods for optical forces modeling in nano-optics devices: trapping and manipulating nanoparticles

M^{me} NYHA MAJEED HAMEED

Sous la direction de Fadi BAIDA
(Femto-ST, Département de Optique)
2 juin 2016

SPIM

Thèse de Doctorat

UFC

N° 2 0 1 6

école doctorale sciences pour l'ingénieur et microtechniques
UNIVERSITÉ DE FRANCHE-COMTÉ

THÈSE présentée par

NYHA MAJEED HAMEED

pour obtenir le

Grade de Docteur de
l'Université de Franche-Comté

Spécialité : **Optique photonique**

**Numerical methods for optical forces modeling in
nano-optics devices: trapping and manipulating
nanoparticles**

Soutenue publiquement le 2 juin devant le Jury composé de :

AKJOUJ ABDELLATIF	Rapporteur	Professeur à l'Université Lille1
BENYATTOU TAHA	Rapporteur	Directeur de Recherche CNRS
BELKHIR ABDERRAHMANE	Examineur	Professeur à l'Université Mouloud Mammeri Tizi-Ouzou
PARENT GILLES	Examineur	Professeur à l'Université de Lorraine
CLEVY CÉDRIC	Examineur	MdC à l'Université de Franche-Comté
BERNAL MARIA-PILAR	Examineur	Directeur de Recherche CNRS
BAIDA FADI	Directeur de thèse	Professeur à l'Université de Franche- Comté

RAPPORT DE SOUTENANCE DE DOCTORAT
Spécialité : OPTIQUE ET PHOTONIQUE

Nom et prénom du candidat : **HAMEED Nyha**

Date et lieu de naissance : **14/04/1982 à Al Najaf (Irak)**


Date de soutenance : **02/06/2016** Heure : **14h00**

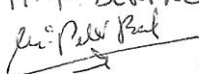
Nom du Président du jury : **Gilles Parent**


Le jury a apprécié de façon unanime la présentation de Mme Nyha Hameed. Cette présentation, bien structurée, claire et pédagogique a mis en évidence un important travail de simulation numérique en électromagnétisme permettant de déterminer les forces optiques mises en jeu dans des structures nanométriques originales. L'exposé a également permis au jury d'apprécier l'implication de Mme Hameed au sein de son unité de recherche, son souci de s'intéresser aux problématiques qui y sont développées et de proposer des simulations proches des expériences qui y sont menées. Au cours de la discussion avec le jury, Mme Hameed a répondu de façon honnête aux questions variées qui lui ont été posées.


En conséquence, le jury a attribué à Mme Hameed le titre de Docteur de l'Université de Franche Comté dans la spécialité optique et photonique avec la mention très honorable.


Taha BAWYATTOU

Abderrahmane BELKHAIR




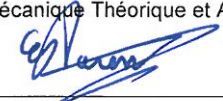


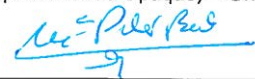

M. P. BERNAL


G. Parent

G. Parent

Fadi BAIDA


UNIVERSITÉ DE FRANCHE-COMTÉ

Noms et signatures des membres du jury

M. Abdellatif AKJOUJ (Professeur des universités) – Institut d'Électronique, de Microélectronique et de Nanotechnologie – Université de Lille 1 Rapporteur <i>Absent excuse</i> 	M. Taha BENYATTOU (Directeur de recherche CNRS) – Institut de Nanotechnologies – Institut National des Sciences Appliquées – Lyon Rapporteur 
M. Gilles PARENT (Professeur des universités) – Laboratoire d'Énergétique et de Mécanique Théorique et Appliquée – Université de Lorraine Membre 	M. Abderrahmane BELKHIR (Professeur des universités) – Laboratoire de Physique et de Chimie Quantique – Université Mouloud Mammeri de Tizi-Ouzou (Algérie) Membre 
M. Cédric CLÉVY (Maître de conférences, HDR) – Institut FEMTO-ST (Département AS2M) – Université de Franche-Comté Membre 	Mme Maria-Pilar BERNAL (Directeur de recherche CNRS) – Institut FEMTO-ST (Département d'Optique) – Université de Franche-Comté Membre 
M. Fadi BAIDA (Professeur des universités) – Institut FEMTO-ST (Département d'Optique) – Université de Franche-Comté Membre 	

Le conseil scientifique de l'École Doctorale Sciences Pour l'Ingénieur et Microtechniques a décidé que les félicitations ne seraient plus attribuées.

Fait à : BESANÇON

Le : 2 juin 2016

Dedicate

*This thesis work is dedicated to my husband **Mohammed** and my kids, **Maryam, Yousif, Fatima, Ahmed**, who have been a constant source of support and encouragement during the challenges of graduate studies and life. I am truly thankful for having you in my life. This work is also dedicated to my parents, my brothers and my sisters, who have always loved me unconditionally and whose good examples have taught me to work hard for the things that I aspire to achieve.*

Acknowledgements

Firstly, I would like to express my sincere gratitude to my advisor **Prof. BAID Fadi** for the continuous support of my Ph.D study and related research, for his patience, motivation, and immense knowledge. His guidance helped me in all the time of research and writing of this thesis. I could not have imagined having a better advisor and mentor for my Ph.D study.

Besides my advisor, I would like to thank the rest of my thesis committee: **Prof. Abdellatif AKJOUJ**, **Dr. Taha BENYATTOU**, **Prof. Gilles PARENT**, **Dr. Cédric CLEVY**, **Dr. Maria-Pilar BERNAL** and **Prof. Abderrahmane BELKHIR** for their acceptance to evaluate my thesis and their insightful comments and encouragement, but also for the questions which incited me to widen my research from various perspectives.

I would very much like to thank **Iraqi Government** and the Ministry of "**Higher Education and Scientific Research**", who have funded the thesis and **Al Muthanna University** for choosing me for this PhD position.

Also, it is a big honor to be a part of FEMTO-ST Institute. I'm very thankful to all the members of the community and to the Optics Department in particular.

Last but not the least, I would like to thank my family: my parents, my brothers, my sisters and to my husband and my kids for supporting me spiritually throughout writing this thesis and my life in general.

Abbreviations list

BNA	Bowtie Nanoaperture Antenna
BNAT	Bowtie Nanoaperture Antenna Tip
DA	Diabolo nano Antenna
EM	Electromagnetic field
FDFD	Finite Difference Frequency Domain method
FDTD	Finite Difference Time Domain method
FIB	Focused Ion Beam
MST	Maxwell Stress Tensor
Np	Nano particle
Nps	Nano particles
PML	Perfectly Matched Layer
RW	Resonance Wavelength
SNOM	Scanning Near-field Optical Microscope
SEM	Scanning Electron Microscopy

Contents

1	General Introduction	15
2	Finite Difference Frequency Domain	19
2.1	Introduction	19
2.2	Motivations for using FDFD method	20
2.3	Maxwell Equations	23
2.3.1	Topological equations (without source)	24
2.3.2	Metric equations (equations with source):	25
2.4	Matrix Form of Maxwell Curl Equations :case of eigenmode calculations . .	26
2.5	Validation of FDFD matlab code	36
2.5.1	Test 1: Step-Index Circular Optical Fiber (SIOF)	36
2.5.2	Test 2: Air-Hole-Assisted Optical Fiber (AHAOF)	40

2.6	Application of our FDFD code	41
2.6.1	Study of the "slot waveguide"	42
2.6.2	Study of the "ridge waveguide"	44
2.7	Conclusions	46
3	Electromagnetic Force	49
3.1	Introduction	49
3.2	Introduction of optical tweezers	50
3.3	Mechanical action of light and gradient force	57
3.4	Basics of the electromagnetic Force	59
3.4.1	Electromagnetic force per unit volume: Formulation of MST ex- pression	61
3.4.2	Total force on a particle included in a volume V	64
3.4.3	The electro and magneto statics force	67
3.5	Numerical simulation tool (FDTD)	74
3.5.1	Principle of FDTD	74
3.5.2	3D Illustration of FDTD	75
3.5.3	Stability criteria	80

3.5.4	Dispersion	81
3.5.5	Boundary conditions: PML principle	83
3.6	Validation of our code	85
3.6.1	Test: Optical force calculations of dielectric nanoparticle	85
3.7	Conclusions	91
4	Application 1: Optical tweezers based on fibred Bowtie Nanoaperture Antenna (BNA)	93
4.1	Introduction	93
4.2	Bowtie Nanoaperture Antenna properties	95
4.3	Bowtie Nanoaperture Antenna design on fiber SNOM tip	96
4.4	Experimental set-up	100
4.5	Numerical study	101
4.5.1	Study of large particle trapping $R = 250$ nm	102
4.6	Experimental vs numerical results	109
4.7	Comparison between conventional metal coated SNOM and BNAT as optical tweezers	111
4.8	Study of small particle trapping	114
4.9	Conclusion	118

5	Application 2: Optical tweezers based on Diabolo Antenna (DA)	119
5.1	Introduction	119
5.2	Diabolo nano-Antenna (DA) properties	121
5.3	Optimization of the diabolo antenna geometry	122
5.4	Optical force calculations with the diabolo antenna	129
5.4.1	Optical force on self-suspended diabolo antenna	129
5.4.2	Optical force exerted by a diabolo antenna on nanoparticle	130
5.5	Conclusion	140
6	General Conclusion and perspectives	141
	Bibliographie	145

List of Figures

2.1	(a): schema of the step-index dielectric cylindrical optical fiber. The radius is set to $R = 3\mu m$, the cladding index is $n_1 = 1$ and the core index is $n_2 = 1.45$. (b) N-order FDTD results showing a map of the spectral density as a function of the propagation constant. The white dashed horizontal line correspond to the operation wavelength ($\lambda = 1.5\mu m$). Intersections with high spectral density give the excited mode propagation constants.	22
2.2	FDFD results giving the effective index of the first $N = 4$ guided modes inside the fiber at $\lambda = 1.5\mu m$	23
2.3	Yee - mesh 3×3 in two dimensions. a)TE mode. b)TM mode	29
2.4	Block diagram of FDFD implementation	35
2.5	Scheme of Step-Index Circular Optical Fiber	37
2.6	Subgridding Technique.	37
2.7	(a) Convergence studies. (b) Relative errors ratio	38

2.8	Electric field distribution for different modes index of step-index circular optical fiber	39
2.9	Relative error of uniform and nonuniform mesh.	39
2.10	Scheme of Air-Hole-Assisted Optical Fiber	40
2.11	Magnetic field distribution of fundamental mode index of Air-Hole-Assisted Optical Fiber.a) Our calculations results. b) Zhu et al [1] results.	41
2.12	Magnetic field distribution for different modes index of Air-Hole-Assisted Optical Fiber	41
2.13	a)Scheme of slot waveguide.b)Electric field distribution of fundamental mode index of slot waveguide	43
2.14	a)Scheme of lithium niobate ridge waveguide. b) The refractive index variations along the vertical direction of the lithium niobate ridge waveguide.	45
2.15	a)Electric field distribution of fundamental mode for lithium niobate ridge waveguide index gradient.b)Electric field distribution of fundamental mode for lithium niobate ridge waveguide without index gradient.c)	46
2.16	Differential between index gradient and non gradient	47
3.1	Schema of optical trapping system of Mie and Rayleigh particles in water by a single-beam gradient force radiation-pressure trap [2]	51

3.2	a) Tungsten probe of an apertureless near-field microscope. b) Z-component of the force experienced of by the sphere versus the distance between the tip and the sphere. c) Force along-z experienced by the sphere as a function of the lateral position of the probe. The sphere is at the origin.[3].	52
3.3	Trapping potential of a particle ($d = 10\text{nm}, \epsilon = 2.5$) in the vicinity of the tip. (a) Potential energy surface in the (xz) plane (the tip is indicated by the shadow on the bottom plane). (b),(c) Normalized potential energy evaluated along the x and z directions, respectively[4].	53
3.4	(a) Schematic of the coaxial plasmonic aperture and the potential well in the xOy transverse plane. (b) Transverse trapping potential on a 10 nm dielectric placed at 20 nm away from the coaxial apertur. (c) Cross sections of the transverse optical trapping potential (U_{xy}) along $x = 0$ nm and $y = 67$ nm. The trapping potential full-width at half-maximum is indicated in each direction [5].	55
3.5	Schema of the nanoscale double-hole. b) SEM image of the double-hole on Au film taken normal to the surface. c) Optical trapping of 12 nm silica spheres using a double nanohole at 15 nm tip separation [6].	56
3.6	Scattering and gradient forces created by non homogeneous optical illumination on a dielectric particle.	57
3.7	(a) Optical trapping. (b) Laser guidance.	58
3.8	A dielectric particle polarization in accordance with: (a,b) uniform field (c,d) non uniform electric field; c) and d) shows that at change of the electric field sign the direction of the gradient force does not change.	60

3.9	Numerical simulation of a dielectric particle is illuminated with:a) Plane wave. b) Gaussian Beams. c) Off-centered spherical particle illuminated by Gaussian Beams.	61
3.10	A particle included in a volume V	65
3.11	Hemisphere enclosing one of the two charge to find the force on charge enclosed.	72
3.12	3D Yee discretization schema (unit cell in Cartesian coordinates).	76
3.13	Circulation of \vec{E} around \vec{H}	79
3.14	Calculating \vec{H} at time $n\Delta t$ and \vec{E} at time $(n+0.5)\Delta t$, where n is an integer.	80
3.15	Principle of perfectly matched layers (PMLs) operating in medium.	85
3.16	A microlens biconvex, curvature radius $r = 4\mu m$, thickness $t = 1\mu m$ and index $n_{lens} = 2$ is placed in front of a Gaussian beam to accentuate the focus on the Np.	86
3.17	a)3D map of the optical force F_x in the xOz plane in front of the lens. b)cross-section made over the figure (a), along the Ox-axis for $d=2513$	88
3.18	a)3D map of the optical force F_z in the xOz plane in front of the lens. b)cross-section made over the figure (a), along the Ox-axis for $d=2513$	89
3.19	Map of the force amplitude (in color level) exerted by the focused light passing through the microlens. The white arrows give the force direction and amplitude. The black square shows the trapping zone.	90

3.20	(a) Schema of a biconvex microlens with sphere surrounded by different boxes. (b),(c),(d) values variations of F_x, F_y, F_z respectively.	91
4.1	Schema of the experimental configuration of BNA tip. (b) Experimental time traces showing the transmission through the BNA at 1064 nm (red curved) and the fluorescence from the trapped bead (blue curve). The increase in both transmission and fluorescence corresponds to the trapping of a single 20 nm PS bead.[7]	94
4.2	(a-d) SEM micrographs of the fiber-integrated nano-tweezer based on a BNA fabricated at the apex of a SNOM tip: side view of the fiber metal-coated SNOM tip (a) before and (b) after initial FIB processing to flatten the tip apex: the rough metallic surface of the rounded apex is milled from the side to be finely polished. (c) and (d) side and top views of the BNA at the tip apex, respectively (obtained by FIB milling from the top) [8]. .	97
4.3	(a)Schema of the end part of a polymer tip with half angle cone of 14° and apex radius of 480 nm. The polymer has an optical refractive index $n = 1.52$ and the tip is supposed to be coated by a 100 nm -thick aluminum layer. The permittivity of the latter is defined with a Drude model where the plasma frequency is set to $\omega_p = 1.973 \times 10^{16}$ and the dumping term to $\Gamma = 2.198 \times 10^{14}$ rad/s. The geometrical parameters of the BNA are : $D_x = 135$ nm, $D_y = 165$ nm and the gap $g = 45$ nm. b) Calculated near-field (at 15 nm above the BNA) electric intensity enhancement of the BNAT shows a maximum of 90 at $\lambda \simeq 1064$ nm.	98

-
- 4.4 (a,b) Simulation of the distribution of optical electric field (amplitude) in a transverse plane (perpendicular to the tip axis) taken 15 nm away from the tip ($\lambda = 1064$ nm), for two perpendicular polarization directions of the incoming waves (see arrows in insets). (c,d) Far-field experimental images of the fiber tip output for two perpendicular polarization directions of the in-fiber illumination (BNA on and off resonance, see arrows in the insets)[8]. 99
- 4.5 Fifth root of the electric field intensity distributions in longitudinal planes : xOz and yOz passing through the tip axis. 100
- 4.6 Schema of the experimental setup used to the visualization of the particle trapping with the BNAT. Two illumination sources are used: first one thanks to laser @ $\lambda = 1064$ nm that is injected inside the fiber to induce the BNA resonance. The second is a white-light source used to directly illuminated the bowl that contains the suspended particles in water. The visualization of the particle position is obtained through a conventional optical system combining a microscope objective with a CCD camera. . . . 102
- 4.7 Calculated optical forces for latex nanoparticle of radius $R = 250$ nm. (a) Distribution of the force amplitude (0.8 power in order to better see the large variations at small distances) in the yOz plane as a function of the BNAT-latex particle distance d .(b) same as (a) but in the xOz plane. . . . 103
-

4.8	(a) is map of the optical force in the plane located at $d = 45$ nm from the tip . The arrows indicate the tangential force component in xOy plane while the color level is associated with the vertical component. (b) Is cross-sections made over the Figures (a), along the Oy -axis which corresponds to the direction of the BNA metallic arms (i.e. to the incident beam polarization direction that induces the BNA resonance).	105
4.9	(a) is map of the optical force in the plane located at $d = 195$ nm from the tip . The arrows indicate the tangential force component in xOy plane while the color level is associated with the vertical component. (b) Is cross-sections made over the Figures (a), along the Oy -axis which corresponds to the direction of the BNA metallic arms (i.e. to the incident beam polarization direction that induces the BNA resonance).	106
4.10	Calculated potential well for latex nanoparticle of radius $R = 250$ nm. (a) The associated potential showing a 180 kT well at $d = 120$ nm in yOz plane. (b) same as (a) but in the xOz plane.	107
4.11	Archimedes' principle	108
4.12	Time evolution of the trapping process showing four different positions of the latex particle when the BNA resonates.	110
4.13	(a) Numerical results of vertical force of $R = 250$ nm as a function of the BNAT-particle distance when the latter moves along the tip axis. Smaller values of d are considered in order to quantify the pulling force near the tip apex ($F = 12$ pN/100mW @ $d = 45$ nm). (b) the corresponding potential showing a well of 300kT at $d = 45$ nm.	112

-
- 4.14 (a) Calculated near-field (at 15 nm above the HAT) electric intensity enhancement of the HAT in two case:1) HAT =56 nm blue solid line not show any resonance.2) HAT=150 nm shows a maximum of 0.023 at $\lambda \simeq 1064$ nm. (b) Numerical results of vertical force of $R = 250$ nm as a function of the cylindrical aperture-particle distance when the latter moves along the tip axis. Green curve corresponds to same opened area as the BNA, blue curve corresponds to same resonance of BNA 113

- 4.15 Calculated optical forces for latex nanoparticle of radius $R = 100$ nm. (a) bottom : distribution of the force amplitude (0.8 power in order to better see the large variations at small distances) in the yOz plane as a function of the BNAT-latex particle distance d . (a) top : the associated potential showing a 100 kT well at $d = 120$ nm. (b) same as (a) but in the xOz plane.(c) vertical force as a function of the BNAT-particle distance when the latter moves along the tip axis. Smaller values of d are considered in order to quantify the pulling force near the tip apex ($F = 3.5$ pN/100mW @ $d = 45$ nm). (d) the corresponding potential showing a well of 140kT at $d = 45$ nm. 115
-

-
- 4.16 Calculated optical forces for latex nanoparticle of radius $R = 30$ nm. (a) bottom : distribution of the force amplitude (0.8 power in order to better see the large variations at small distances) in the yOz plane as a function of the BNAT-latex particle distance d . (a) top : the associated potential showing a 40 kT well at $d = 120$ nm. (b) same as (a) but in the xOz plane.(c) vertical force as a function of the BNAT-particle distance when the latter moves along the tip axis. Smaller values of d are considered in order to quantify the pulling force near the tip apex ($F = 1.2$ pN/100mW @ $d = 105$ nm). (d) the corresponding potential showing a well of 47kT at $d = 105$ nm. 116
- 4.17 (a) is map of the optical force in the plane located at $d = 45$ nm from the tip of $R = 100$ nm. The arrows indicate the tangential force component in xOy plane while the color level is associated with the vertical component. (b) is cross-sections made over the figure (a), along the Oy -axis which corresponds to the direction of the BNA metallic arms (i.e. to the incident beam polarization direction that induces the BNA resonance). 117
- 4.18 (a) The optical force in the plane located at $d = 105$ nm from the tip of nanoparticle with $R = 30$ nm where the arrows indicate the tangential force component in xOy plane. (b) is cross-sections made over the figure (a), along the Oy -axis which corresponds to the direction of the BNA metallic arms (i.e. to the incident beam polarization direction that induces the BNA resonance). 117
-

5.1	(a) SEM of pairs of gold nanoblocks with 5 nm gaps. (b) Calculated near-field distributions near a model gold nanoblock pair at an 800-nm incident wavelength. Block size= $80 \times 80 \times 30$ nm and gap distance = 5 nm for xz plane yz plane on the pair as shown to the left side of panels respectively. (c) Optical plasmonic trapping of 350 nm polystyrene particles with nanoblock pairs [9].	120
5.2	(a) 3D view BNA and (b) its complementary DA nano antenna. (c, d) Physical principles of EM field confinement appears in the bowtie nanoaperture and diabolo nanoantennas.	122
5.3	Near-field electric and magnetic spectral responses of Diabolo nanoantenna (DA) and its complementary structure Bowtie nanoaperture antenna (BNA) .(a) Perfect metal.(b) Real metal.	123
5.4	(a)Magnetic and (b)Electric spectral responses as a function of length D with fixed value of $G = 25$ and $T = 20$ nm of a gold DA immersed in water.	124
5.5	(a)Magnetic and (b)Electric spectral responses as a function of gap G with fixed value of $D = 135$ and $T = 20$ nm of a gold DA immersed in water.	125
5.6	(a)Magnetic and (b)Electric spectral responses as a function of gap T with fixed value of $D = 135$ and $G = 25$ nm of a gold DA immersed in water.	125
5.7	The relation between RW/enhancement factor and DA geometrical parameters a)DA length D . b)DA gap G . c)DA thickness T	126
5.8	(a)Magnetic and (b) electric spectral responses of a gold DA with $D = 135$ nm, $G = 25$ and $T = 20$ nm immersed in air (black dashed lines) and in water (red solid lines).	127

5.9	(a),(b) Show the magnetic and electric field distributions at resonance immersed in water ($\lambda_{res}^{water} = 1458 \text{ nm}$) along a transverse (xOy) plane and (c),(d),(e),(f) in the longitudinal planes (xOz,yOz) at 5 nm above the DA.	128
5.10	Numerical results of the optical force of DA immersed in air (black dashed lines) and in water (blue solid lines) as a function of the wavelength in two cases: 1) DA on resonance 2) DA off resonance.	130
5.11	Schematic of the diabolo nano-antenna D is the total length in both x and y directions, G is the gap size and T is the thickness in z direction onto a glass substrate and Np as sphere with radius R surrounded by water.	131
5.12	Magnetic and electric spectral near-field responses of a gold DA with $D = 135 \text{ nm}$, $G = 25$ and $T = 20 \text{ nm}$ deposited on a glass substrate and immersed in water.	131
5.13	Map of vertical force numerical results presented as a function of the DA-to-Np distance S and the wavelength illuminations λ for different Np radius: a) $R=30 \text{ nm}$. b) $R=40 \text{ nm}$. c) $R=55 \text{ nm}$. e) $R=70 \text{ nm}$. f) $R=90 \text{ nm}$. d) Show the potential well of Np with $R=55 \text{ nm}$.	134
5.14	Map of vertical force numerical results presents as a function of the Np radius R and the wavelength illuminations λ for different DA-to-Np distance S : a) $S=15. \text{ nm}$ b) $S=55. \text{ nm}$ c) $S=95. \text{ nm}$ d) $S=155 \text{ nm}$.	136
5.15	Map of vertical force numerical results presents as a function of Np radius and DA-to-Np distance S for different operation wavelengths: a) $\lambda = 1397 \text{ nm}$ b) $\lambda_{res} = 1523 \text{ nm}$ c) $\lambda = 1800 \text{ nm}$.	137

- 5.16 Numerical results of vertical force presents as a function of the size of the N_p placed at 15 nm far from the DA along its axis. One notice that the permittivity of the N_p is modeled with a subgridding technique in order to accurately describe its geometry. 138
- 5.17 (a),(b),(c) and (d) The potential results of different N_p s radii (50,55,60,65) nm shows three case of the optical trapping with different operation wavelength:1) Red solid lines are trapping at distance.2) Green solid lines are trapping at contact. 3) Blue solid lines are no trapping (radiation pressure). 139
-

List of Tables

2.1	Fundamental mode index for step-index circular optical fiber	38
2.2	Fundamental mode index for air-hole-assisted optical fiber	41
2.3	The effective indices of the first five guided modes of the slot waveguide . .	44
2.4	The effective indices of the first five guided modes of the ridge waveguide .	45

Chapter 1

General Introduction

Light has been a topic of studies for a long time, reaching back to the philosophers in ancient Greece discussing the properties of sight. The expansion of light as a science accelerated in the Islamic world around 1000 AD, and continued in Europe with the renewal of science, philosophy and art through the renaissance. In the 17th century, methodological studies of optical phenomena lead to the development of the particle and wave theories of Huygens and Newton. By the end of the 19th century, optics had been found to be electromagnetic radiation, and with Maxwells equations, the noticeable optical phenomena of the time could be explicated. However, the development of optical sciences continued when the visions from quantum physics were introduced in the 20th century, and studies of light-matter interactions share in understanding of optical processes up to this day.

The advances in nanoscience and technology are in large part due to our newly acquired ability to measure, fabricate and manipulate individual structures on the nanometer scale using scanning probe techniques, optical tweezers, high-resolution electron microscopes and lithography tools, focused ion beam milling systems and others. One of the domains

of nanoscience is the nano-optics, which attracts more and more interest nowadays. The nano-optics focuses on understanding light-matter interactions on a length scale either comparable to, or smaller than, the classical diffraction limit of light [10]. The nano optics is applied in a lot of fields. For example in metamaterials science, plasmonic, communication, astronomy, medicine, photography and different engineering fields. It is also applied in photonic optics, which is in the heart of innovation, combined with other disciplines such as mechanical, electronic and digital techniques. The nano optics has opened up the possibility to create different devices such as: Electro-optical sensors, switches, modulators, nano optical tweezers, waveguides.

Our thesis works are theoretical and based on development the numerical tools for the modeling of experiments that are carried out within our team. We have already large variety of codes based on Finite Difference Time Domain (FDTD) algorithm. However, these codes allow computation of electromagnetic field inside a calculation window including the structure under study and enable determination of eigenmodes of any shape waveguide structure (periodic or not). In addition, and at the beginning of my thesis, our team has experimental project which is supported by the Agence Nationale de la Recherche under Contract ANR10-NANO-002, we proposed to do that work theoretically to provide more interpretation of the results obtained through this project. So, the FDTD code will be modified to calculate the optical force through Maxwell stress tensor (MST) and to study the optical manipulation and trapping of a nanoparticle by using two type of nanoantenna as optical tweezers. In parallel and to address some drawbacks of the FDTD algorithm, 2D FDFD (Finite Difference Frequency Domain) algorithm was developed to solve Maxwells equations as eigenproblem to determine guided mode properties of exotic waveguide designs.

In chapter 2, we will introduce the finite-difference frequency-domain (FDFD) method.

This chapter starts with a presentation of basic Maxwell equations and their derivation in frequency domain. Only eigenproblem, that corresponds to the determination of eigenmodes of a 2D structure, is addressed. Validation of the code is then done through some tests based on comparison with already published results or with results obtained through other methods that are available in our team. Finally, some applications, dealing with the determination of guiding properties for several original geometries of waveguides (ridge and slot waveguides), are performed [11].

In chapter 3, we will introduce the origin of the electromagnetic forces and the principle of optical trapping. Some algebra is then done to derive the analytical expression of the Maxwell Stress Tensor (MST) that allows determination of optical forces. Indeed, this tensor must be calculated over an enclosed surface that contains the particle on which the electromagnetic (EM) force is exerted. The elements of MST are deduced from the known of the electromagnetic field (both electric and magnetic fields) on the considered surface. These values of field can be easily determined by a FDTD simulation. Principle of this powerful method is then presented together with its adjustment to integrate the calculation of the needed MST. The chapter ends with the validation of the developed code and a discussion of its convergence.

In chapter 4, we will present a direct application of our code by studying the 3D optical trapping of small dielectric nanoparticles (NPs) with a fibered nano-antenna. Experimental proof of this trapping was done by our team. The comparison between theoretical and experimental results shows a very good agreement. We theoretically extend the study demonstrating the ability of such nano-tweezers (Fibered Bowtie nano-antenna aperture) to trap smaller NPs.

The last chapter 5 is devoted to a pure theoretical study of optical forces induced by the light-nanoantenna interaction. A Diabolo nano-antenna, that was designed to exhibit

both electric and magnetic field enhancement, is considered. Enhancement of the radiation pressure at its resonance is demonstrated. Different mechanical regimes: trapping at contact, trapping at distance and non trapping of NPs, are pointed out depending on both the NPs radii and the operation wavelength.

Chapter 2

Finite Difference Frequency Domain

2.1 Introduction

The finite-difference frequency-domain (FDFD) method is a numerical method which is commonly used to solve electromagnetic problems, based on finite-difference approximations of the derivative operators in the differential equation to be solved. Whereas "FDFD" is a general term describing all frequency-domain finite-difference methods, the title seems to mostly explain the method as applied to scattering problems [12, 13, 14]. The method exhibits many similarities with the finite-difference time-domain (FDTD) method so that the literature on FDTD can be directly of interest to understand the basic principle. In general, the method works by transforming Maxwell's equations (or other partial differential equation) for sources and fields at a constant frequency into a linear matrix equation $Dx = b$. D is then a matrix that is derived from the wave equation operator, the column vector x contains the field components to be calculated, and the column vector b describes the source. The method can be applied for anisotropic materials, but in this case the off-diagonal components of the tensor appear and they require

special mathematical treatment.

There are at least two kinds of "frequency-domain" problems in electromagnetism [15, 16, 17]. One is dedicated to the steady-state response of a structure in the presence of a time-harmonic source such as a current density J vector in the form $\mathbf{J}(\mathbf{x}) e^{-i\omega t}$, or a similar time-harmonic source. In this case, the frequency-domain problem leads to a $Dx = b$ system of linear equations as described above. The description of a 3D frequency-domain FDTD method to solve scattering problems in the microwave range was published [18] since 1987. The other version of FDFD is devoted to find the eigenmodes of a structure (e.g. a waveguide for instance) in the absence of sources: in this case the frequency ω becomes itself a variable, and one obtains an eigenproblem equation $\Gamma \times x = \Lambda \times x$ (where Γ is the eigenvector, x electromagnetic field components and usually, the eigenvalue Λ is proportional to ω^2). In its original form, the method was used to solve the Helmholtz wave equation [19, 20]. Recently, a full-wave, 2D finite difference frequency domain 2D FDFD algorithm was proposed that solved Maxwells equations directly [21, 22, 23, 24, 25]. A lot of researches used FDFD method to guiding the light due it has more advantage [26, 27, 28, 29, 30, 31, 32], where it has been useful.

2.2 Motivations for using FDFD method

The numerical methods that are generally applied to the resolution of the electromagnetic wave problems can be classified into two general categories: time domain methods and frequency domain methods. In the frequency-domain formulation, the solution is described as a set of time-harmonic modes. The advantages of solving the electromagnetic wave problems in frequency domain can be attributed to two properties: first, it can handle any frequency dependent properties of materials such as dispersion. Second, simulations

in frequency domain are faster when only responses for a few frequencies are required.

The main motivation of using FDFD method in our case lies many reasons. In fact, our team had developed many FDTD code that can simulate both infinite or finite structures in 2D and in 3D. Especially, we have implemented the N-order FDTD algorithm allowing determining of the eigenmodes. But this code has some drawbacks as it cannot allow fixing the mode frequency. In this case, the propagation constant \vec{k} is set and the algorithm allows the calculation of the eigenmode frequencies in a given frequency range. For example, if we want to calculate the eigenmodes of a step-index dielectric cylindrical optical fiber (see figure 2.1 a) we can use both the N-order FDTD-code or the FDFD-code. Nevertheless, the first one gives a map of the EM spectral density (SD) over some range of wavelengths where maxima of this SD correspond to the excitation of an eigenmode (see figure 2.1 b). Now, if we want to determine the eigenmode properties at a desired value of $\lambda = 1.5\mu m$, we have to make N-Order FDTD calculations over a wide range of k and make a cross-section (the white dashed line) to determine the excited eigenmodes at this value of λ . In fact, we don't know in advance which k will give us the good eigenmode. Consequently, this is obtained at the coast of many FDTD calculations by changing the value of k and, simultaneously checking if the results correspond to the fixed operation wavelength. This can be very time-consuming (16 hours in the case of figure 2.1 b for instance). On the contrary, in FDFD code, we can directly fix the frequency (wavelength) and make one simulation that gives us the propagation constants (i.e. the effective index of the modes) corresponding to the excitation of the first N guided modes ($N = 4$ in 2.2) at this wavelength. So, we chose FDFD method in our study because it is more suitable and simple for our simulation .

Another drawback of the FDTD is related to the modeling of a nonlinear material due to the apparition of a time convolution integral that needs to be calculated by storing

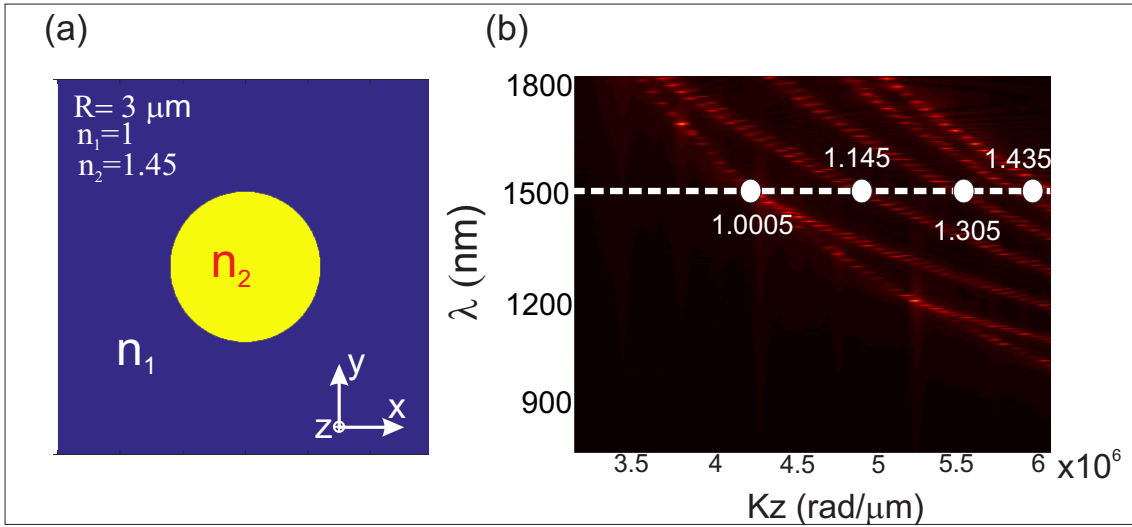


Figure 2.1: (a): schema of the step-index dielectric cylindrical optical fiber. The radius is set to $R = 3\mu m$, the cladding index is $n_1 = 1$ and the core index is $n_2 = 1.45$. (b) N-order FDTD results showing a map of the spectral density as a function of the propagation constant. The white dashed horizontal line correspond to the operation wavelength ($\lambda = 1.5\mu m$). Intersections with high spectral density give the excited mode propagation constants.

the values of the electric field components at all the grid nodes and for all the time steps [33]. In the frequency-domain equation, this convolution turns into a simple product. Consequently, FDFD seems to be more appropriate in this case.

According to the discrepancies between FDTD and FDFD, these two methods appear to be complementary: FDTD being suitable for the determination of dispersion diagram while FDFD can be faster in the case of monochromatic calculations.

In this chapter, we will introduce the finite-difference frequency domain method in the context of the electromagnetic eigenproblem. We used the formulation of the FDFD method in the framework of matrix operators over a Yee grid [34]. We will focus on the Maxwell's equations formulation and give overview as shown in the section (2.3). Because the method uses frequency domain equations, the results yield only single frequency $\omega(\lambda)$, a steady-state solution. Responses over large spectral domain are then determined by

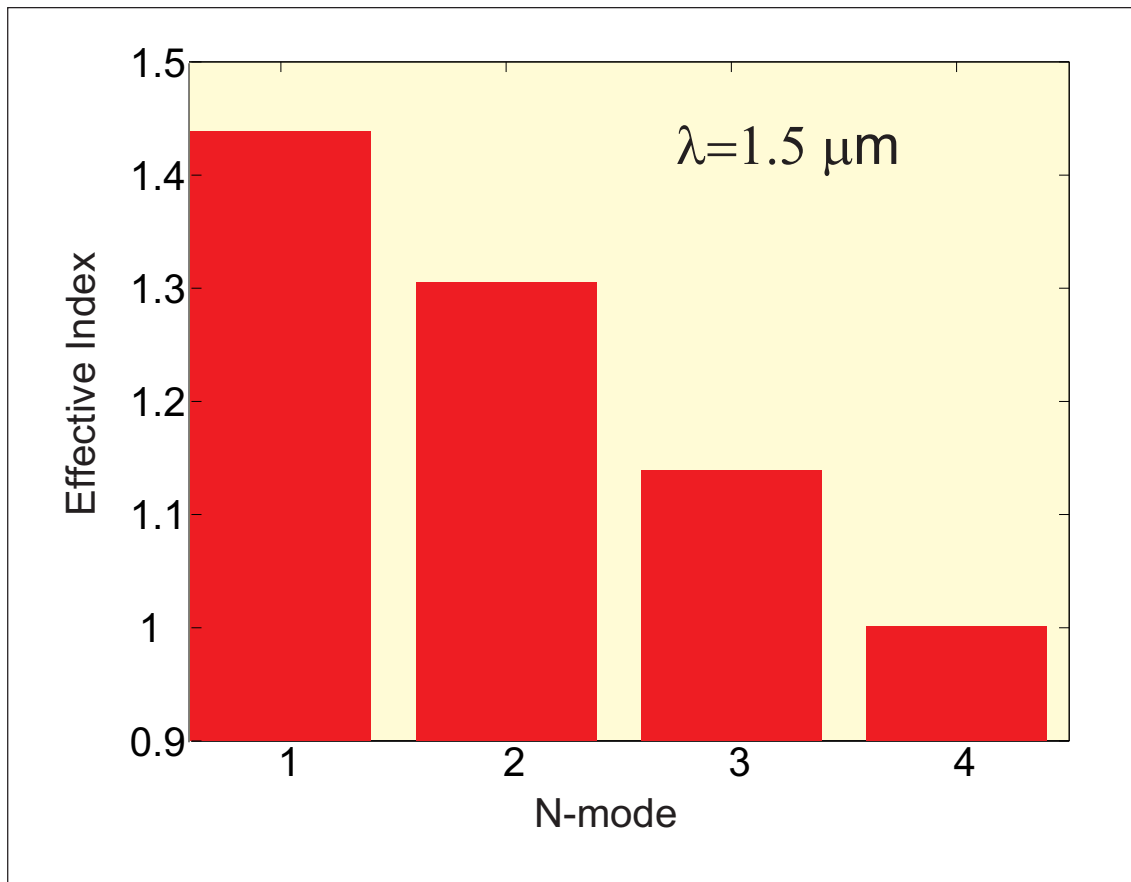


Figure 2.2: FDFD results giving the effective index of the first $N = 4$ guided modes inside the fiber at $\lambda = 1.5 \mu\text{m}$.

repeating the simulation for all desired values of the frequency. This is often the most desirable solution to many problems, as many engineering problems involve quasi-steady state field; this is much faster than transient broadband analysis as by FDTD [35]. For all of these reasons, we developed the FDFD method and implemented a Matlab code.

2.3 Maxwell Equations

Around 1865, Maxwell has achieved a harmonious synthesis of various experimental laws discovered by his predecessors (the laws of electrostatic, magnetostatic, Faraday's law of

induction ...), by expressing them in the form of a system of four equations coupled with spatio-temporal partial derivatives. They were published in final form in 1873 in the book "Electricity and magnetism". Maxwell's equations, known as Maxwell-Lorentz equations are fundamental laws of physics. They are the basic postulates of electromagnetism with the expression of the electromagnetic Lorentz force. These equations translate, in local form, different relationships (between the electric field \vec{E} , the magnetic field \vec{H} and the electric and magnetic excitations \vec{D} and \vec{B} respectively) that govern electromagnetism and can be divided into two sets.

2.3.1 Topological equations (without source)

- Faraday Equation

$$\vec{\nabla} \times \vec{E} = -\frac{\partial \vec{B}}{\partial t} \quad (2.1)$$

This gives the spatial variation of the electric field as a function of the temporal variation of the magnetic field. This equation describes all induction phenomena and shows that a time varying of the magnetic field can create a non-zero electric field circulation i.e. an electromotive force.

- Conservation of the magnetic field

$$\vec{\nabla} \cdot \vec{B} = 0 \quad (2.2)$$

This reflects the fact that the flux of the magnetic field through any closed surface is zero. This is an intrinsic property of \vec{B} which shows that the magnetic field may differ from points in space, or that there are no magnetic charges (no magnetic monopole).

2.3.2 Metric equations (equations with source):

- Maxwell-Gauss equation

$$\vec{\nabla} \cdot \vec{E} = \frac{\rho}{\varepsilon_0} \quad (2.3)$$

Where ρ is the volume charge density (source of the electric field). This equation expresses the fact that the electric flux through any closed surface is equal to the sum of interior charges; the Gauss theorem that is well-known in electrostatic.

- Maxwell-Ampere equation

$$\vec{\nabla} \times \vec{H} = \vec{j} + \frac{\partial \vec{D}}{\partial t} \quad (2.4)$$

Where \vec{j} and \vec{H} represent respectively, the vector of surface current density and the magnetic field. This equation relates the magnetic field sources and the electric field. In steady system, we find Ampere's theorem showing that the magnetic field rotates around the currents. The additional term $\varepsilon_0 \frac{\partial \vec{E}}{\partial t}$ called displacement current indicates that a variable electric field behaves as a magnetic field source.

These four equations are governing the static and dynamic electromagnetic phenomena. They couple the electric and magnetic fields through spatial and temporal local differential equations. To these four Maxwell equations, two essential additional constitutive equations which describe the response of the medium. In the case of LHI (linear, homogeneous, isotropic) media they can be given by:

$$\vec{D} = \varepsilon \vec{E} \quad (2.5)$$

$$\vec{B} = \mu \vec{H} \quad (2.6)$$

Where $\varepsilon = \varepsilon_0 \varepsilon_r$ is absolute permittivity. ε_0 , ε_r are vacuum permittivity and the relative permittivity of the medium respectively. $\mu = \mu_0 \mu_r$ is the magnetic permeability of a specific medium. μ_0 , μ_r are vacuum permeability and relative permeability respectively. In the visible range, all the homogeneous materials are non-magnetic which leads to $\mu_r = 1$.

2.4 Matrix Form of Maxwell Curl Equations :case of eigenmode calculations

As we work in harmonic regime let us call $\vec{\Psi}$ any electromagnetic field components \vec{E} , \vec{H} , \vec{B} or \vec{D} . It can be expressed as:

$$\vec{\Psi}(\vec{r}, t) = \vec{\Psi}_0(\vec{r})e^{-i\omega t} \quad (2.7)$$

From Eq.2.7 we can get Maxwell curl equations for source-free media in the frequency-domain:

$$\nabla \times \vec{E} = -i\omega\mu_0\vec{H} \quad (2.8)$$

$$\nabla \times \vec{H} = i\omega\varepsilon_0\varepsilon_r\vec{E} \quad (2.9)$$

More explicitly, in x,y,z Cartesian coordinate we rewrite these equations as shown:

$$\begin{vmatrix} \frac{\partial}{\partial x} \\ \frac{\partial}{\partial y} \\ \frac{\partial}{\partial z} \end{vmatrix} \times \begin{vmatrix} E_x \\ E_y \\ E_z \end{vmatrix} = i \omega \mu_0 \cdot \begin{vmatrix} H_x \\ H_y \\ H_z \end{vmatrix} \quad (2.10)$$

$$\begin{vmatrix} \frac{\partial}{\partial x} \\ \frac{\partial}{\partial y} \\ \frac{\partial}{\partial z} \end{vmatrix} \times \begin{vmatrix} H_x \\ H_y \\ H_z \end{vmatrix} = -i \omega \varepsilon_0 \varepsilon_r \cdot \begin{vmatrix} E_x \\ E_y \\ E_z \end{vmatrix} \quad (2.11)$$

Where H_x, H_y, H_z , are three components of magnetic field. Likewise, E_x, E_y, E_z are three components of electric field. Let us develop the cross products:

$$\frac{\partial E_z}{\partial y} - \frac{\partial E_y}{\partial z} = i \omega \mu_0 H_x \quad (2.12)$$

$$\frac{\partial E_x}{\partial z} - \frac{\partial E_z}{\partial x} = i \omega \mu_0 H_y \quad (2.13)$$

$$\frac{\partial E_y}{\partial x} - \frac{\partial E_x}{\partial y} = i \omega \mu_0 H_z \quad (2.14)$$

$$\frac{\partial H_z}{\partial y} - \frac{\partial H_y}{\partial z} = -i \omega \varepsilon_0 \varepsilon_x E_x \quad (2.15)$$

$$\frac{\partial H_x}{\partial z} - \frac{\partial H_z}{\partial x} = -i \omega \varepsilon_0 \varepsilon_y E_y \quad (2.16)$$

$$\frac{\partial H_y}{\partial x} - \frac{\partial H_x}{\partial y} = -i \omega \varepsilon_0 \varepsilon_z E_z \quad (2.17)$$

Let us consider a 2D eigenproblem of an invariant structure along the z-direction. Our problem is then to determine the structure modes that propagate along the z-direction with a propagation constant β . Each component of the electromagnetic field can then be expressed as:

$$\Psi_m(\vec{r}, t) = \Psi_{0m}(\vec{r})e^{i(\beta z - \omega t)} \quad m \in [x, y, z] \quad (2.18)$$

Thus, the equations (2.12) to (2.17) become as:

$$\frac{\partial E_z}{\partial y} - i\beta E_y = i \omega \mu_0 H_x \quad (2.19)$$

$$i\beta E_x - \frac{\partial E_x}{\partial z} = i \omega \mu_0 H_y \quad (2.20)$$

$$\frac{\partial E_y}{\partial x} - \frac{\partial E_x}{\partial y} = i \omega \mu_0 H_z \quad (2.21)$$

$$\frac{\partial H_z}{\partial y} - i\beta H_y = -i \omega \varepsilon_0 \varepsilon_r E_x \quad (2.22)$$

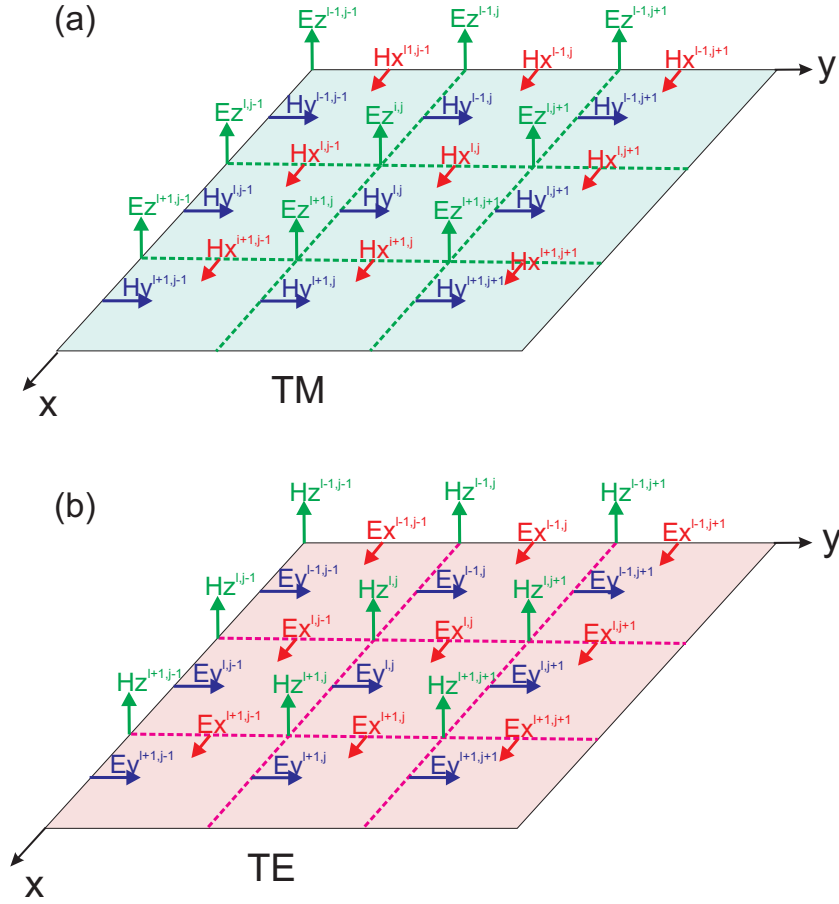
$$i\beta H_x - \frac{\partial H_z}{\partial x} = -i \omega \varepsilon_0 \varepsilon_r E_y \quad (2.23)$$

$$\frac{\partial H_y}{\partial x} - \frac{\partial H_x}{\partial y} = -i \omega \varepsilon_0 \varepsilon_r E_z \quad (2.24)$$

In order to solve this system of equations through finite-difference approximation, we need to discretize the space with small cells (cubes in 3D or squares in 2D). After this step, we approximate the partial derivatives (in time and in space) by their central finite-difference expressions for each cell of the Yee's mesh. For example, for 2D problem as in figure 2.3, Eq 2.19 becomes:

$$\frac{E_z^{(l,j+1)} - E_z^{(l,j)}}{\Delta y} - i \beta E_y^{(l,j)} = i \omega \mu_0 H_x^{(l,j)} \quad (2.25)$$

After discretizing all the six equations above, one obtains the two matrix-form equations:


 Figure 2.3: Yee - mesh 3×3 in two dimensions. a)TE mode. b)TM mode

$$i \omega \mu_0 \cdot \begin{bmatrix} H_x \\ H_y \\ H_z \end{bmatrix} = \begin{bmatrix} 0 & -i \beta I & D_y^E \\ i \beta I & 0 & -D_x^E \\ -D_y^E & D_x^E & 0 \end{bmatrix} \begin{bmatrix} E_x \\ E_y \\ E_z \end{bmatrix} \quad (2.26)$$

$$-i \omega \varepsilon_0 \cdot \begin{bmatrix} \varepsilon_x & 0 & 0 \\ 0 & \varepsilon_y & 0 \\ 0 & 0 & \varepsilon_z \end{bmatrix} \cdot \begin{bmatrix} E_x \\ E_y \\ E_z \end{bmatrix} = \begin{bmatrix} 0 & -i \beta I & D_y^H \\ i \beta I & 0 & -D_x^H \\ -D_y^H & D_x^H & 0 \end{bmatrix} \begin{bmatrix} H_x \\ H_y \\ H_z \end{bmatrix} \quad (2.27)$$

I is identity matrix and β is the propagation constant. D_x^E, D_y^E are matrices that perform spatial derivative operations on electric fields. Likewise, D_x^H, D_y^H are matrices

that perform spatial derivative operations on magnetic fields. They are given by:

$$(D_x^E E)_{l,j} = \frac{E^{l+1,j} - E^{l,j}}{\Delta x} \quad (2.28)$$

$$(D_y^E E)_{l,j} = \frac{E^{l,j+1} - E^{l,j}}{\Delta y} \quad (2.29)$$

$$(D_x^H H)_{l,j} = \frac{H^{l-1,j} - H^{l,j}}{\Delta x} \quad (2.30)$$

$$(D_y^H H)_{l,j} = \frac{H^{l,j-1} - H^{l,j}}{\Delta y} \quad (2.31)$$

For a pure propagation along the z -direction, two polarization states can be studied independently. Namely, the TM state that corresponds to a magnetic field that is perpendicular to the propagation direction (\vec{H} is then in the xOy plane) and the TE state for which the electric field is perpendicular to Oz axis. Figure 2.3 shows a small (3×3) $2D$ Yee mesh in these two cases of polarization (TM in figure 2.3 a) and (TE in figure 2.3 b).

Equations 2.26 and 2.27 become:

$$i \omega \mu_0 H_z = -D_y^E E_x + D_x^E E_y \quad (2.32)$$

$$-i \omega \varepsilon_0 E_z = -D_y^H H_x + D_x^H H_y \quad (2.33)$$

$$D_x^H = \frac{1}{\Delta x} \cdot \begin{bmatrix} 1 & 0 & 0 & 0 & 0 & 0 & 0 & 0 & 0 \\ -1 & 1 & 0 & 0 & 0 & 0 & 0 & 0 & 0 \\ 0 & -1 & 1 & 0 & 0 & 0 & 0 & 0 & 0 \\ 0 & 0 & 0 & 1 & 0 & 0 & 0 & 0 & 0 \\ 0 & 0 & 0 & -1 & 1 & 0 & 0 & 0 & 0 \\ 0 & 0 & 0 & 0 & -1 & 1 & 0 & 0 & 0 \\ 0 & 0 & 0 & 0 & 0 & 0 & 1 & 0 & 0 \\ 0 & 0 & 0 & 0 & 0 & 0 & -1 & 1 & 0 \\ 0 & 0 & 0 & 0 & 0 & 0 & 0 & -1 & 1 \end{bmatrix} \quad (2.36)$$

$$D_y^H = \frac{1}{\Delta y} \cdot \begin{bmatrix} 1 & 0 & 0 & 0 & 0 & 0 & 0 & 0 & 0 \\ 0 & 1 & 0 & 0 & 0 & 0 & 0 & 0 & 0 \\ 0 & 0 & 1 & 0 & 0 & 0 & 0 & 0 & 0 \\ -1 & 0 & 0 & 1 & 0 & 0 & 0 & 0 & 0 \\ 0 & -1 & 0 & 0 & 1 & 0 & 0 & 0 & 0 \\ 0 & 0 & -1 & 0 & 0 & 1 & 0 & 0 & 0 \\ 0 & 0 & 0 & -1 & 0 & 0 & 1 & 0 & 0 \\ 0 & 0 & 0 & 0 & -1 & 0 & 0 & 1 & 0 \\ 0 & 0 & 0 & 0 & 0 & -1 & 0 & 0 & 1 \end{bmatrix} \quad (2.37)$$

Each of these matrices contains nonzero elements only along two diagonals leading to very sparse matrices that can be constructed very quickly. The sparse matrices can be stored efficiently in computers to reduce the amount of memory required for data storage. In the case of a uniform meshing all diagonals are uniform except where quantities are

written in red. These exceptions arise from the Dirichlet boundary conditions.

After developing eqs. 2.26,2.27 and after some algebra we arrived to a same formula as for eigenproblem equation which is defined in general case by:

$$\Gamma \times x = \Lambda \times x \quad (2.38)$$

Where x is the eigenvector, Λ is the eigenvalue equal to β^2 in our case. So, for the transverse electric case, the eq.2.38 becomes:

$$\begin{bmatrix} P_{xx} & P_{xy} \\ P_{yx} & P_{yy} \end{bmatrix} \begin{bmatrix} E_x \\ E_y \end{bmatrix} = \beta^2 \begin{bmatrix} E_x \\ E_y \end{bmatrix} \quad (2.39)$$

Where

$$\begin{aligned} P_{xx} &= -\omega^{-2} D_x^E \varepsilon_r^{-1} D_y^H D_x^H D_y^E + (\omega^2 I + D_x^E \varepsilon_r^{-1} D_x^H)(\varepsilon_r + \omega^{-2} D_y^H D_y^E) \\ P_{yy} &= -\omega^{-2} D_y^E \varepsilon_r^{-1} D_x^H D_y^H D_x^E + (\omega^2 I + D_y^E \varepsilon_r^{-1} D_y^H)(\varepsilon_r + \omega^{-2} D_x^H D_x^E) \\ P_{xy} &= D_x^E \varepsilon_r^{-1} D_y^H (\varepsilon_r + \omega^{-2} D_x^H D_x^E) - \omega^{-2}(\omega^2 I + D_x^E \varepsilon_r^{-1} D_x^H) D_y^H D_x^E \\ P_{yx} &= D_y^E \varepsilon_r^{-1} D_x^H (\varepsilon_r + \omega^{-2} D_y^H D_y^E) - \omega^{-2}(\omega^2 I + D_y^E \varepsilon_r^{-1} D_y^H) D_x^H D_y^E \end{aligned} \quad (2.40)$$

Similarly, we can get an eigenvalue equation in terms of transverse magnetic fields:

$$\begin{bmatrix} Q_{xx} & Q_{xy} \\ Q_{yx} & Q_{yy} \end{bmatrix} \begin{bmatrix} H_x \\ H_y \end{bmatrix} = \beta^2 \begin{bmatrix} H_x \\ H_y \end{bmatrix} \quad (2.41)$$

$$\begin{aligned} Q_{xx} &= -\omega^{-2} D_x^H D_y^E D_x^E \varepsilon_r^{-1} D_y^H + (\varepsilon_r + \omega^{-2} D_x^H D_x^E)(\omega^2 I + D_y^E \varepsilon_r^{-1} D_y^H) \\ Q_{yy} &= -\omega^{-2} D_y^H D_x^E D_y^E \varepsilon_r^{-1} D_x^H + (\varepsilon_r + \omega^{-2} D_x^H D_y^E)(\omega^2 I + D_x^E \varepsilon_r^{-1} D_x^H) \\ Q_{xy} &= -(\varepsilon_r + \omega^{-2} D_x^H D_x^E) D_y^E \varepsilon_r^{-1} D_x^H + \omega^{-2} D_x^H D_y^E (\omega^2 I + D_x^E \varepsilon_r^{-1} D_x^H) \\ Q_{yx} &= -(\varepsilon_r + \omega^{-2} D_y^H D_y^E) D_x^E \varepsilon_r^{-1} D_y^H + \omega^{-2} D_y^H D_x^E (\omega^2 I + D_y^E \varepsilon_r^{-1} D_y^H) \end{aligned} \quad (2.42)$$

Under Dirichlet boundary conditions, we can verify that $D_x^H = -D_x^{ET}$ and $D_y^H = -D_y^{ET}$ where the symbol T is indicate to the transpose operation. Then, it is clear from eqs.2.40 and 2.42, that:

$$Q_{xx} = P_{yy}^T, \quad Q_{yy} = P_{xx}^T, \quad Q_{xy} = -P_{xy}^T, \quad Q_{yx} = -P_{yx}^T \quad (2.43)$$

After constructing the matrices P and Q, we solved eqs.2.40 or 2.42 through the function "eigs" of matlab. It provides us the effective mode index $n_{eff} = \frac{\beta}{k_0}$ (where $k_0 = \frac{2\pi}{\lambda}$ is the wave number in vacuum) and fields of the each guided mode. Through :

$$[\Gamma, v] = \text{eigs}(P \text{ or } Q, nm, LR)$$

Γ contains all the eigenvectors of the (nm) modes that we are considering and sorting

as largest real (LR). v is a vector that contains all the eigenvalue(β^2). The effective index can then be written as:

$$n_{eff} = \frac{\sqrt{v}}{k_0}$$

Figure 2.4 shows the diagram of FDFD implementation used in our matlab code. Also, we programmed our code by using Fortran language with *LAPACK* function which

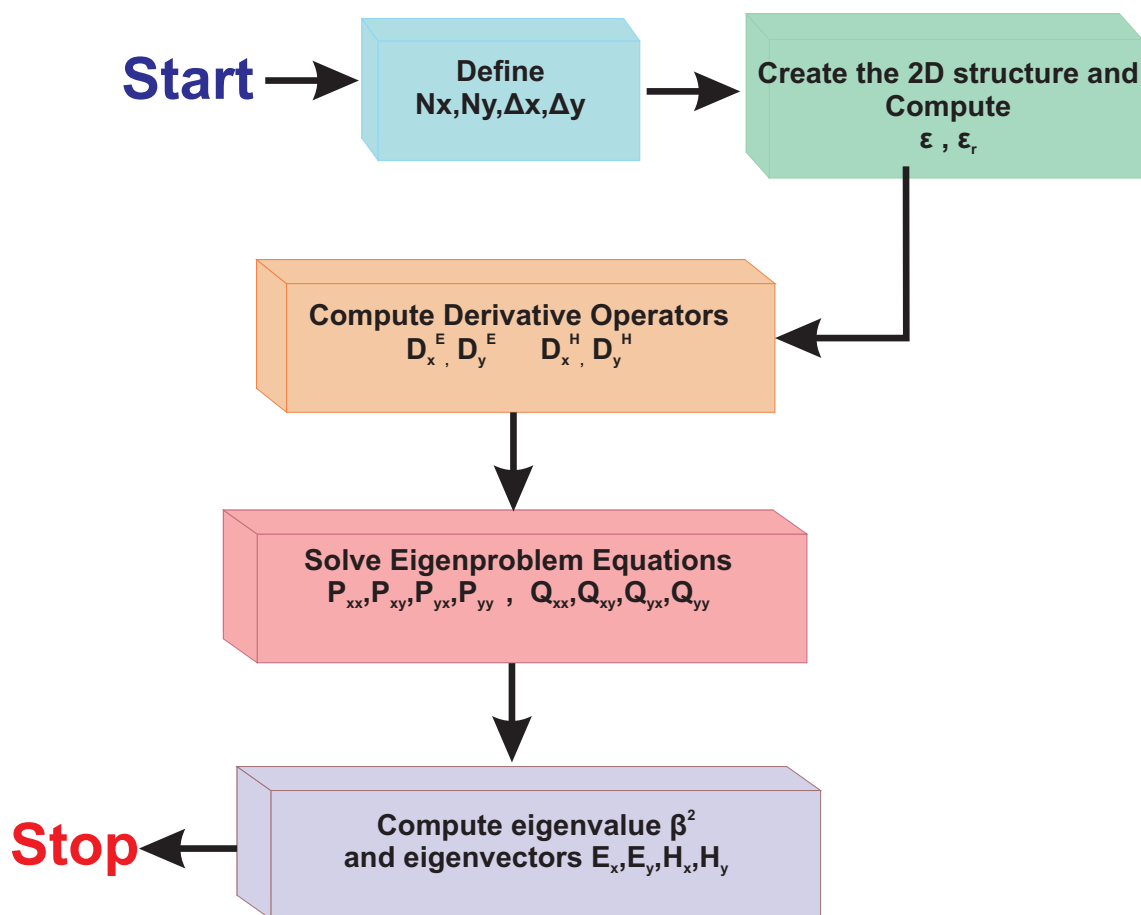


Figure 2.4: Block diagram of FDFD implementation

provides routines for solving eigenvalue problems. But we found that it takes more long time and large memory in comparison to matlab code. So, matlab-code was used in our simulations.

2.5 Validation of FDFD matlab code

As mentioned before, we built FDFD matlab code by using formulations of Maxwell equations in frequency domain and from the eigenvalue equation eqs.2.39,2.41 that allows determination of the propagation constant, and then the effective index. To validate this code, we did some tests and compared our results with already published ones made, for the same method and second by other theories. Let us show here only 2 tests of(2D-WG).

2.5.1 Test 1: Step-Index Circular Optical Fiber (SIOF)

The first test was devoted to the determination of the effective index of a step-index circular fiber which was studied in [1]. We used our FDFD matlab-code to calculate the effective index of the first guided modes (5 modes here) of the fiber and compare our results to the ones published in that reference [1]. The fiber core radius is fixed to $R = 3\mu m$ (see figure 2.5) with a refractive index of $n_1 = 1.45$ and it is supposed to be surrounded by air $n_2 = 1$. This structure is discretized a uniform meshing schema. The eigenmodes of the structure are determined at the operation wavelength of $\lambda = 1.5\mu m$. We used different grid dimensions (30×30 to 120×120) to see the convergence of our code. First, we observed that when the grid dimensions are equal to 70×70 the calculation is stopped because of lack of memory. This calculation was done on a personal computer with processor Intel(R) Core(TM) i5-2520M CPU @ 2.59 GHz and 4 Go of memory. We tried to do the calculations with number of grid more than 70×70 by using workstation in our lab where the calculator properties are: 4×12 cores AMD Opteron(tm) Processor 6174, 256 Go of memory, Linux CentOS release 5.6 (Final) operating system. We got results for large grid dimensions, (up to 120×120) with good accuracy but taking very long time(15 hours).

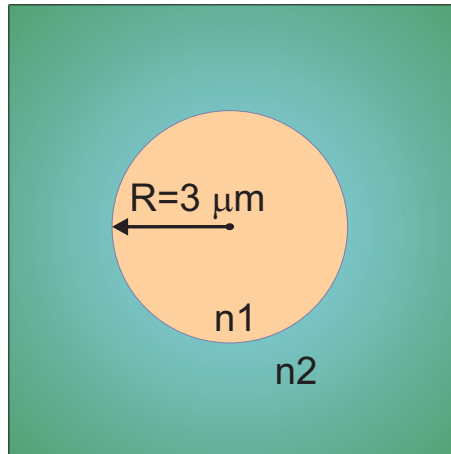


Figure 2.5: Scheme of Step-Index Circular Optical Fiber

In order to faithfully describe the structure under study, a subgridding technique was also employed as shown in figure 2.6. Comparison of the convergence for non subgridding and subgridding technique was performed in the case of SIOF. Figure 2.7 a, shows the obtained results n_{eff} in comparison with analytical value. We can observe very clearly a more quick converge when we apply subgridding technique in our code. This is confirmed through the calculations of the relative errors in both cases figure 2.7 b.

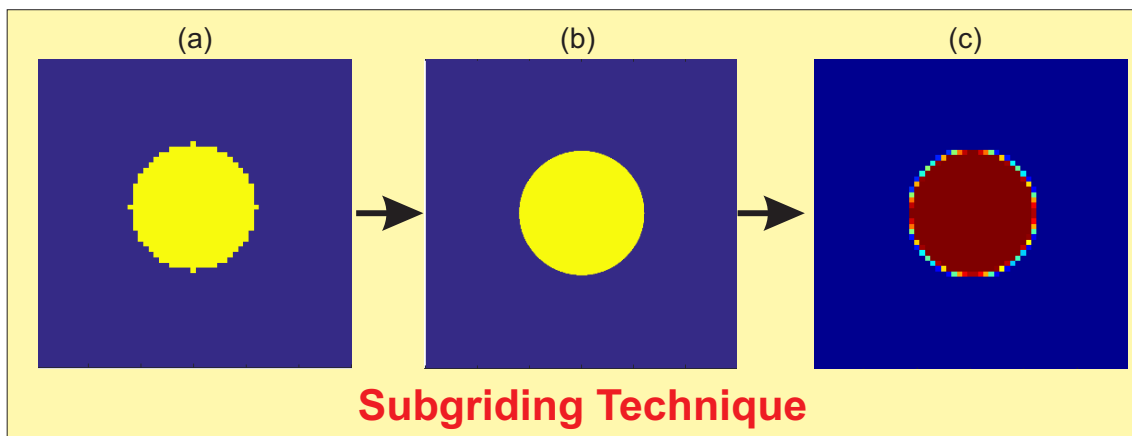


Figure 2.6: Subgridding Technique.

Then we compared our result with Zhu et al [1] and with other methods such as differential method developed by our team (Philippe Boyer). A good agreement between

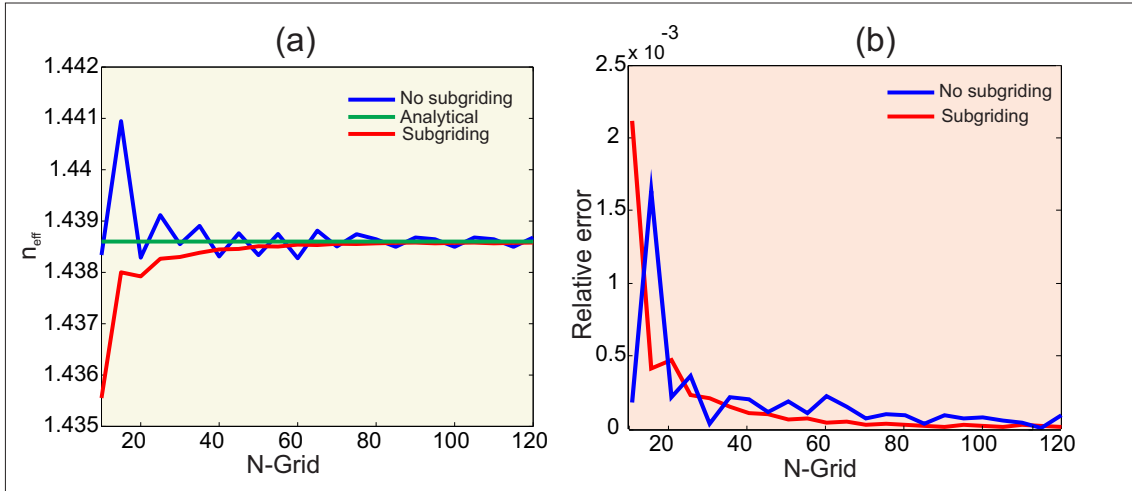


Figure 2.7: (a) Convergence studies. (b) Relative errors ratio

all results is found as shown in table 2.1. But, we can observe little difference in the value of the fundamental mode between our results and the one obtained by the differential method. This difference is caused by the staircase mesh, that appears on the edges of the (circular optical fiber). In table 2.1, we list calculated fundamental mode index for two different meshing parameters. The electric field distribution of different modes are also given in figure 2.8.

Table 2.1: Fundamental mode index for step-index circular optical fiber

N_x, N_y	Our work	Differential method	Zhu et al [1]	Lusse et al [36]
60	1.43861	1.43860	1.43861	1.43854
120	1.43861		1.43861	1.43859

To decrease the simulations time without decreasing its accuracy calculation, we developed a FDFD-code with nonuniform mesh. We calculate the effective index of the same step-index circular fiber with nonuniform mesh. The spatial step varies from 300 nm outside the fibers to 150 nm in the region of the fiber as shown in figure 2.9 a. To keep the same area as in the uniform mesh, we obtain $Lx = Ly = 1.5 \mu m$. Thus the relative error smaller than the results obtained with uniform mesh as shown in figure 2.9 b. Nevertheless, the time memory was divided by 2.

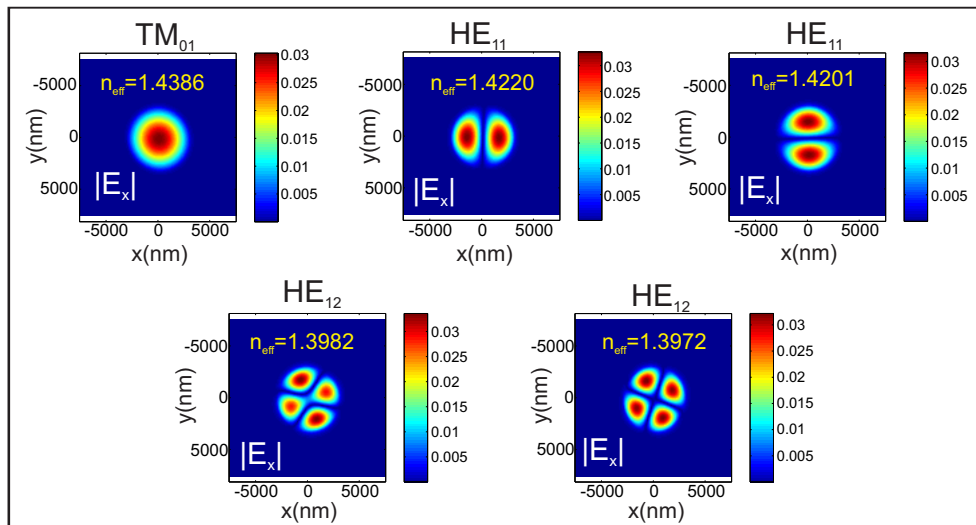


Figure 2.8: Electric field distribution for different modes index of step-index circular optical fiber

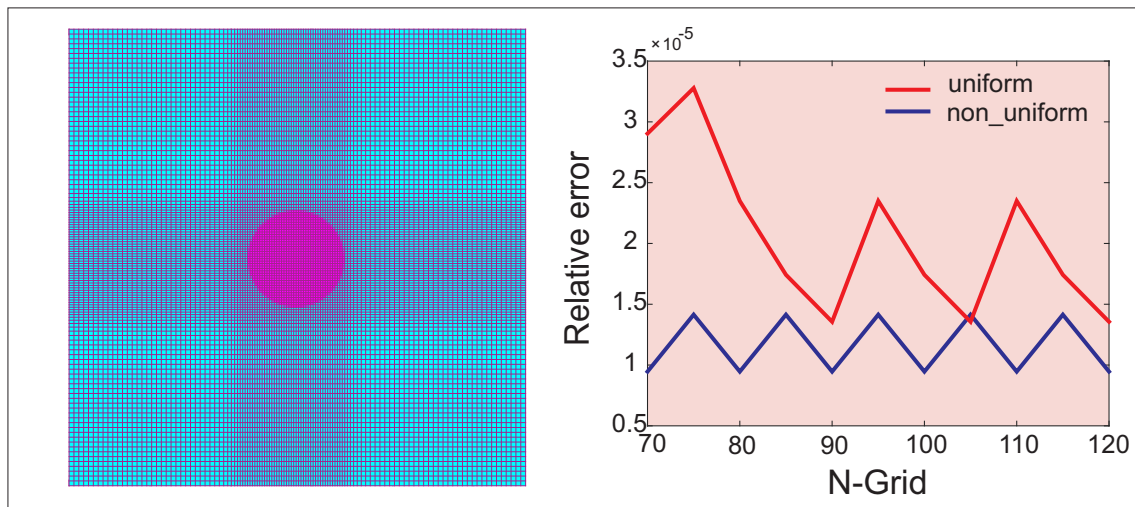


Figure 2.9: Relative error of uniform and nonuniform mesh.

Thus with $N_x = N_y = 120$, the relative error can be considered negligible. So, that all following calculations of mode with these parameters.

2.5.2 Test 2: Air-Hole-Assisted Optical Fiber (AHAOF)

In the second test, we calculate the fundamental effective index of air-hole-assisted optical fiber (AHAOF) [1]. It consists on a high-index guiding core with cylindrical shape surrounded by six air holes placed at the corners of a regular hexagon as shown in figure 2.10. One interesting characteristic of the AHAOF is their polarization and dispersion properties exhibiting a transmission loss lower than conventional optical fiber.

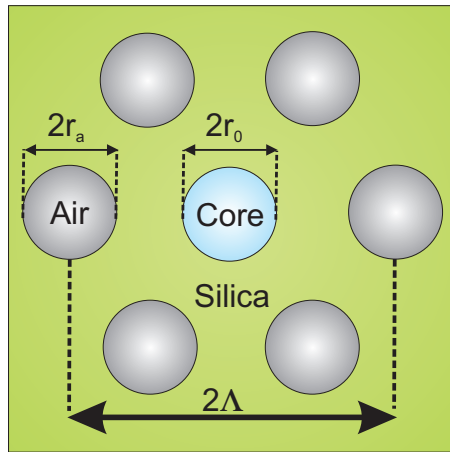


Figure 2.10: Scheme of Air-Hole-Assisted Optical Fiber

The geometrical and optical parameters of the structure are (see figure 2.10): core index $n = 1.45$, silica cladding index $n_{si} = 1.42$, $r_0 = 2\mu m$, $r_a = 2\mu m$ and $\Lambda = 5\mu m$ with uniform mesh. As in the first test, we have fixed the operation wavelength value to $\lambda = 1.5\mu m$ and calculated the eigenmode for different dimensions grid. Figure 2.11 shows the comparison of AHAOF fundamental mode between our matlab-code result and the result obtained in [1]. A qualitatively good agreement is obtained. In table 2.2, we list calculated fundamental mode indices and figure 2.12 shows magnetic field distribution for different guided modes of AHAOF. Our results are in a good agreement with the results obtained by [1, 36].

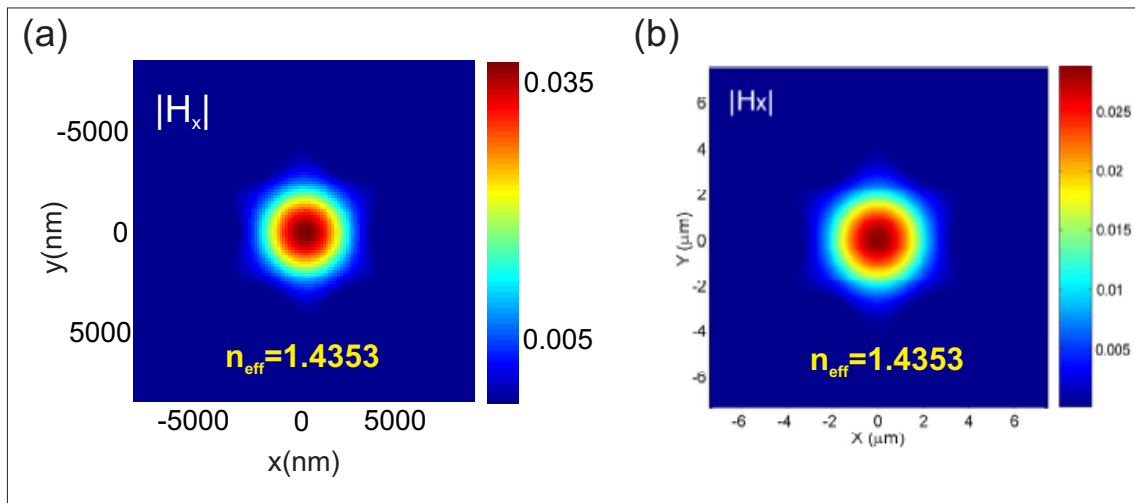


Figure 2.11: Magnetic field distribution of fundamental mode index of Air-Hole-Assisted Optical Fiber. a) Our calculations results. b) Zhu et al [1] results.

Table 2.2: Fundamental mode index for air-hole-assisted optical fiber

Number of grid along X-axis	Our work	Zhu et al [1]	Lusse et al [36]
60	1.43535	1.43535	1.43528
120	1.43525	1.43536	1.43533

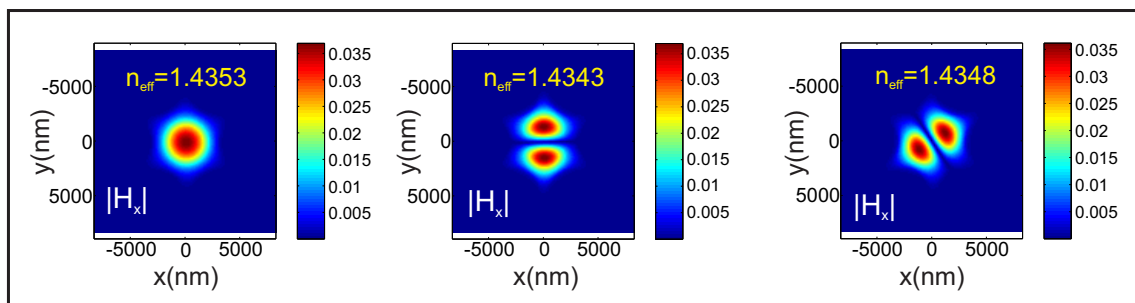


Figure 2.12: Magnetic field distribution for different modes index of Air-Hole-Assisted Optical Fiber

2.6 Application of our FDFD code

We present here a study of two different configurations of waveguide made in lithium niobate ($LiNbO_3$). We named the first "slot waveguide (SW)" while the second is named "ridge waveguide". These two types of waveguide were proposed by our team to support

nanopatterned structure (photonic crystal for instance) in order to build tunable devices such as electrooptical modulators. The first one was proposed in reference [11], "SW" among other configurations of small waveguide. In parallel, the second was proposed in reference [37] to handle an ultra short Bragg grating (only $8\mu m$ length) exhibiting high reflectivity up to 50% for both TE and TM modes. In both cases, the geometries allow light to be strongly confined inside a nanometer scale region of low refractive index (the waveguide core). In addition, they are easy to manufacture enabling miniaturization, integration with electronic, photonics and very convenient with nonlinear optical applications. In the following, we will consider each of them and find the optical properties of its fundamental guided mode.

2.6.1 Study of the "slot waveguide"

In this paragraph, we present a study of the SW with the developed FDFD code to solve the eigen modes of this waveguide. In 2004 the slot optical waveguides was proposed by M. Lipson's team at Cornell Nano photonics Center [23] and then experimentally fabricated and characterized [38]. That group stunned the photonic researchers by discovering this extraordinary structure geometry. In fact, light is confined inside very small (sub- λ) low index slot region as a result of an electric field discontinuity. It was named "slot waveguide" due to its physical shape, a low index slot surrounded by two high index slabs (see figure 2.13). Slot waveguide structure has achieved a lot of interests and big importance due to its ability to be applied in Nano-photonics. The large light confinement can be exploited to exacerbate the optical non-linearity of the used materials (high or low refractive indices). Our team planned to engrave a 2D photonic crystal (PC) on the top interface of the SW. The transmission response of the whole structure (SW+PC) can then be tuned with external signal such as electric or acoustic perturbation.

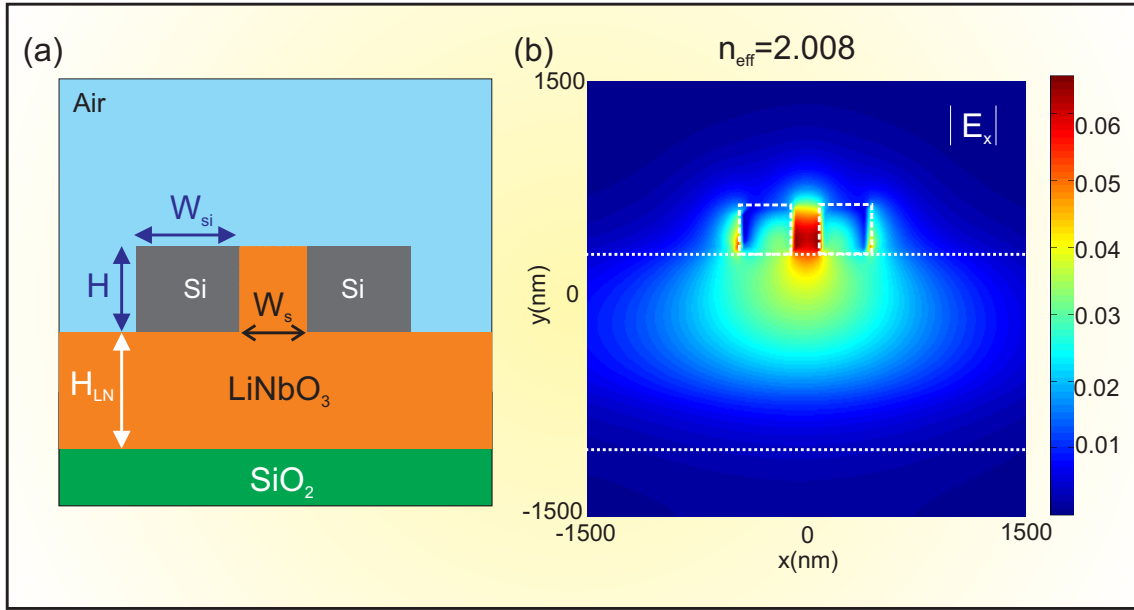


Figure 2.13: a) Scheme of slot waveguide. b) Electric field distribution of fundamental mode index of slot waveguide

Figure 2.13 a shows a view of a slot waveguide structure that comprises three slabs: two *Si* ones with high refractive index $n_{Si} = 3.48$ and a low refractive index slot made of *LiNbO₃* formed in between the slabs. The three slabs are surrounded by air from the top and lateral sides and by *LiNbO₃* from down. This configuration is consistent with technological constraints of a lithium niobate wafer available by NANO-LN company [39]. A parametric study on this kind of SW was performed in the reference [11]. We only show here an example of result obtained in a specific configuration that allows very high light confinement. Consequently, the *LiNbO₃* slot width is fixed to $W_s = 150$ nm, the silicon side walls width is $W_{Si} = 200$ nm and the height of the structure is $H = 150$ nm. Numerical simulations are performed using uniform mesh $\Delta x = \Delta y = 25$ nm over an area of $3 \times 3 \mu m^2$. Only TE polarization (electric field along the propagation direction) leads to a large confined guided mode in the *LiNbO₃* slot. As mentioned before, this is due to the electric field discontinuity on the *LiNbO₃*-*Si* interfaces. Consequently, the electric field of the mode must be oriented perpendicularly to those interfaces. Here \vec{E} is mainly

along the x-direction. In such a case, the normal electric field component E_N suffers a large discontinuity (only D_N is continuous) due to the refractive index contrast between $LiNbO_3$ and Si. FDFD results yield to a fundamental mode with $n_{eff} = 2.008$ with the electric field distribution shown on figure 2.13 b. Reader can refer to reference [11] for more details about the optimization of this configuration. Table 2.3 gives the effective indices of the first 5 guided modes in the structure.

Table 2.3: The effective indices of the first five guided modes of the slot waveguide

Effective indices of guided modes				
1	2	3	4	5
2.008	1.9248	1.9113	1.8386	1.7962

2.6.2 Study of the "ridge waveguide"

The ridge waveguide, as shown in figure 2.14 a, is a common waveguide structure. This work was theoretically and experimentally studied by our team in the references [40, 37]. The ridge waveguide was fabricated from $500\mu m$ thick lithium niobate wafer. A Ti indiffusion process is first performed in order to gradually modify the refractive index of $LiNbO_3$ along the wafer thickness (planar waveguide is obtained). Then, a $48\mu m$ height ridge is obtained by optical-grade dicing to get lateral confinement 2.14 b. The obtained ridge waveguide is then located at the top of the ridge where the refractive index gradient exists. The fundamental guided mode of the structure is excited inside this top region such that there is no need to consider all the $48\mu m$ ridge height. In our simulations, the modeled region has $4\mu m \times 7\mu m$ size along x and y directions respectively. Uniform meshing is applied with $\Delta x = \Delta y = 50$ nm. The eigenmodes of the structure are determined at an operation wavelength of $\lambda = 1.5\mu m$.

Table 2.4 gives the effective indices of the first 5 guided modes in the structure. The spatial distribution of electric field amplitude of the fundamental guided mode is presented

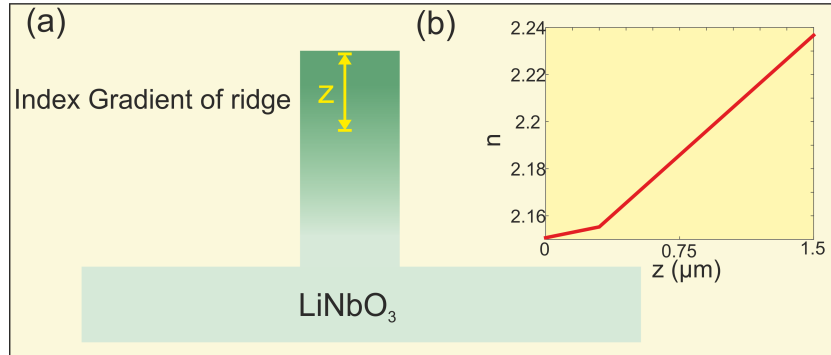


Figure 2.14: a) Scheme of lithium niobate ridge waveguide. b) The refractive index variations along the vertical direction of the lithium niobate ridge waveguide.

Table 2.4: The effective indices of the first five guided modes of the ridge waveguide

Effective indices of guided modes				
1	2	3	4	5
2.1270	2.1249	2.1173	2.1202	2.1114

in figure 2.15 a. One can observe the high confinement of electromagnetic field at the top of the ridge waveguide leading to excellent guiding properties (vertical and lateral confinement). In comparison, we also performed simulations in the case of step-index ridge waveguide (without Ti indiffusion). Figure 2.15 b shows the fundamental guided mode electric field distribution where the guided mode appears far from the top of the ridge. This result demonstrates the need of Ti indiffusion to bring up the light confinement in order to enhance its interaction with a possible nano-structuration (PC) on the top of the ridge. In the next, we study how the mode center moves vertically as a function of the index gradient. For this purpose, we keep the same gradient behavior and we only varies the value of its maximum (n_{max}). This experimentally may correspond to modifying the Ti dose or the time of the indiffusion process. Figure 2.16 shows the fundamental guided mode center displacement δ as a function of n_{max} with $\Delta = 0$ corresponding to a step-index ridge waveguide (no gradient). For small variation of n_{max} , figure 2.16 show a quite linear behavior of δ with a slope of $\frac{\Delta\delta}{n_{max}} \simeq 19 \frac{\mu m}{RIU}$. This results can be exploited to determine the Ti indiffusion process parameters to be compatible (efficient interaction)

with a given nano-patterning depth on the top of the ridge. As a conclusion, the FDFD developed code seems to be a powerful tool for the study of dielectric waveguides whatever their geometries.

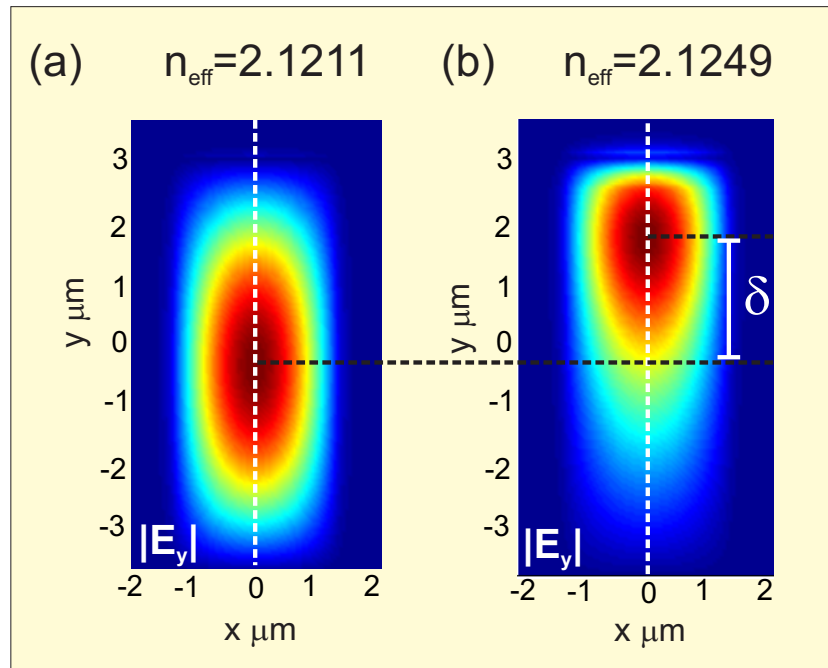


Figure 2.15: a) Electric field distribution of fundamental mode for lithium niobate ridge waveguide index gradient. b) Electric field distribution of fundamental mode for lithium niobate ridge waveguide without index gradient. c)

2.7 Conclusions

In this chapter, we explained all concepts and theoretical fundamentals (basics of finite difference approximation, numerical tools,...) to understanding the method that was used for the theoretical study of waveguide. The FDFD method is depending on use a Yee grid. The FDFD method offers the following advantages: (1) The simulation by using the frequency domain method is very faster because its response for a few required frequencies. (2) It depends on the properties of materials such as dispersion. Also, a lot of literature

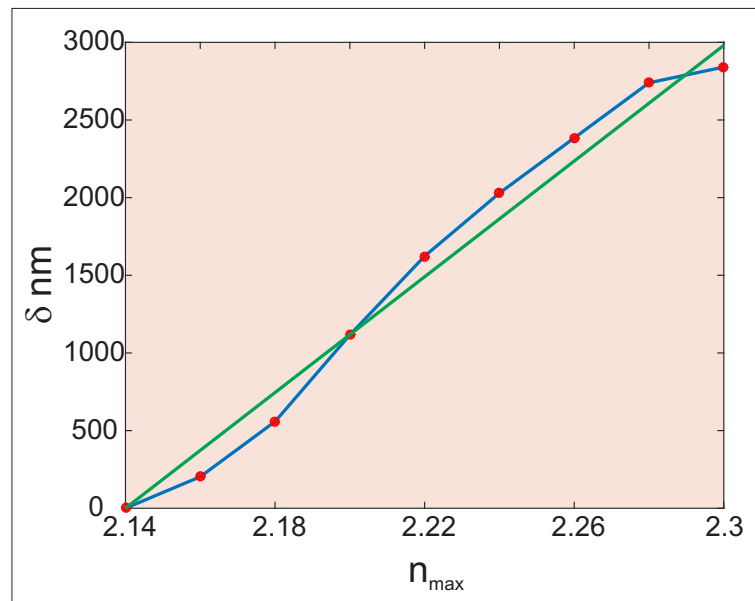


Figure 2.16: Differential between index gradient and non gradient

on finite-difference time-domain (FDTD) methods applies to FDFD, especially subjects on how to represent materials and devices on a Yee grid. We verified our code with other published results. We achieved excellent guided mode for all tests and applications and good agreement with their results was obtained. Consequently, the FDFD method is suitable and very simple. But as it has advantages also it has drawbacks, it has some difficulties such as the large dimensions grid more than (120×120) takes long time for calculations and large memory. The modeling metallic nano structures will be described in following chapters.

Chapter 3

Electromagnetic Force

3.1 Introduction

The electromagnetic force is one of the four basic forces in nature, being weaker than the strong nuclear force but stronger than the weak nuclear force and the gravity. So, the electromagnetic force is the second strongest force. The action of light on object has been known for a long time. In fact, around 1616, Johannes Kepler observed that the comet tail is always pointed in the opposite direction from the sun position, he assumed that this is a result of radiation pressure exerted by sun light on ice crystals and dust constituting the comet tail [41]. This force will be later called "radiation pressure" [42]. Even before the contrivance of lasers, observations with detailed experimental devices proved the existence of radiation pressure qualitatively and quantitatively [43]. This phenomenon led the researchers to exploit the electromagnetic force for particles manipulation. In our work we will use two type of the nanoantenna as optical tweezers. Let us see in the following section optical tweezers evolutions.

3.2 Introduction of optical tweezers

Optical micro manipulation as a mean to selectively trap and move small particles, however it requires very high intensity gradients that are only possible with laser light sources. This field of activities was begun almost 40 years ago by Ashkin in his innovative paper on acceleration and trapping of particles by radiation pressure [44], who used a weakly focused laser beam in order to guide particles. He not only observed the acceleration of microscopic particles by the radiation force but also noticed a gradient force, pulling transparent particles with an index of refraction higher than the host medium towards the beam axis.

Furthermore, he suggested and demonstrated the notion of counter-propagating optical trapping, where the opposed radiation pressure of two laser beams leads to the stable three-dimensional confinement of particles. Soon, other stable optical traps were demonstrated, including the optical levitation where gravitational forces are compensated by the radiation pressure [44, 45]. The main achievement in the field of optical micro manipulation was the demonstration of a single beam gradient force trap, which is nowadays known as optical tweezers [2, 46] as shown in figure 3.1. In optical tweezers, a single laser beam is very strongly focused through a high numerical aperture lens, this means achievement of gradient forces that counterbalances the scattering forces in propagation direction. This simple and elegant implementation of an optical trap allows the stable three-dimensional optical trapping of dielectric particles. Based on these essential findings, a whole field of optical micro manipulation has been advanced.

This latter have attracted intense research interests in the past years due to their unique ability to manipulate tiny objects without contact. Optical tweezers have been successfully used in manipulating a large panel of physical object and biological entities

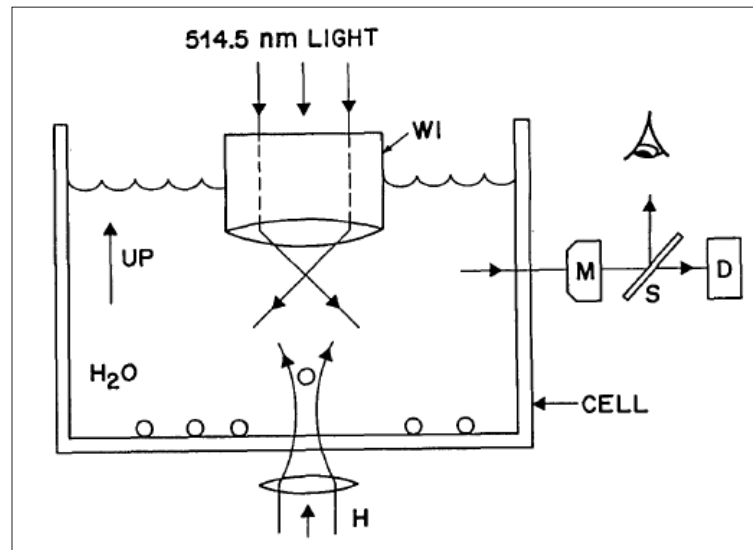


Figure 3.1: Schema of optical trapping system of Mie and Rayleigh particles in water by a single-beam gradient force radiation-pressure trap [2]

[47]. However, optical tweezers are often restricted, both in size of trapped particles and in compactness, to being generated by diffraction limited bulky optics, and it remains a key fundamental challenge to realize optical tweezers capable of manipulating sub-micron particles in a versatile and flexible configuration. A way of addressing this issue is to make use of optical fibers which avoid the use of complex bulky optics to direct photons. An alternate configuration involving an apertureless metal probe and a dielectric nanosphere illuminated in total internal reflection regime, has been investigated by Chaumet et al [3] as shown in figure 3.2. All these authors have theoretically analyzed and demonstrated the possibility of using the metal tip to pick up and move particles above a substrate.

On the one hand, optical tweezers have been further developed towards multilateral, multifunctional tools by means of time-sharing approaches, holographic beam-shaping, and an uncountable number of technological refinements[48, 49]. On the other hand, a wide range of another approaches has appeared that go beyond the concept of single or multiple detached optical tweezers but supply optical landscapes, designed to a specific problem. Manipulation of small particles by immaterial probes such as intense light

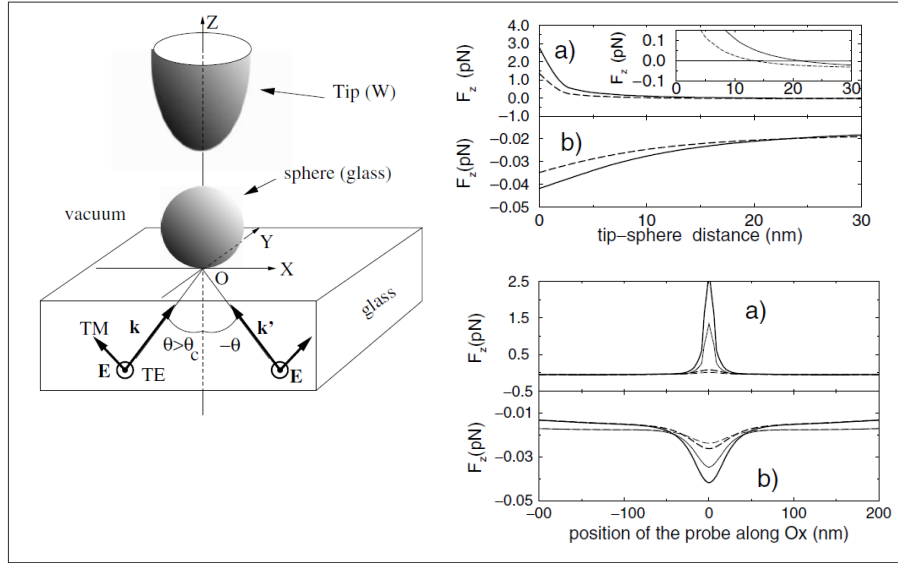


Figure 3.2: a) Tungsten probe of an apertureless near-field microscope. b) Z-component of the force experienced by the sphere versus the distance between the tip and the sphere. c) Force along-z experienced by the sphere as a function of the lateral position of the probe. The sphere is at the origin.[3].

beams has attracted a lot of researches both theoretically and experimentally [50, 51, 52]. If we neglect the radiation pressure that is inadequate for optical trapping, the electromagnetic forces generated on such micro-structures mainly depend on the spatial gradient of the electro-magnetic field. More spatially localized the light confinement is, higher the gradient is and more intense the force is. Consequently, Scanning Near-field Optical Microscopy (SNOM) facilities were proposed till 1997 by Novotny et al. [4] to use the electric field enhancement (tip effect) at a metallic tip apex as optical tweezers to trap nanometer-sized dielectric particles. Figure 3.3 shows the potential energy in xz-plane for nanoparticle having radius only 10 nm where the potential well which was obtained is equal to $25 \text{ kT}/W$ along x,z direction respectively as shown in figure 3.3 b,c.

A similar theoretical result was obtained by [53, 54, 55] for a nanoparticle placed near a sub-wavelength aperture made in metallic film. Unfortunately, the resonance wavelength

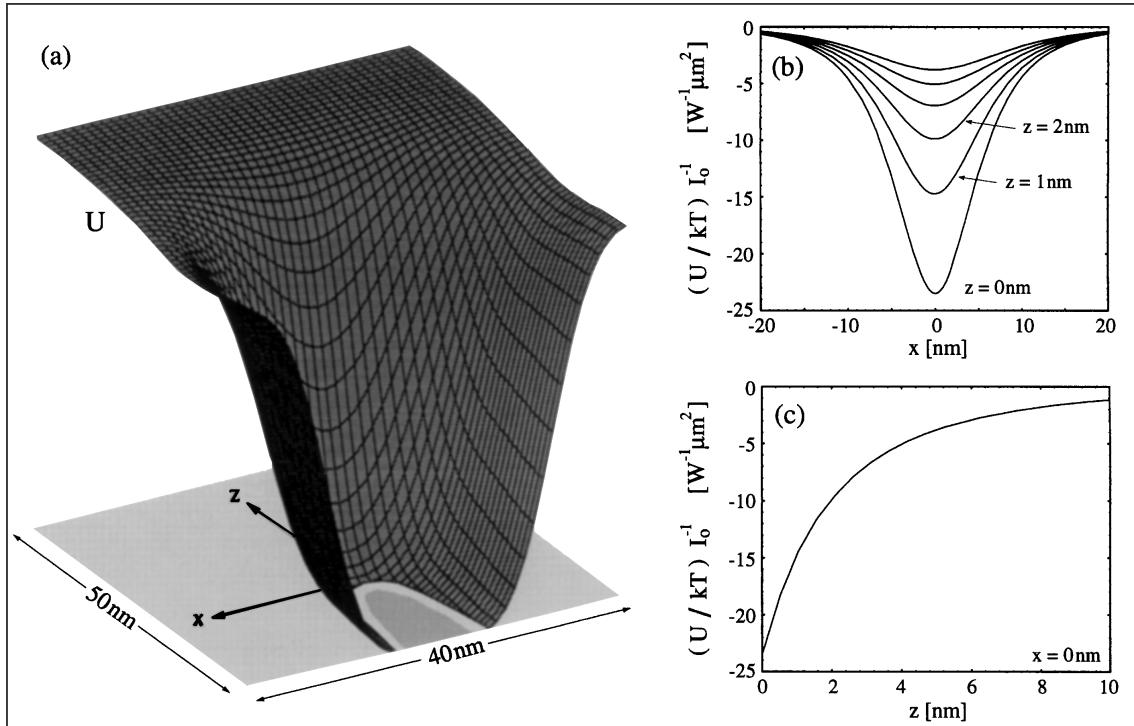


Figure 3.3: Trapping potential of a particle ($d = 10\text{nm}, \epsilon = 2.5$) in the vicinity of the tip. (a) Potential energy surface in the (xz) plane (the tip is indicated by the shadow on the bottom plane). (b),(c) Normalized potential energy evaluated along the x and z directions, respectively[4].

of the particle depends on its size (volume) and on its dielectric constant through the expression of its polarizability. Thus, it is necessary to adapt the operation wavelength, i.e. the particle dimensions and metal nature, to the fluid that must have small absorption at this wavelength. Nonetheless, conventional homogeneous electromagnetic fields are inconsistent with single particle trapping when the dimensions of the latter is small compared to the wavelength. This obstacle, related to the diffraction limit given by the Rayleigh criterion, can be bypassed by the consideration of non propagative waves such as evanescent ones created by diffraction of light by sub-wavelength features [56]. All these authors have theoretically analyzed and demonstrated the possibility of using the metal tip to pick up and move particles above a substrate.

On the other hand, some studies proposed to use optical tweezers to perform fine

positioning of nanoshells inside human tissues [57, 58] in view of use in nanomedicine. However, optical tweezers are now designed for a large range of applications covering several domains such as physics, chemistry and medicine. Recently, researchers have demonstrated the ability to surpass the limits imposed by free-space diffraction by tailoring the optical and structural properties of a medium [59]. For example, Grigorenko et al [60] utilized the strongly enhanced and localized optical near-fields of closely spaced metallic nanostructures. Similarly Yang et al [61] were able to demonstrate optical trapping and transport of dielectric nanoparticles by exploiting the strong field confinement within slot waveguides [23, 62, 63]. The strength of optical traps can be enhanced by the strong confinement of the optical field and it can also be improved by exploiting the field amplification within an optical resonator. Interesting numerical study [5] of the light emitted by a single coaxial aperture figure 3.4a demonstrated a stable optical trapping of dielectric particle as small as 2 nm diameter. Figure 3.4 b shows transverse trapping potential produced by the transverse optical force components (F_x and F_y) as well as the pulling force (F_z) on a 10 nm dielectric particle (index $n = 2$) placed 20 nm away from the coaxial aperture, normalized by 100 mW of the power transmitted through the coaxial aperture. The cross sections of the transverse optical trapping potential (U_{xy}) shows potential well achievement equal to 25 kT/100 mW as shown in figure 3.4 c .

Thereby, it is well known that small dielectric spheres can be trapped by conventional gaussian beams while metallic ones are ejected out from the center of the beam [64, 65]. In fact, in the case of micro-sized particles, the light cannot penetrate inside the particle and the radiation pressure becomes predominant. Recently, optical trapping of micro particles was demonstrated inside hollow optical fiber [66] and also by using a dual tapered fiber tweezers [67, 6]. Figure 3.5 shows Optical trapping of 12 nm silica spheres using a double nanohole at 15 nm tip separation. In that paper, the authors showed the possibility of trapping simultaneously more than one particle and they also

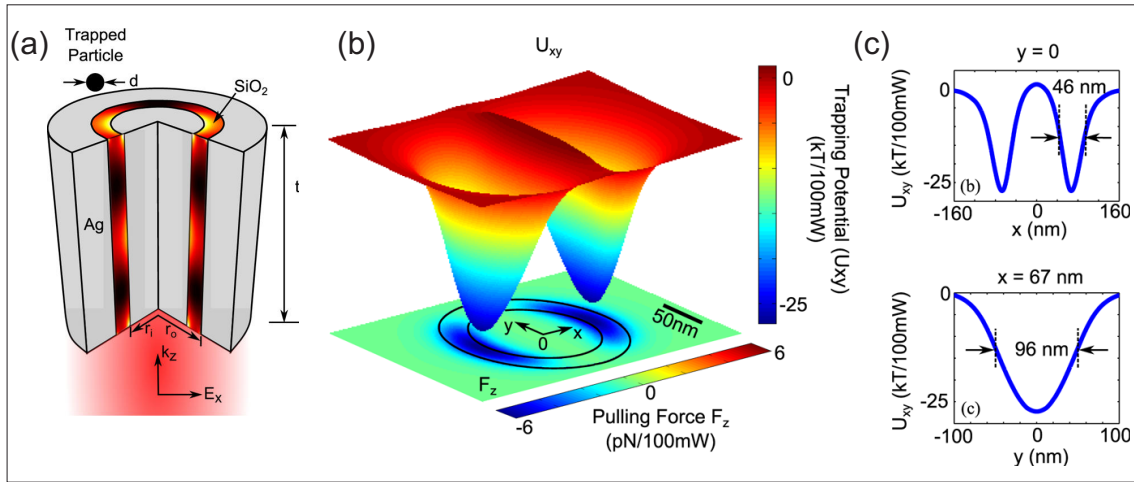


Figure 3.4: (a) Schematic of the coaxial plasmonic aperture and the potential well in the xOy transverse plane. (b) Transverse trapping potential on a 10 nm dielectric placed at 20 nm away from the coaxial aperture. (c) Cross sections of the transverse optical trapping potential (U_{xy}) along $x = 0$ nm and $y = 67$ nm. The trapping potential full-width at half-maximum is indicated in each direction [5].

established a metastable regime. Thus, far-field measurements are usually performed to prove this trapping through the detection of a near-field information that can be linked to the particle position (Rayleigh scattering, fluorescence, ...). However, nano-sized metallic particles trapping is possible but needs to excite the particle resonance (resonant trapping) [68].

Maxwell stress tensor can be considered as powerful method for optical force calculations. In fact, this method was qualified as critical for practical force calculations in numerical codes. There are three reasons making the MST more appropriate than other methods: (1) The accuracy of the result is not affected by the current density distribution inside the object. (2) The enclosed surface of the object does not need to be compatible with its surface. (3) The integral depends only on the field distribution outside the object. Moreover, it is not necessary to know the electromagnetic field distribution within complex anisotropic or nonlinear materials. Consequently, MST method will be applied in all our following calculations of optical forces.

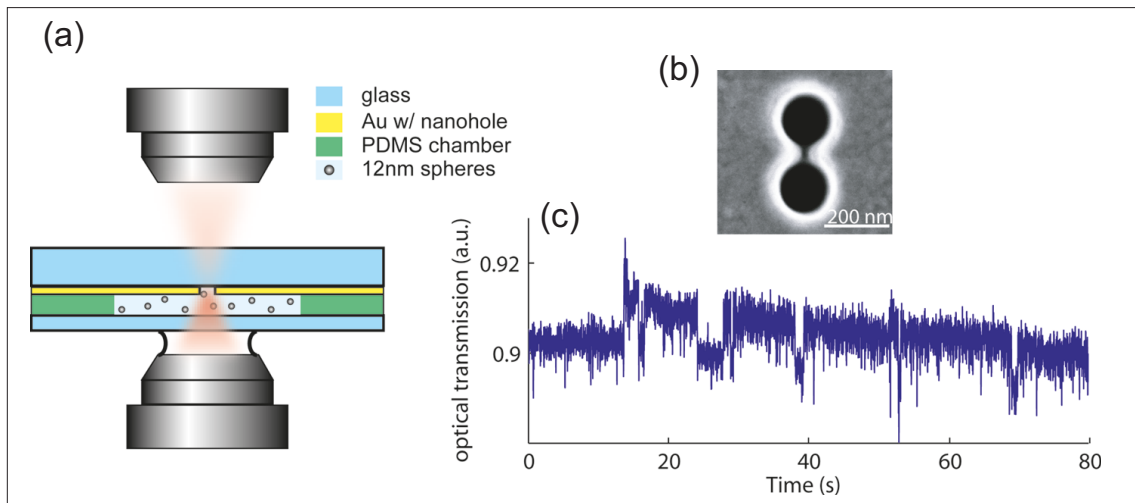


Figure 3.5: Schema of the nanoscale double-hole. b) SEM image of the double-hole on Au film taken normal to the surface. c) Optical trapping of 12 nm silica spheres using a double nanohole at 15 nm tip separation [6].

One of the most innovative methods to solve the Maxwell's equations is the finite difference time-domain (FDTD). The FDTD method is now widely employed to simulate light-matter interaction in nanooptics [69, 70, 71, 72, 73]. As well, the FDTD method is used to calculate the total electromagnetic field in any computational volume that contains the structure under study. As it will be shown, optical forces are then derived through the determination of the Maxwell stress tensor which can be easily calculated through the knowledge of the EM field surrounding the particle. This field is a priori determined by FDTD. In this chapter, we will present some basic of mechanical action of light and electromagnetic theory and show how optical forces arise on dielectric particles. The developed numerical tools are then tested and results are compared to literature to demonstrate the validity of our codes.

3.3 Mechanical action of light and gradient force

The light is composed of photons with energy and a quantity of movement. When a photon hits a particle, there is a transfer of momentum. The light exerts on the particle known as a radiation pressure [46, 2] that is essentially directed toward the propagation direction. In addition, if the illumination is non homogeneous, transverse force can be induced. Thus, optical forces are derived of two essential component: the gradient force, which pushes the particle in the opposite direction of the incidence light propagation, or towards the focus of the laser beam. The scattering force, which pushes the particle in the direction of the incidence light propagation, or away from the light source. In figure 3.6 we can see that when A incident laser beam meet the interface, some is reflected and some is refracted. The focus of the cone of light is on the point F_g inside the sphere.

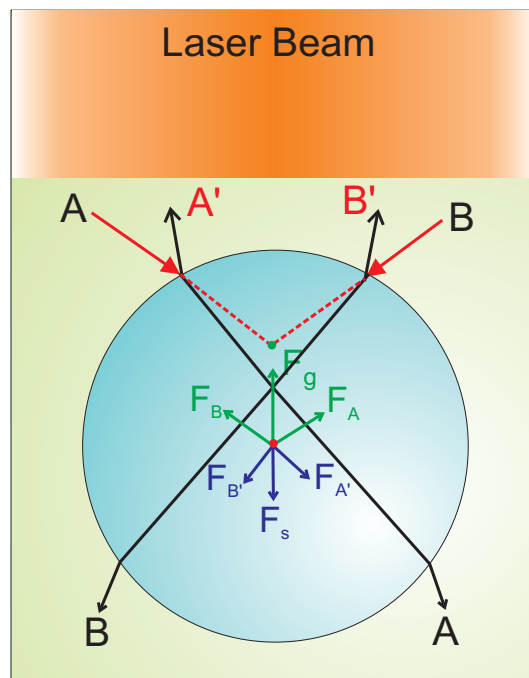


Figure 3.6: Scattering and gradient forces created by non homogeneous optical illumination on a dielectric particle.

In the case of a focused laser beam, this force pulls the particle radially into the axis

of the beam as well as axially into the focal point of the beam. In order to achieve the gradient force, the axial component must be greater in magnitude than the axial scattering force (see figure 3.7 a). This can be fulfilled in the case of highly focused beams as shown on figure 3.7 a. Otherwise, if the scattering force is greater in magnitude than the axial component of the gradient force the laser guidance is realized and weakly focused beam causes particle to be pushed (guided) along the beam axis as shown in figure 3.7 b.

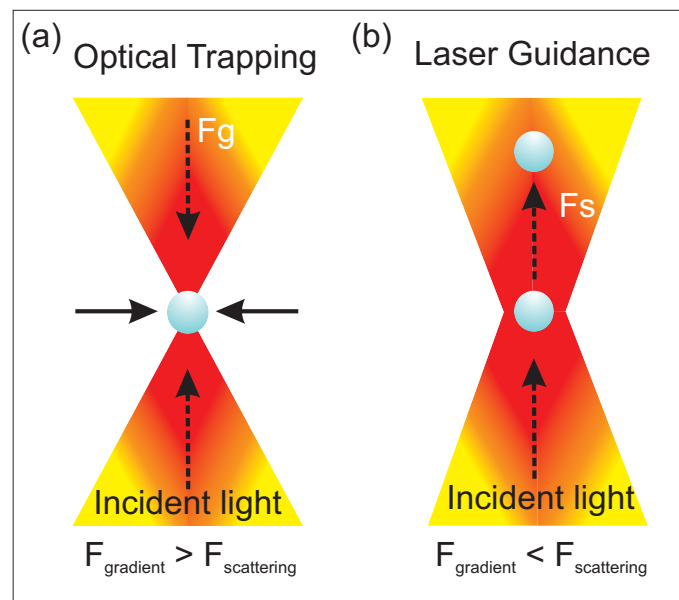


Figure 3.7: (a) Optical trapping. (b) Laser guidance.

Light-matter interaction at the nano-scale leads basically to light confinement at the edges of nano-structures (SNOM tip apex for instance or any resonance type). This very enhanced electromagnetic field gradient can be exploited to locally generate efficient optical forces able to trap small nanoparticles.

3.4 Basics of the electromagnetic Force

The electromagnetic force (or Lorentz force) is the force that will undergo a charged particle placed in an electromagnetic field. It causes all electric and magnetic interactions. An electromagnetic field exerts on a particle having a non-zero electric q charge, a total force that is given by the sum of two terms: an electric term (Coulomb force) and a magnetic term (Lorentz force):

$$\vec{F} = q (\vec{E} + \vec{v} \times \vec{B}) \quad (3.1)$$

Where \vec{E} and \vec{B} are respectively the electric and the magnetic fields, \vec{v} represents the velocity of the particle with respect to a defined Galilean reference system. Thus, for a small dielectric particle placed in homogeneous electromagnetic field, two Coulomb forces appear and act on detached charges in opposite directions (induced dipole) even if the electric field oscillates (dipole direction changes). So, when the particle is illuminated by a plane wave (PW), the EM field around it presents two different characteristics: (1) lateral distribution remains symmetrical so lateral forces compensate each other while (2) axial distributions are necessary non-symmetrical (due to the illumination). Thus, the induced dipoles on the two axial lobes of the particle are different and their resulting action tends to push the particle in the propagation direction. Figure 3.8 explicitly illustrates the two cases of uniform and nonuniform lateral electric field. The same schema can be applied for axial forces. To take into account the redistribution of the EM field around the particle (due to light-matter interaction), FDTD simulations were performed and corresponding results are shown on figure 3.9. Both PW and Gaussian incident beams were considered. For the latter, off-centered illumination of the spherical particle is also studied in order to point out the apparition of lateral gradient force component. On the contrary, when the

electric field is non-uniform (Gaussian beam for example) and has a gradient along one direction, then Coulomb forces do not compensate each other anymore. In this case the resulting force [which is called gradient force] is not equal to zero, and pushes the particle towards the stronger field intensity position as shown in figures 3.8 c,d and 3.9 c.

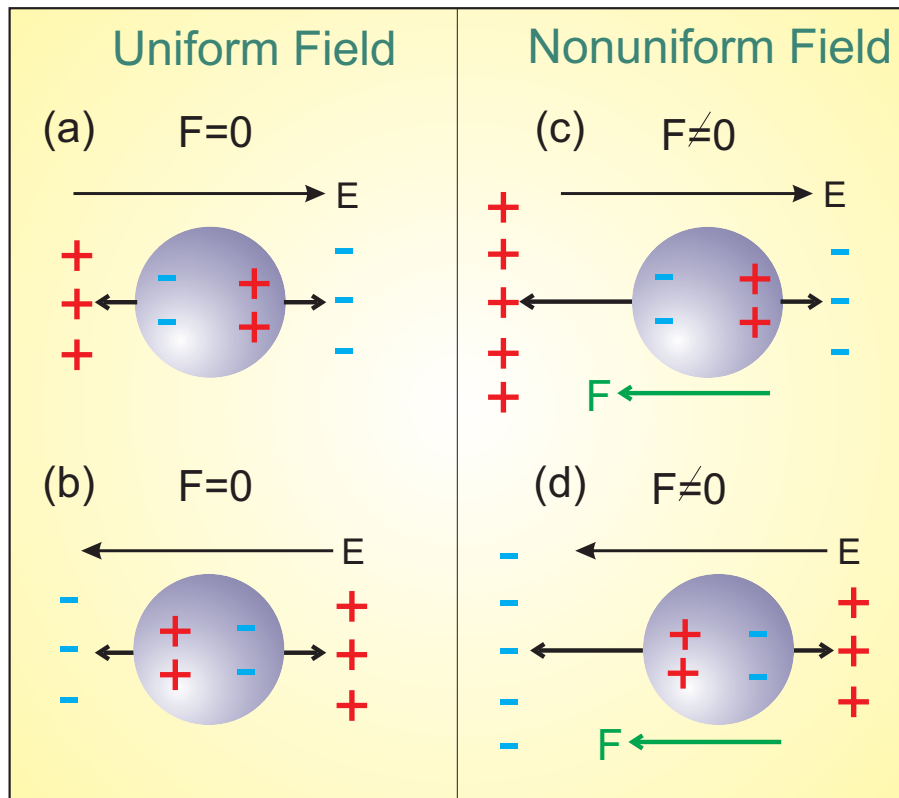


Figure 3.8: A dielectric particle polarization in accordance with:(a,b) uniform field (c,d)non uniform electric field; c) and d) shows that at change of the electric field sign the direction of the gradient force does not change.

Nevertheless, a scattering force also exists and tends, generally, to drive the particle in the propagation direction. In order to get a stable optical trapping, the scattering force must be smaller than the gradient one. As an example, for a small particle ($n=1.65$) of $95nm$ diameter immersed in water, the gradient force becomes 3 times larger than the scattering force if the Gaussian beam spot size is equal to $w_0 = 0.75\lambda = 260nm$ [2]. For such a small particle (Rayleigh regime) illuminated by Gaussian or Gaussian-Hermite beams, the determination of the optical forces can be conducted analytically

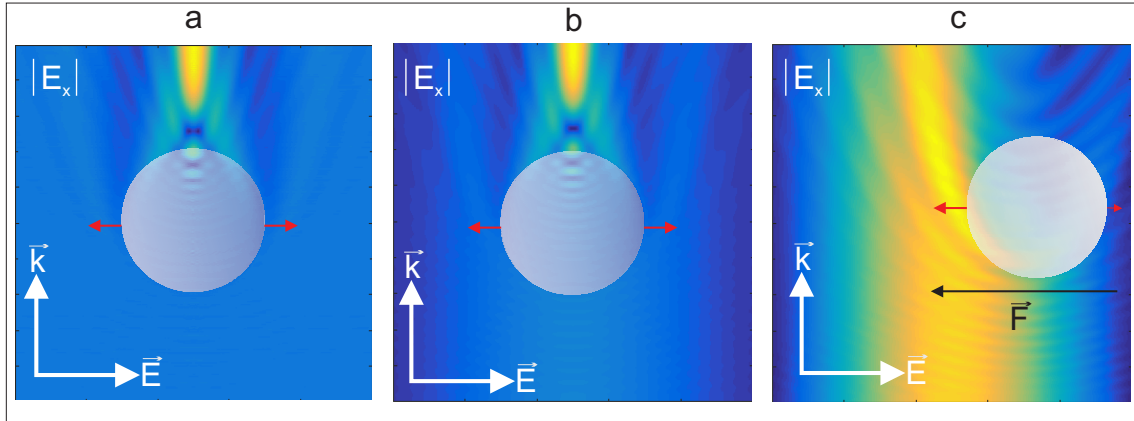


Figure 3.9: Numerical simulation of a dielectric particle is illuminated with: a) Plane wave. b) Gaussian Beams. c) Off-centered spherical particle illuminated by Gaussian Beams.

[74, 75]. Unfortunately, for the general case where bigger particles having any shape and in presence of any electromagnetic field distribution, the determination of the optical force becomes difficult and numerical tools are generally needed. The latter are derived from the expression of the electromagnetic force eq. 3.1 through Maxwell equations.

3.4.1 Electromagnetic force per unit volume: Formulation of MST expression

Let us consider a charge distribution, with volume density ρ , submitted to an electromagnetic field (\vec{E}, \vec{B}) . The force exerted on an elementary charge $dq = \rho d\tau$ contained within an elementary volume $d\tau$, moving at the overall velocity \vec{v} , can be written $d\vec{f} = (\rho\vec{E} + \vec{j} \times \vec{B})d\tau$ where \vec{j} is the current surface density given by $\vec{j} = dq \cdot \vec{v}$. Thus, we define the force per unit volume for an unknown charge distribution as:

$$\vec{f} = \rho\vec{E} + \vec{j} \times \vec{B} \quad (3.2)$$

Next, ρ and \vec{j} can be replaced by the fields \vec{E} and \vec{B} , using Gauss's and Ampere's laws:

$$\vec{f} = \varepsilon(\nabla \cdot \vec{E})\vec{E} + \frac{1}{\mu}(\nabla \times \vec{B}) \times \vec{B} - \varepsilon \frac{\partial \vec{E}}{\partial t} \times \vec{B} \quad (3.3)$$

This expression of the electromagnetic force involves both electric and magnetic fields and the properties of the medium (ε, μ) .

The last term, which is a time derivative, can be rewritten differently in order to be interpreted physically. In fact, by injecting the Poynting vector ($\vec{P} = \vec{E} \times \frac{\vec{B}}{\mu}$) and using the product rule :

$$\frac{\partial}{\partial t} \vec{P} = \frac{\partial \vec{E}}{\partial t} \times \vec{B} + \vec{E} \times \frac{\partial \vec{B}}{\partial t} \quad (3.4)$$

$$= \frac{\partial \vec{E}}{\partial t} \times \vec{B} - \vec{E} \times (\nabla \times \vec{E}) \quad (3.5)$$

By using Maxwell-Faraday equation eq. 2.1 we get finally:

$$\vec{f} = \varepsilon \left[(\nabla \cdot \vec{E})\vec{E} - \vec{E} \times (\nabla \times \vec{E}) \right] + \frac{1}{\mu} \left[-\vec{B} \times (\nabla \times \vec{B}) \right] - \varepsilon \frac{\partial}{\partial t} (\vec{P}) \quad (3.6)$$

In order to get symmetrical expression in \vec{E} and \vec{B} , we insert the term $(\nabla \cdot \vec{B})\vec{B}$ which is zero and get:

$$\vec{f} = \varepsilon \left[(\nabla \cdot \vec{E})\vec{E} - \vec{E} \times (\nabla \times \vec{E}) \right] + \frac{1}{\mu} \left[(\nabla \cdot \vec{B})\vec{B} - \vec{B} \times (\nabla \times \vec{B}) \right] - \varepsilon \frac{\partial}{\partial t} (\vec{P}) \quad (3.7)$$

At first glance, this expression is difficult to be interpreted. To simplify it, we can use the vector identity:

$$\frac{1}{2}\vec{\nabla}A^2 = \vec{A} \times (\nabla \times \vec{A}) + (\vec{A} \cdot \vec{\nabla})\vec{A} \quad (3.8)$$

From this expression, we deduce that:

$$\vec{E} \times (\nabla \times \vec{E}) = -(\vec{E} \cdot \vec{\nabla})\vec{E} + \frac{1}{2}\vec{\nabla}E^2 \quad (3.9)$$

and

$$\vec{B} \times (\nabla \times \vec{B}) = -(\vec{B} \cdot \vec{\nabla})\vec{B} + \frac{1}{2}\vec{\nabla}B^2 \quad (3.10)$$

By substituting these last equations 3.9,3.10, in the equation 3.7, we get:

$$\begin{aligned} \vec{f} = \varepsilon \left[(\nabla \cdot \vec{E})\vec{E} + (\vec{E} \cdot \vec{\nabla})\vec{E} \right] + \\ \frac{1}{\mu} \left[(\nabla \cdot \vec{B})\vec{B} + (\vec{B} \cdot \vec{\nabla})\vec{B} \right] - \frac{1}{2}\vec{\nabla}(\varepsilon\vec{E}^2 + \frac{1}{\mu}\vec{B}^2) - \varepsilon\frac{\partial}{\partial t}(\vec{P}) \end{aligned} \quad (3.11)$$

Finally, to simplify this equation 3.11 we can rewrite it as:

$$\vec{f} = \nabla \cdot \overset{\leftrightarrow}{T} - \varepsilon\frac{\partial}{\partial t}(\vec{P}) \quad (3.12)$$

Where the tensor $\overset{\leftrightarrow}{T}$, named the Maxwell Stress Tensor, satisfies the expression:

$$\overset{\leftrightarrow}{T}_{ij} = \varepsilon(E_i \cdot E_j - \frac{1}{2}\delta_{ij}\vec{E}^2) + \frac{1}{\mu}(B_i \cdot B_j - \frac{1}{2}\delta_{ij}\vec{B}^2) \quad (3.13)$$

Consequently, the electromagnetic field in a linear medium of relative dielectric permittivity ε_r and magnetic permeability μ is represented mathematically by this Maxwell stress tensor $\overset{\leftrightarrow}{T}$ which is (3×3) matrix. Let us recall that δ_{ij} is the Kronecker symbol for $i, j = x, y, z$.

We arrive at a simple relation expressing the electromagnetic forces per unit volume based on the divergence of MST and Poynting vector which gives us the energy flow eq.3.12. So, let us see in next section how we can calculate the total optical force exerted on an illuminated particle.

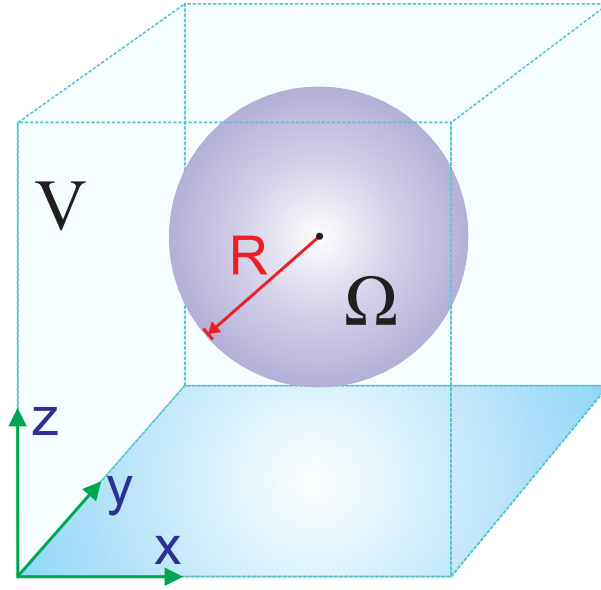
3.4.2 Total force on a particle included in a volume V

To calculate the total force exerted by electromagnetic fields on a particle (see figure 3.10), we have simply to apply the integration of the force density over all its volume as follows:

$$\vec{F} = \iiint_{\Omega} (\nabla \cdot \overset{\leftrightarrow}{T} - \varepsilon_0 \frac{\partial}{\partial t} (\vec{E} \times \vec{B})) d\tau \quad (3.14)$$

where Ω is particle volume. The first term, we apply Ostrogradski-Green theorem, which express the equality between this integral and the flux of $\overset{\leftrightarrow}{T}$ through the boundary of the volume V (which is a surface integral). This can be expressed as:

$$\forall V \supset \Omega, \iiint_V (\nabla \cdot \overset{\leftrightarrow}{T}) d\tau = \oiint_S \overset{\leftrightarrow}{T} \cdot \vec{n} ds \quad (3.15)$$

Figure 3.10: A particle included in a volume V .

\vec{n} represents the local normal vector to the surface. Consequently, the expression of the total force becomes:

$$\vec{F} = \oiint_S \overset{\leftrightarrow}{T} \cdot \vec{n} \, ds - \varepsilon_0 \frac{\partial}{\partial t} \iiint_V \vec{E} \times \vec{B} \, d\tau \quad (3.16)$$

The electromagnetic forces on a volume can be determined from the knowledge of the Maxwell stress tensor only calculated over the surface delimiting the same volume. The latter involves electric permittivity and magnetic permeability of the medium at the surface (outside the volume itself) .

Since the number of field lines generated the charge q depends only on the magnitude of the charge, any arbitrarily shaped surface that encloses q will intercept the same number of field lines. So, we are finally able to calculate the total force applied to a volume V knowing only the field on a surface S surrounding this volume. S is then any bounded surface delimiting the volume V that encloses the particle. One notice that S

must be completely located in the same medium surrounding the particle and cannot intersect any other one. For sake of simplicity, we assume a cube centered on the particle and we only record the electromagnetic field over its six faces. This condition on the choice of the surface will limit the calculation of the force to the contactless cases between the particles and another material (substrate or nano-antenna for example).

In our work, the electromagnetic field exhibits very rapid oscillations so that only the average effects over a period are observed. Thus :

$$\frac{\partial}{\partial t} \langle \iiint_V \vec{E} \times \vec{B} d\tau \rangle = 0 \quad (3.17)$$

And the force expression becomes :

$$\vec{F} = \oint_S \langle \vec{T} \rangle \cdot \vec{n} ds \quad (3.18)$$

As we can see, the force can be calculated through the value of electromagnetic field over any external closed surface containing the whole volume on which it is exerted. In this regime and working in complex notations, the expression of the Maxwell stress tensor becomes:

$$\overset{\leftrightarrow}{T} = \begin{bmatrix} T_{11} & T_{12} & T_{13} \\ T_{21} & T_{22} & T_{23} \\ T_{31} & T_{32} & T_{33} \end{bmatrix} \quad (3.19)$$

Where:

$$\begin{aligned}
T_{11} &= \frac{1}{4} [\varepsilon_0 (| E_x |^2 - | E_y |^2 - | E_z |^2) + \frac{1}{\mu_0} (| B_x |^2 - | B_y |^2 - | B_z |^2)] \\
T_{12} &= \frac{1}{2} [\varepsilon_0 \cdot \text{Re}(E_x E_y^*) + \frac{1}{\mu_0} \cdot \text{Re}(B_x B_y^*)] \\
T_{13} &= \frac{1}{2} [\varepsilon_0 \cdot \text{Re}(E_x E_z^*) + \frac{1}{\mu_0} \cdot \text{Re}(B_x B_z^*)] \\
T_{21} &= \frac{1}{2} [\varepsilon_0 \cdot \text{Re}(E_x E_y^*) + \frac{1}{\mu_0} \cdot \text{Re}(B_x B_y^*)] \\
T_{22} &= \frac{1}{4} [\varepsilon_0 (| E_y |^2 - | E_x |^2 - | E_z |^2) + \frac{1}{\mu_0} (| B_y |^2 - | B_x |^2 - | B_z |^2)] \\
T_{23} &= \frac{1}{2} [\varepsilon_0 \cdot \text{Re}(E_y E_z^*) + \frac{1}{\mu_0} \cdot \text{Re}(B_y B_z^*)] \\
T_{31} &= \frac{1}{2} [\varepsilon_0 \cdot \text{Re}(E_x E_z^*) + \frac{1}{\mu_0} \cdot \text{Re}(B_x B_z^*)] \\
T_{32} &= \frac{1}{2} [\varepsilon_0 \cdot \text{Re}(E_y E_z^*) + \frac{1}{\mu_0} \cdot \text{Re}(B_y B_z^*)] \\
T_{33} &= \frac{1}{4} [\varepsilon_0 (| E_z |^2 - | E_x |^2 - | E_y |^2) + \frac{1}{\mu_0} (| B_z |^2 - | B_x |^2 - | B_y |^2)]
\end{aligned}$$

Where $E_y^*, E_z^*, B_y^*, B_z^*$ are complex conjugates of E_y, E_z, B_y, B_z respectively.

This definition of the force through the Maxwell stress tensor is, of course, consistent and valid in both electrostatics and magnetostatics. The next section is dedicated to analytically demonstrate the equivalence between equation 3.18 and the well-known Coulomb (electrostatics) and Lorentz (magnetostatics) forces. (3.4.3).

3.4.3 The electro and magneto statics force

In the case where a static electric field \vec{E} is applied on a charge distribution of density ρ over a total volume V , the force density and the total force are given through the Coulomb

law, eq.3.2 by:

$$d\vec{F} = \vec{E}(r)\rho(r)dV \quad (3.20)$$

$$\text{and } \vec{F} = \int_V \vec{E}(r)\rho(r)dV \quad (3.21)$$

respectively, where the volume of integration is any volume including all the charges. By replacing ρ with $div(\vec{E})$ to get:

$$\vec{F} = \epsilon \iiint_V \vec{E}(r)\nabla \cdot \vec{E}dV \quad (3.22)$$

Given the fact that the derivatives are in fact a vector operator, we have to be a bit careful in treating them as simple derivatives. This is done by using the standard "Vector Formulas", through:

$$\nabla \cdot [\Psi C] = C \cdot \nabla \Psi + \Psi \nabla \cdot C \quad (3.23)$$

There is however a complication: the scalar quantity in this formula (Ψ) is, in the equation we want to transform, the vector \vec{E} . Consequently, we need to transform the vectorial equation into 3 scalar ones since: $\vec{E} = E_x \cdot \vec{i} + E_y \cdot \vec{j} + E_z \cdot \vec{k}$. The vector formula above will be applied three times taking as scalar functions the three components of \vec{E} .

$$\vec{F} = \varepsilon \int_V \left[\vec{i} E_x (\nabla \cdot \vec{E}) + \vec{j} E_y (\nabla \cdot \vec{E}) + \vec{k} E_z (\nabla \cdot \vec{E}) \right] dV \quad (3.24)$$

$$\begin{aligned} \vec{F} = \varepsilon & \left[\vec{i} \int_V \left(\nabla \cdot (E_x \vec{E}) - \vec{E} \cdot \nabla E_x \right) dV \right. \\ & \left. + \vec{j} \int_V \left(\nabla \cdot (E_y \vec{E}) - \vec{E} \cdot \nabla E_y \right) dV + \vec{k} \int_V \left(\nabla \cdot (E_z \vec{E}) - \vec{E} \cdot \nabla E_z \right) dV \right] \quad (3.25) \end{aligned}$$

Using Ostrogradsky theorem, we obtain:

$$\begin{aligned} \vec{F} = \varepsilon & \left(\oiint_S [\vec{i} E_x \vec{E} \cdot \vec{n} \right. \\ & \left. + \vec{j} E_y \vec{E} \cdot \vec{n} + \vec{k} E_z \vec{E} \cdot \vec{n}] dS - \varepsilon \int_V [\vec{i} (\vec{E} \cdot \nabla E_x) + \vec{j} (\vec{E} \cdot \nabla E_y) + \vec{k} (\vec{E} \cdot \nabla E_z)] dV \right) \quad (3.26) \end{aligned}$$

$$\vec{F} = \varepsilon \left[\oiint_S \vec{E} (\vec{E} \cdot \vec{n}) dS - \int_V (\vec{E} \cdot \nabla) \vec{E} dV \right] \quad (3.27)$$

The first term of the last equation eq.3.27 is easy to understand. The second term is less easy: we need the use of two Vector formula:

$$(A \cdot \nabla) C = A_x \frac{\partial C}{\partial x} + A_y \frac{\partial C}{\partial y} + A_z \frac{\partial C}{\partial z} \quad (3.28)$$

and

$$\nabla(\vec{A} \cdot \vec{C}) = (\vec{A} \cdot \nabla) \vec{C} + (\vec{C} \cdot \nabla) \vec{A} + \vec{A} \times (\nabla \times \vec{C}) + \vec{C} \times (\nabla \times \vec{A}) \quad (3.29)$$

to express

$$\nabla(\vec{E} \cdot \vec{E}) = 2(\vec{E} \cdot \nabla)\vec{E} + 2\vec{E} \times (\nabla \times \vec{E}) \quad (3.30)$$

Knowing that for electrostatics case, $\nabla \times \vec{E} = -\frac{\partial B}{\partial t} = 0$ leads to:

$$\nabla(\vec{E} \cdot \vec{E}) = 2(\vec{E} \cdot \nabla)\vec{E} \quad (3.31)$$

By replacing in the last expression for \vec{F} eq. 3.27

$$\frac{1}{2}\nabla(\vec{E} \cdot \vec{E}) = (\vec{E} \cdot \nabla)\vec{E}.$$

we obtain:

$$\vec{F} = \varepsilon_0 \left[\oiint_S \vec{E}(\vec{E} \cdot \vec{n}) dS - \frac{1}{2} \int_V \nabla(E^2) dV \right] \quad (3.32)$$

By using one time again the Ostrogradsky theorem to express the second integral of eq.3.32, we get:

$$\vec{F} = \varepsilon_0 \oiint_S [\vec{E}(\vec{E} \cdot \vec{n}) - \frac{1}{2}E^2 \cdot \vec{n}] dS \quad (3.33)$$

If we write separately the three components of this vector equation, we see that it can be written in the form:

$$\vec{F} = \oiint_S \overset{\leftrightarrow}{T}_E \cdot \vec{n} dS \quad (3.34)$$

Where the newly introduced quantity $\overset{\leftrightarrow}{T}_E$ is the Electrostatic stress tensor Maxwell.

$$\overleftrightarrow{T}_E = \varepsilon_0 \begin{bmatrix} E_x^2 - \frac{E^2}{2} & E_x E_y & E_x E_z \\ E_x E_y & E_y^2 - \frac{E^2}{2} & E_y E_z \\ E_x E_z & E_y E_z & E_z^2 - \frac{E^2}{2} \end{bmatrix} \quad (3.35)$$

The last formula shows that the force exerted on all the charges contained in a volume V is equal to the integral on the surface S which encloses the volume V of the product of the electrostatic stress tensor with the unit vector normal to the surface. Similarly, for the magnetostatics case, the Maxwell stress tensor can be derived from its general form and leads to:

$$\overleftrightarrow{T}_M = \mu_0 \begin{bmatrix} H_x^2 - \frac{H^2}{2} & H_x H_y & H_x H_z \\ H_x H_y & H_y^2 - \frac{H^2}{2} & H_y H_z \\ H_x H_z & H_y H_z & H_z^2 - \frac{H^2}{2} \end{bmatrix} \quad (3.36)$$

Let us notice that, in presence of charges and currents both electrical and magnetic forces exist and the total force will be determined by the Maxwell stress tensor $\overleftrightarrow{T} = \overleftrightarrow{T}_E + \overleftrightarrow{T}_M$. Equation 3.19 is similar to the sum of the electric and magnetic stress tensors in equations 3.35 and 3.36. This suggests that the total force on an isotropic, linear dielectric object, as for incompressible fluid, can be found by applying equation 3.19 that requires the only knowledge of the permeability, permittivity and field values on a enclosed surface surrounding the object.

Let us now recover the well-known relationship of the Coulomb force (giving the force between two charges) from the Maxwell stress tensor. For this purpose, we consider a positive charge on the left at a distance $2d$ from the negative charge (see figure 3.11). We enclose one charge (the negative charge for instance) by an hemispherical surface whose plane side lies along the middle plane between the two charges. If we let the radius of the

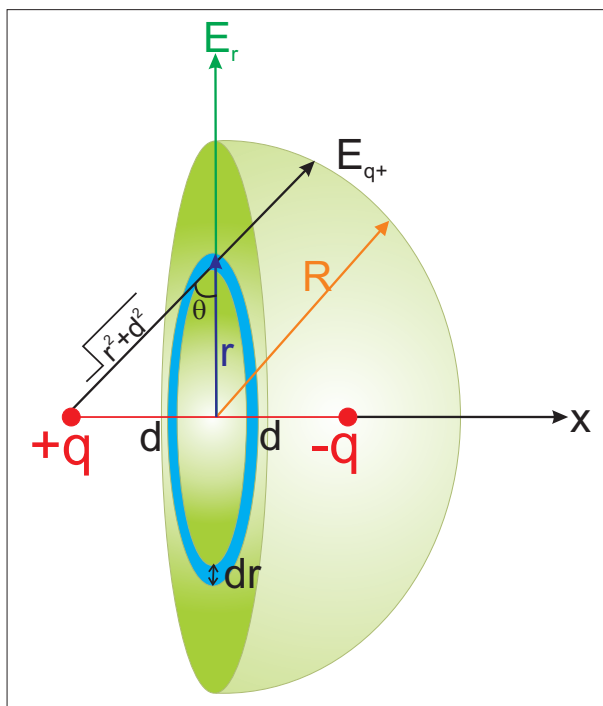


Figure 3.11: Hemisphere enclosing one of the two charge to find the force on charge enclosed.

hemisphere grow, the field at hemispherical boundary becomes that of a dipole, αR^{-3} . The surface integral then varies as R^{-4} . Taking the hemisphere to ∞ makes this part of the surface integral vanish. At the middle plane:

$$E_{q^+} = \frac{2q}{4\pi\epsilon_0(r^2 + d^2)} \cos\theta \quad (3.37)$$

$$E_{q^+} = \frac{2q}{4\pi\epsilon_0(r^2 + d^2)} \frac{d}{\sqrt{r^2 + d^2}} \quad (3.38)$$

$$E_{q^+} = \frac{2qd}{4\pi\epsilon_0\sqrt{r^2 + d^2}^3} \quad (3.39)$$

Thus

$$E_{q^+}^2 = \left(\frac{2qd}{4\pi\epsilon_0} \right)^2 \frac{1}{(r^2 + d^2)^3} \quad (3.40)$$

Where the transverse component of the fields of the two charges just neglected. The ninth element T_{33} of stress tensor is $\epsilon_0(E_x^2 - \frac{1}{2}E^2)$, and the surface element is $dS_x = -2\pi r dr$. The force on the charge from the stress tensor at the middle plane is then:

$$F_x = - \int_0^\infty -\frac{1}{2}\epsilon_0 E^2 (-2\pi r dr) \quad (3.41)$$

$$F_x = -\frac{1}{2}\epsilon_0 \frac{4q^2 d^2}{(4\pi\epsilon_0)^2} \int_0^\infty \frac{(2\pi r dr)}{(r^2 + d^2)^3} \quad (3.42)$$

$$F_x = -\frac{q^2 d^2}{4\pi\epsilon_0} \int_d^\infty \frac{dS}{S^5} \quad (3.43)$$

$$F_x = -\frac{q^2}{4\pi\epsilon_0 2(d)^2} \quad (3.44)$$

Where we have defined $S^2 = r^2 + d^2$ to perform the integration. The result obtained is of course exactly the result given by Coulomb's law.

In the general case of a any geometrical shape particle immersed in an electromagnetic field, the calculation of the force needs the determination of the field in the presence of the particle. This is a very hard task that we will address numerically through an adapted tool based on Finite Difference Time Domain (FDTD) method for the solving of Maxwell equations. Consequently, the next section is devoted to the presentation of the FDTD principle.

3.5 Numerical simulation tool (FDTD)

3.5.1 Principle of FDTD

The FDTD (Finite Difference Time Domain) method is a numerical approach that allows discretization of Maxwell's equations in space and time. We have selected simulation in time domain, according to the finite difference method, because it has the advantage of allowing a characterization in a broad frequency band for a structure through a single simulation. By applying a Fourier transform over the recorded time signals, it is possible to determine the optical response of the structure.

The application of the FDTD method to solve Maxwell's equations in free space was first introduced by Yee in 1966 [34]. The method consists in approximating the partial spatial and temporal derivatives appearing in Maxwell's equations by centered finite differences. Yee proposed scheme that allowed to overcome the difficulties due to simultaneous coupling between electric E and magnetic H fields. Indeed, an explicit numerical scheme is obtained for the calculation of the electromagnetic field throughout the studied volume versus time. The components of electric and magnetic fields are interleaved both in time and space. They are never calculated at the same location nor at the same time. By choosing a broad frequency band excitation, one may obtain electromagnetic characterization of the studied structure by Fourier transform of the time signal (near or far fields, transmission, reflection, ...).

Later, in 1975, Allen Taflove, who attempts to solve the problem of penetration of the microwaves inside human eye (many cataracts were observed on radar technicians during the second World War), decides to use the Yee algorithm. From the end of the 80s, the computer revolution has widespread the use of the FDTD method. This success

is explained mainly by the simplicity of its numerical implementation.

3.5.2 3D Illustration of FDTD

The starting point of the finite difference method is the differential form of Maxwell's equations given by:

$$\vec{\nabla} \times \vec{H} = \frac{\partial \varepsilon \vec{E}}{\partial t} \quad (3.45)$$

$$\vec{\nabla} \cdot \vec{E} = -\mu \frac{\partial \vec{H}}{\partial t} \quad (3.46)$$

Let us mention that the resolution of these two equations can be performed in different coordinates systems (cylindrical, spherical,...) depending on the symmetry of the solutions. In our case where no particular symmetry is involved, we consider solutions in Cartesian coordinates. In addition, we consider that involved materials in our case are linear and isotropic. Nonetheless, the case of dispersive materials, such as noble metals in the visible spectral range, will be addressed differently. We will limit our investigations to the case of LI materials that can be dispersive or not. Let us first consider the simplest case of LIND material. In this case, Maxwell-Ampere equation can be written:

$$\frac{\partial E_x}{\partial t} = \frac{1}{\varepsilon(x, y, z)} \left(\frac{\partial H_z}{\partial y} - \frac{\partial H_y}{\partial z} \right) \quad (3.47)$$

$$\frac{\partial E_y}{\partial t} = \frac{1}{\varepsilon(x, y, z)} \left(\frac{\partial H_x}{\partial z} - \frac{\partial H_z}{\partial x} \right) \quad (3.48)$$

$$\frac{\partial E_z}{\partial t} = \frac{1}{\varepsilon(x, y, z)} \left(\frac{\partial H_y}{\partial x} - \frac{\partial H_x}{\partial y} \right) \quad (3.49)$$

and :

$$\frac{\partial H_x}{\partial t} = -\frac{1}{\mu} \left(\frac{\partial E_z}{\partial y} - \frac{\partial E_y}{\partial z} \right) \quad (3.50)$$

$$\frac{\partial H_y}{\partial t} = -\frac{1}{\mu} \left(\frac{\partial E_x}{\partial z} - \frac{\partial E_z}{\partial x} \right) \quad (3.51)$$

$$\frac{\partial H_z}{\partial t} = -\frac{1}{\mu} \left(\frac{\partial E_y}{\partial x} - \frac{\partial E_x}{\partial y} \right) \quad (3.52)$$

To numerically implement these equations, temporal and spatial derivatives must be expressed as centered finite differences through the Taylor expansion. In addition, Yee demonstrated that numerical stable schema needs to evaluate the 6 components of the electromagnetic field for different positions (spatially) and at different times (temporally). Yee proposed his well-known discretization schema presented on figure 3.12 where the three components of the magnetic field are located at the centers of each unit cell faces while the electric ones are placed at the middle of the edges. The unit cell is then a parallelepiped with Δx , Δy and Δz side lengths.

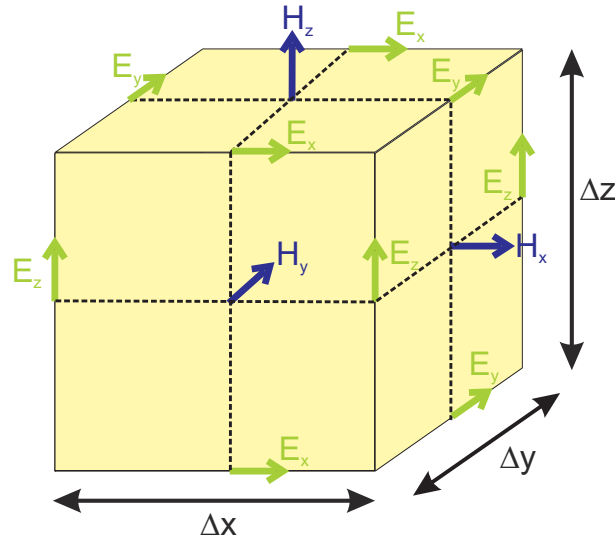


Figure 3.12: 3D Yee discretization schema (unit cell in Cartesian coordinates).

According to the Yee schema and assuming that fields are temporally interleaved,

equations 3.46 becomes:

$$\begin{aligned} \frac{\partial E_x}{\partial t} &= \frac{E_x(t + \frac{\Delta t}{2}) - E_x(t - \frac{\Delta t}{2})}{\Delta t} = \\ &= \frac{1}{\varepsilon(x, y, z)} \left(\frac{H_z(y + \frac{\Delta y}{2}) - H_z(y - \frac{\Delta y}{2})}{\Delta y} - \frac{H_y(z + \frac{\Delta z}{2}) - H_y(z - \frac{\Delta z}{2})}{\Delta z} \right) \end{aligned} \quad (3.53)$$

$$\begin{aligned} \frac{\partial E_y}{\partial t} &= \frac{E_y(t + \frac{\Delta t}{2}) - E_y(t - \frac{\Delta t}{2})}{\Delta t} = \\ &= \frac{1}{\varepsilon(x, y, z)} \left(\frac{H_x(z + \frac{\Delta z}{2}) - H_x(z - \frac{\Delta z}{2})}{\Delta z} - \frac{H_z(x + \frac{\Delta x}{2}) - H_z(x - \frac{\Delta x}{2})}{\Delta x} \right) \end{aligned} \quad (3.54)$$

$$\begin{aligned} \frac{\partial E_z}{\partial t} &= \frac{E_z(t + \frac{\Delta t}{2}) - E_z(t - \frac{\Delta t}{2})}{\Delta t} = \\ &= \frac{1}{\varepsilon(x, y, z)} \left(\frac{H_y(x + \frac{\Delta x}{2}) - H_y(x - \frac{\Delta x}{2})}{\Delta x} - \frac{H_x(y + \frac{\Delta y}{2}) - H_x(z - \frac{\Delta y}{2})}{\Delta y} \right) \end{aligned} \quad (3.55)$$

$$\begin{aligned} \frac{\partial H_x}{\partial t} &= \frac{H_x(t) - H_x(t - \Delta t)}{\Delta t} = \\ &= \frac{1}{\mu} \left(\frac{E_z(y + \frac{\Delta y}{2}) - E_z(y - \frac{\Delta y}{2})}{\Delta y} - \frac{E_y(z + \frac{\Delta z}{2}) - E_y(z - \frac{\Delta z}{2})}{\Delta z} \right) \end{aligned} \quad (3.56)$$

$$\frac{\partial H_y}{\partial t} = \frac{H_y(t) - H_y(t - \Delta t)}{\Delta t} = -\frac{1}{\mu} \left(\frac{E_x(z + \frac{\Delta z}{2}) - E_x(z - \frac{\Delta z}{2})}{\Delta z} - \frac{E_z(x + \frac{\Delta x}{2}) - E_z(x - \frac{\Delta x}{2})}{\Delta x} \right) \quad (3.57)$$

$$\frac{\partial H_z}{\partial t} = \frac{H_z(t) - H_z(t - \Delta t)}{\Delta t} = -\frac{1}{\mu} \left(\frac{E_y(x + \frac{\Delta x}{2}) - E_y(x - \frac{\Delta x}{2})}{\Delta x} - \frac{E_x(y + \frac{\Delta y}{2}) - E_x(y - \frac{\Delta y}{2})}{\Delta y} \right) \quad (3.58)$$

Δt is then the time delay between the upgrading of the electromagnetic field for each Yee cell. As mentioned before, the magnetic field components are calculated at times multiple of Δt while the electric field is calculated at half time between two magnetic ones. In order to illustrate the algorithm of the FDTD, we consider the case of a TM (Transverse Magnetic) field that illuminates a 2D sample (invariant along the z-direction see figure 3.13). In this case, the electric field has only two components (E_x and E_y and the magnetic field is scalar and has only y - component). Consequently, equations 3.53 to 3.58 become:

$$\frac{H_{z,(i,j)}^{n+1} - H_{z,(i,j)}^n}{\Delta t} = -\frac{1}{\mu} \left[\left(\frac{E_{y,(i+\frac{1}{2},j)}^{(n+\frac{1}{2})} - E_{y,(i-\frac{1}{2},j)}^{(n+\frac{1}{2})}}{\Delta x} \right) - \left(\frac{E_{x,(i,j+\frac{1}{2})}^{(n+\frac{1}{2})} - E_{x,(i,j-\frac{1}{2})}^{(n+\frac{1}{2})}}{\Delta y} \right) \right] \quad (3.59)$$

$$\frac{E_{x,(i,j+\frac{1}{2})}^{n+\frac{1}{2}} - E_{x,(i,j+\frac{1}{2})}^{n-\frac{1}{2}}}{\Delta t} = \frac{1}{\varepsilon} \left(\frac{H_{z,(i,j+1)}^n - H_{z,(i,j)}^n}{\Delta y} \right) \quad (3.60)$$

$$\frac{E_{y,(i+\frac{1}{2},j)}^{n+\frac{1}{2}} - E_{y,(i+\frac{1}{2},j)}^{n-\frac{1}{2}}}{\Delta t} = -\frac{1}{\varepsilon} \left(\frac{H_{z,(i+1,j)}^n - H_{z,(i,j)}^n}{\Delta x} \right) \quad (3.61)$$

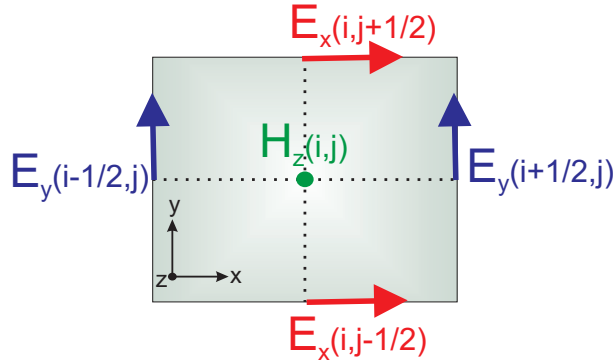


Figure 3.13: Circulation of \vec{E} around \vec{H}

In this peculiar case, the Yee schema is reduced to a planar one (rectangular shape) where the magnetic field occupies its center and the two electric components are placed at the middle of the sides (E_x along the x -parallel side and E_y along the y -parallel one) as shown on figure 3.13.

The temporal schema is similar to the spatial one except that all the electric field component are calculated for the same moment $(n + \frac{1}{2})\Delta t$ being the time step) while the magnetic components are calculated at moments $n\Delta t$ (Δt , half a time step after the electric ones. This arrangement ensures an iterative process that is entirely explicit as shown in the following schema (3.14):

Thus, the data of the electric field at any spatial location are calculated at a given

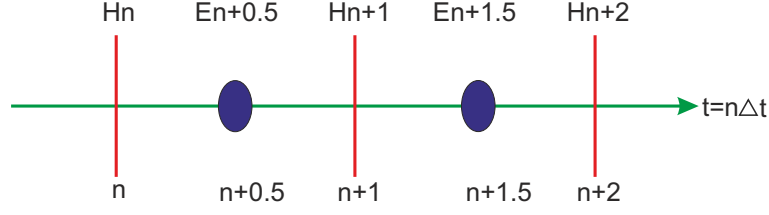


Figure 3.14: Calculating \vec{H} at time $n\Delta t$ and \vec{E} at time $(n+0.5)\Delta t$, where n is an integer.

time from the surrounding magnetic field components previously calculated and stored. Then the magnetic field is calculated at the next time through the values of electric field that has just recorded, and, even up to a specified value of temporal steps insuring a complete light-matter interaction (permanent regime).

3.5.3 Stability criteria

Numerical FDTD algorithm stability problems have been studied by Courant Friedrich and Lewy (CFL) [76] and Von Neumann, from a rigorous mathematical approach. This study shows that the explicit diagram based upon the Yee's scheme is stable under a temporal criterion called the CFL condition that is given by [77]:

$$\Delta t \leq c \left[\sqrt{\frac{1}{\Delta x^2} + \frac{1}{\Delta y^2} + \frac{1}{\Delta z^2}} \right]^{-1} = \frac{1}{c\sqrt{\frac{3}{\Delta^2}}} = \frac{\Delta}{c\sqrt{3}} \quad (3.62)$$

Where Δt is time delay, c is speed of light, $\Delta x = \Delta y = \Delta z$ are spatial step. Due to the fact that most of the modeled structures involve large window calculation volume, a non-uniform meshing will be used meaning that $\Delta x, \Delta y$ and Δz are now function of x, y and z respectively. Even if the CFL condition expression changes in this case, we choose to use the same definition of Δt giving in Eq. 3.62 after replacing Δ by δ which is the smallest value of the spatial step ($\delta = \text{Min}(\Delta x(i), \Delta y(j), \Delta z(k))$).

In addition of the instability problem, the discretization of the Maxwell equations can generate numerical dispersion problems (due to the errors induced by the deformation of the signal phase). To overcome this problem, Taflove et al.[77] studied the numerical stability using a complex-frequency analysis and found a criterion that bounds the spatial step as following:

$$\text{Max}(\Delta x, \Delta y, \Delta z) \leq \frac{\lambda_{min}}{n} \quad (3.63)$$

where λ_{min} is the minimum wavelength of the spectral range over which we wish to make our study and n is the number of cell per wavelength. The more the n value is big, the more the numerical error is small. In our case where a non uniform meshing is applied, the value of n was set between 70 and 215 while a value of 16 or 20 is large enough to insure a phase error of 10^{-2} [77]. In fact, in nanooptics, small values of n are currently used to accurately describe the structure geometry under consideration (small details such as the metal thickness, the 25 nm gap size of a nano-antenna,...).

Nonetheless, we must keep in mind that these two criteria given by Eq. 3.62 and 3.63 must always checked whatever the geometry and dielectric constant of the considered structures.

3.5.4 Dispersion

For a faithful modeling of light-matter interaction phenomena, it is essential to take account of actual *EM* properties of the materials. In our case, all dielectric media are supposed to be non dispersive while this assumption becomes no more valid in the case of noble metals in the visible and IR spectral ranges. Even if metals are non magnetic in this domain, their dielectric permittivity greatly depends on the frequency. The charge densities and currents (electric conduction) do not appear explicitly in the calculation

because they are integrated in the expression of the dielectric constant. Direct calculation of the electric and magnetic fields components is then not obvious through the FDTD algorithm due to the need of the calculation of a convolution integral for the determination of the electric displacement vector given by :

$$\vec{D}(t) = \varepsilon(t) \otimes \vec{E}(t) \quad (3.64)$$

$$\vec{D}(t) = \int_{-\infty}^t \varepsilon(\hat{t}) \cdot \vec{E}(t - \hat{t}) d\hat{t} \quad (3.65)$$

The fastidious calculation of this integral can be bypassed in the case where the permittivity can be analytically expressed as a function of the frequency. One of the simplest expression is the Drude model that is described below.

3.5.4.1 Drude model

The Drude model was developed at the beginning of the 20th century by Paul Drude. It came a three years after J.J. Thompson who discovered the electron in 1897. Drude model is based on the kinetic theory of electrons in a metal. This particularly simple theory successfully represents the optical and thermal properties of some metals. In this model, the metal is considered as positive ions immersed in a free electron gas [78].

The frequency dependence of the medium permittivity can be derived from the equations of motion. In the absence of relativistic effects (such as the Lorentz force) and in the presence of external electric field, The equation of the motion of an electron can be described as follows:

$$\ddot{X}(t) + \gamma \dot{X}(t) = -\frac{e}{m} E(t) \quad (3.66)$$

m represents the mass of the electron, e its charge and γ a damping term equal to the inverse of mean free path ($\gamma = \frac{1}{\tau}$). The expression $\gamma \dot{X}$ indicates the presence a damping force that can be attributed to different collisions. One notice that the model takes into account only the contribution of the electrons of the conduction band and it is adapted to alkali and noble metals.

Knowing that the model takes into account only the contribution of conduction electrons. After solving the equation 3.66, the expression of the dielectric permittivity can be written as:

$$\varepsilon_D = \varepsilon_\infty - \frac{\omega_D^2}{\omega^2 + i\gamma_D\omega} \quad (3.67)$$

Where ω_D is plasma frequency of electrons have mass m and charge e defined by $\omega_p = \frac{Ne^2}{m\varepsilon_0}$. ε_∞ represents the relative permittivity of the metal at infinite frequencies generally taken equal to 1. In our study, these parameters must be changed in FDTD code according to the operation wavelength. Experimental data taken from Palik [79] are used to adapt the Drude model (ω_D and γ_D values) in our FDTD calculations.

3.5.5 Boundary conditions: PML principle

To prevent reflections caused by the scattering of waves from the domain boundaries, a lot of methods were considered [80, 81, 82, 83, 84, 85, 86, 87] but they are still not very accurate. The perfectly matched layers (PMLs) was originally formulated in 1994 by Berenger [88] and it is now commonly used to truncate computational regions in numerical methods to simulate problems with open boundaries especially in the FDTD method. The PMLs technique based on the principle of impedance adaptation at the interface between

two media that have the same index but one of these media is absorbent with electric and magnetic conductivities. This adaptation condition can be written as:

$$\frac{\sigma}{\epsilon} = \frac{\sigma^*}{\mu} \quad (3.68)$$

Where σ, σ^* are electric and magnetic conductivity respectively. The PMLs have the property that the EM waves are gradually absorbed in the layers before they reach the outer boundaries. In this way, there will be no reflections that can disturb the propagation of the source wave in the calculation window. The PML absorption must then be anisotropic in the sense that it will be non-zero for waves propagating along the perpendicular direction to the interface between PMLs and the main window (x axis in figure 3.15) while no absorption is needed along the interface direction (y axis in figure 3.15). In the PML medium, the wave is split into two unphysical waves: 1) a wave propagating at normal incidence and satisfies the equation eq 3.68. This wave is attenuated and absorbed by the PML medium and undergoes only a very low reflection. 2) A second wave at grazing incidence that propagates without absorption in the PML medium. This wave does not suffer any reflection and PML must exhibit identical properties to that of the main window. This anisotropy is then transposed to the absorption coefficients (σ and σ^*) by defining three different components for each one ($\sigma_x, \sigma_y, \sigma_z, \sigma_x^*, \sigma_y^*$ and σ_z^*). The non-zero components are not constant but their values gradually increase from 0 (absorption of the main medium) to a maximum value σ_{max} through polynomial law of p degrees:

$$\sigma_x(i) = \sigma_{max} \left(\frac{\delta_x}{L} \right)^p \quad (3.69)$$

where δ_x is the distance between the considered cell center and the PML-medium

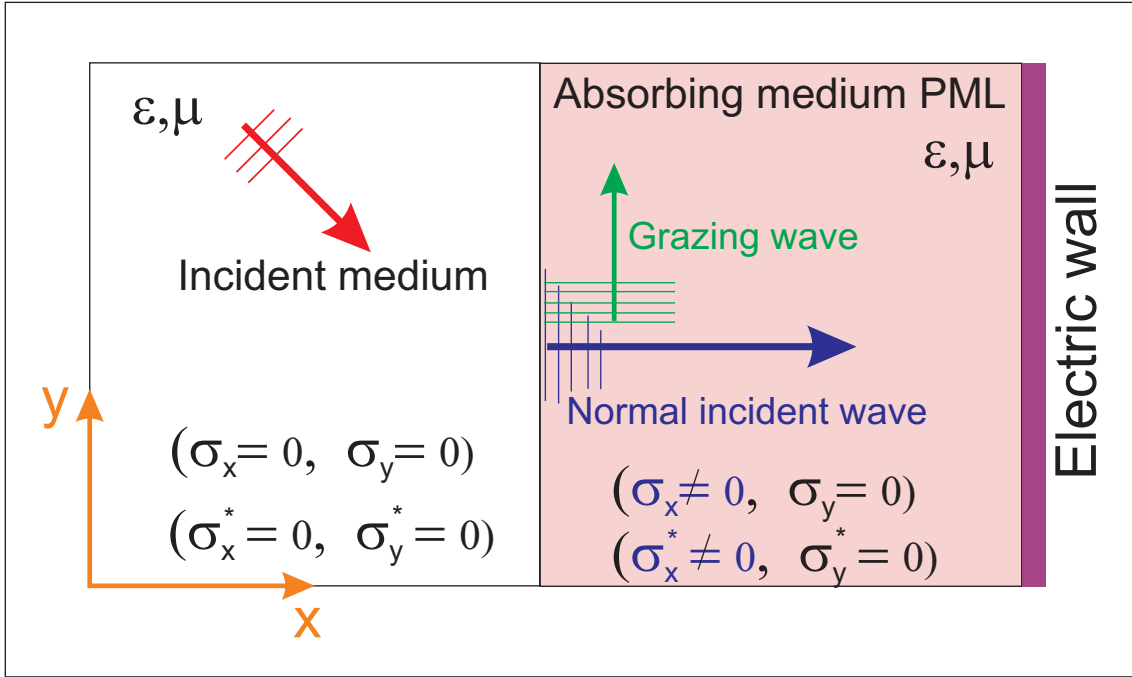


Figure 3.15: Principle of perfectly matched layers (PMLs) operating in medium.

interface and L is the PML thickness. We set the value of p to 2 and the σ_{max} value so that the maximum allowed reflection by the PMLs is fixed to 10^{-6} .

The thickness of the absorbent layer may be chosen as large as desired to minimize the reflections at the edge of the calculations window. For example, in our calculation, for $R_{max} = 10^{-6}$ and an operation wavelength equal to $\lambda = 1300$ nm a PMLs thickness equal to 150 nm is sufficient.

3.6 Validation of our code

3.6.1 Test: Optical force calculations of dielectric nanoparticle

As mentioned before, we used available home-made FDTD codes that we modified in order to integrate detectors which record the six electromagnetic field components over

the six faces of a cubic or, more generally, parallelepiped box surrounding the particle on which we are calculating the optical force. These field values are then processed through a Matlab code to numerically evaluate the Maxwell stress tensor. Optical forces are then determined by integrating the flux of the MST over these six faces. In fact, as we work in a harmonic regime, only time average value of the MST is involved in the force expression. FDTD codes working in complex notation are considered to compute the electromagnetic fields. In this case, numerical simulations require 2 times more CPU time and 2 times more memory than the calculation in real notation but have the advantage to directly give time average values.

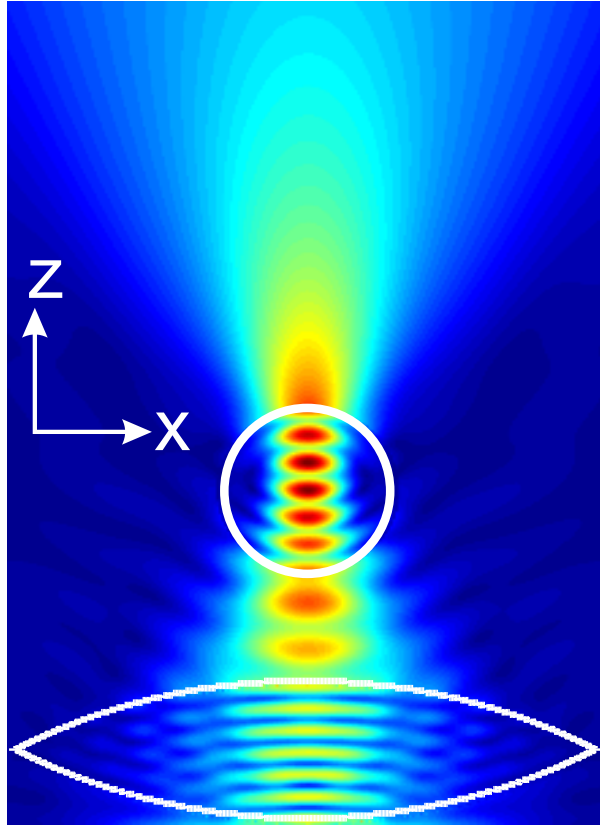


Figure 3.16: A microlens biconvex, curvature radius $r = 4\mu m$, thickness $t = 1\mu m$ and index $n_{lens} = 2$ is placed in front of a Gaussian beam to accentuate the focus on the Np.

The first example we studied is similar to the experiment that was conducted by Ashkin to prove the possible trapping of particles by optical beams. For this purpose, we consider a dielectric spherical Np of radius $R = 600nm$, with refractive index $n_s = 1.7$. The Np

is assumed to be surrounded by vacuum $n_{air} = 1$ and illuminated by a Gaussian beam of width $sw = 2000nm$. We placed a micro biconvex lens in front of the Gaussian beam with radius of curvature $r = 4\mu m$ and thickness $t = 1\mu m$ and lens index $n_{lens} = 2$, to obtain higher focus on the Np. The wavelength is fixed to $\lambda = 632.8nm$. The main calculation window extends over 320 cells in the x and y - directions and over 384 cells in the z direction with uniform mesh ($\Delta x = \Delta y = 15nm$). The calculation window, in which the Np and the lens are located, is limited by the Berenger PML absorbing boundary conditions [88] to avoid parasitic reflections. The total dimensions of the computational window are $(4.8, 4.8, 5.76)\mu m$ in the x, y, z directions respectively. The scheme of the studied configuration is given in figure 3.16.

One FDTD simulation is performed per Np position. This later was displaced in a longitudinal plane (xOz) and 2838 sphere positions (33×86) were considered in this plane symmetrically arranged with respect to the lens axis. The three components of the optical force are then calculated where in figure 3.17 a we presented 3D view of F_x component for each position of the Np. As seen in figures 3.17 a,b the component F_x of force are perfectly antisymmetric while, from the figures 3.18 a and b, the component of F_z is symmetrical with respect to the x -position (F_y component in xOz plane is always equal to zero due to the structure symmetry). One emphasizes the fact that, for specific lens to Np distance (here $d=2513$ nm), F_z passes through a minimum negative value when the Np approaches the z -axis which corresponds to an attractive force. Thus, for this position, the Np is both attracted toward $x = 0$ and $z = d$. This corresponds to efficient trapping. Figure 3.19, explicitly shows this trapping through the drawing of the force calculated for each Np position. The trapping zone is pointed out with a black square where both F_x and F_z are minimum. Consequently, when the Np is placed at the vicinity of this zone, the optical force tends to move it (see white arrows on the same figure) toward this trapping position.

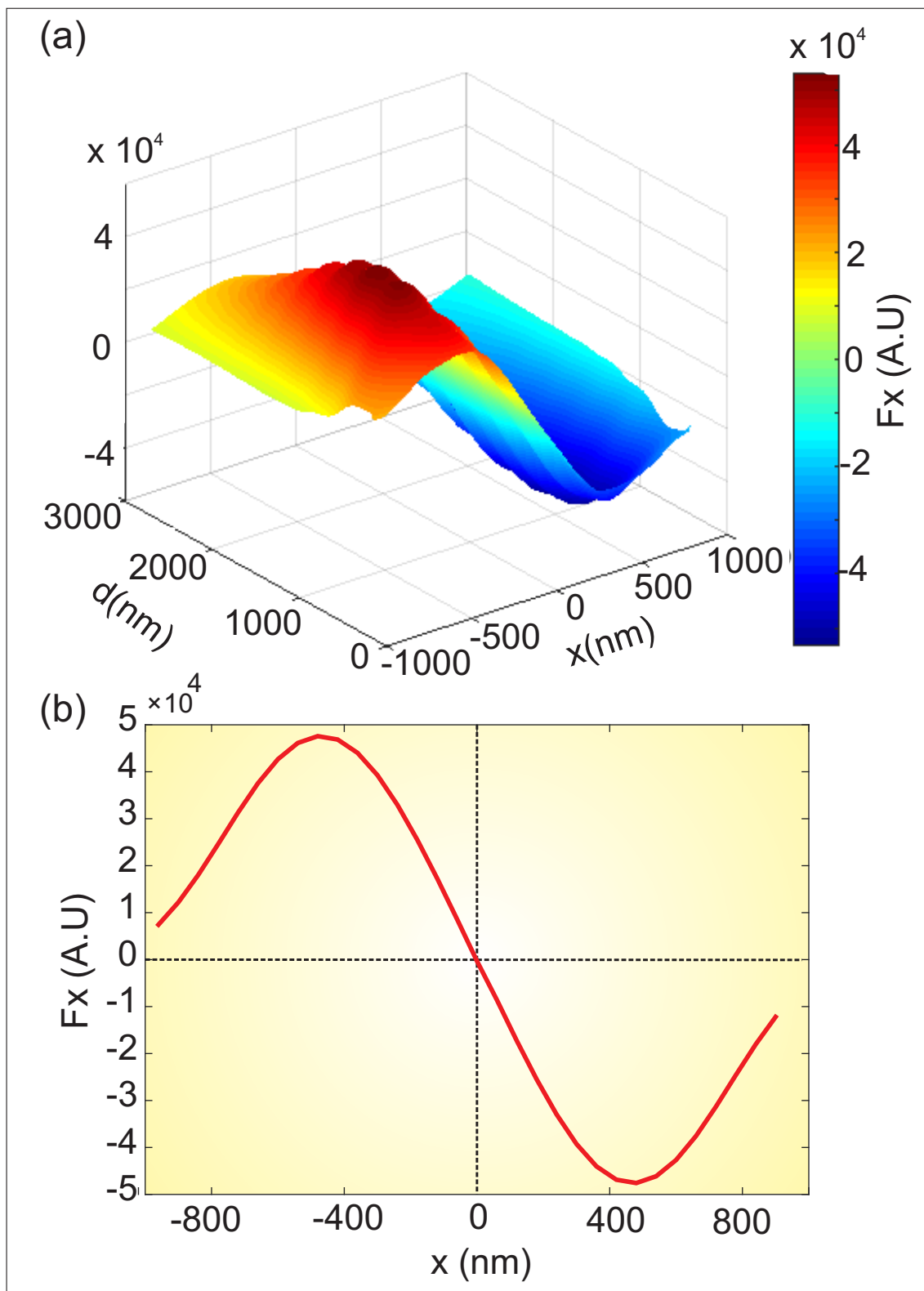


Figure 3.17: a) 3D map of the optical force F_x in the xOz plane in front of the lens. b) cross-section made over the figure (a), along the Ox -axis for $d = 2513$.

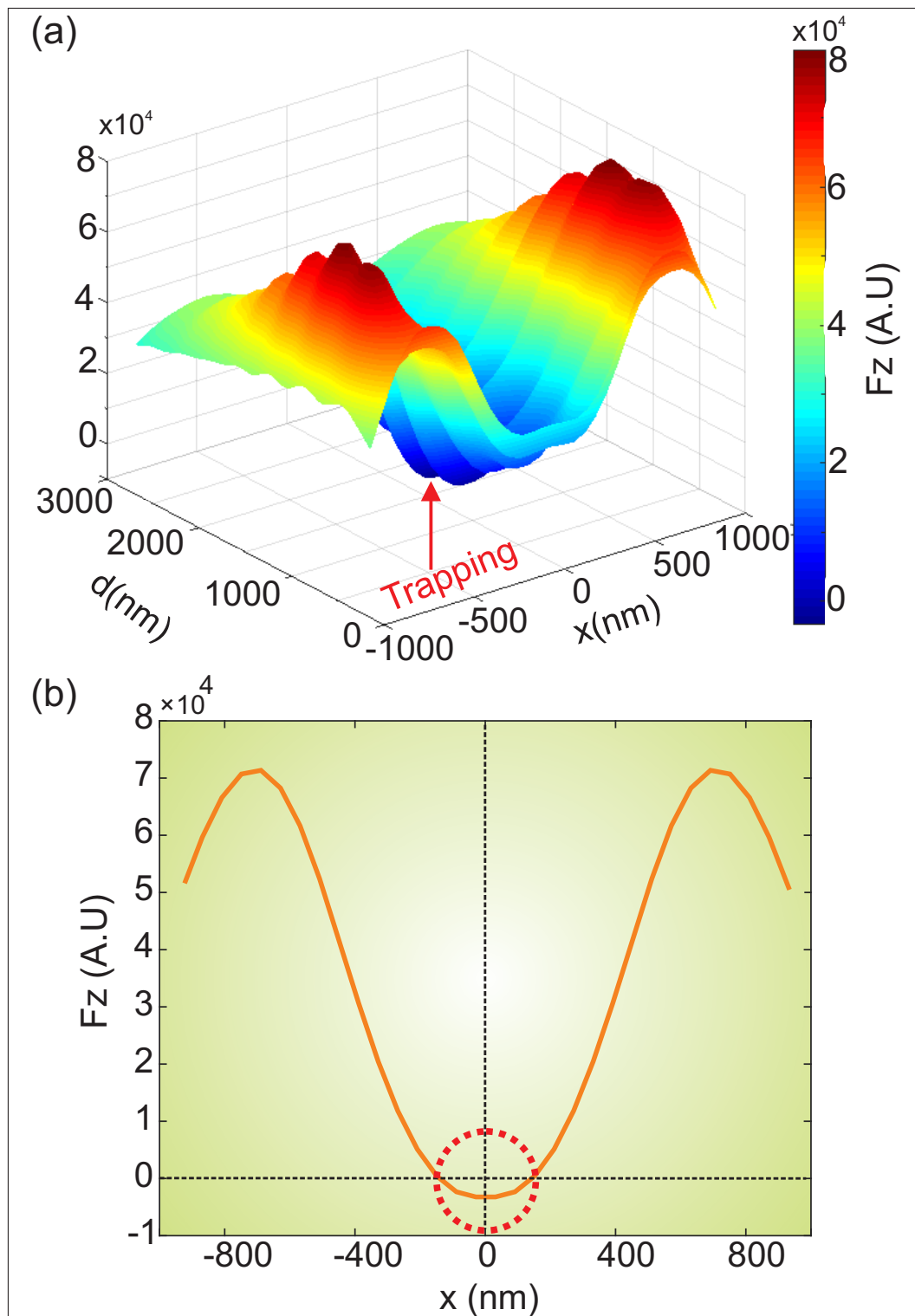


Figure 3.18: a) 3D map of the optical force F_z in the xOz plane in front of the lens. b) cross-section made over the figure (a), along the Ox -axis for $d=2513$.

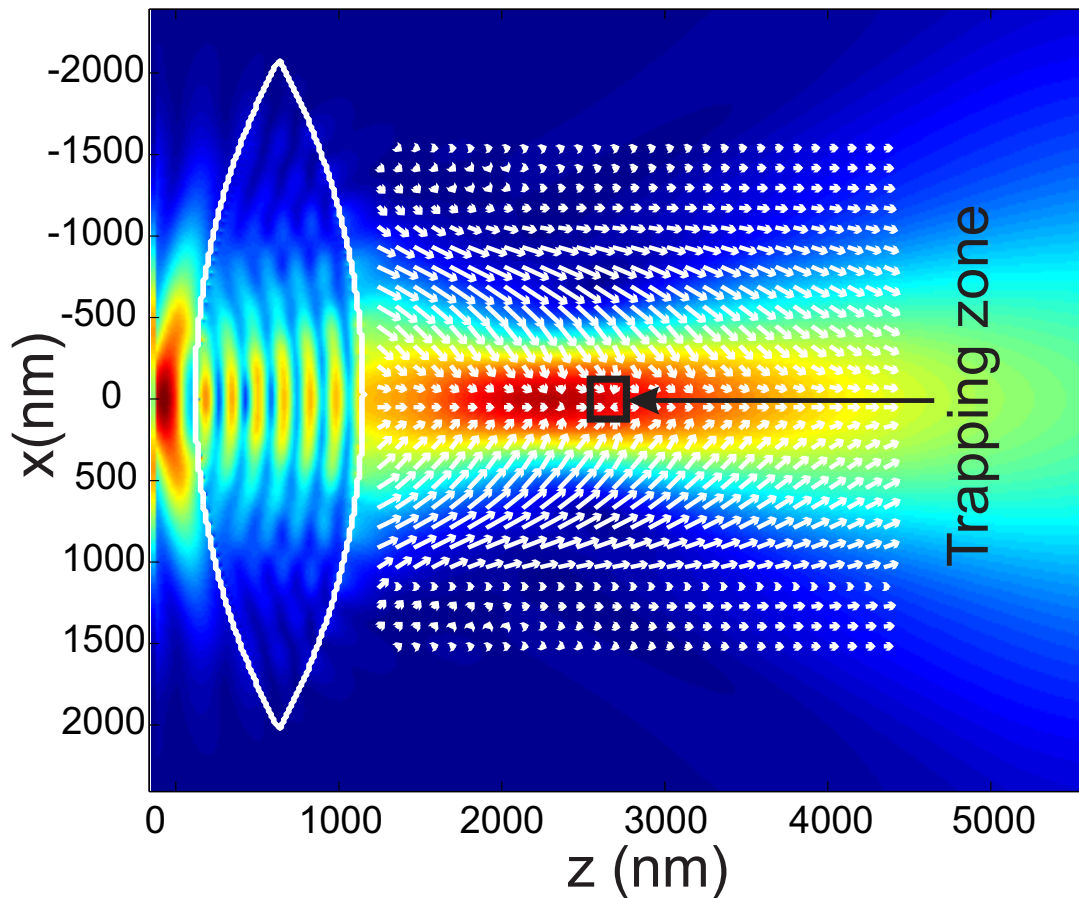


Figure 3.19: Map of the force amplitude (in color level) exerted by the focused light passing through the microlens. The white arrows give the force direction and amplitude. The black square shows the trapping zone.

3.6.1.1 Validation of the conservative character of the optical force

A force is qualified by "conservative" when the work of this force is independent from the path and is equal to zero when the path is a closed loop. It depends only on the initial and final positions. In other words, a N_p located at the same physical location in a closed loop must have the same kinetic energy at all times if it is within a conservative system. When applied to our case, this means that the force (the flux of the Maxwell stress tensor) is constant whatever is the closed surface that surrounds the N_p . This property was verified through the calculation of the force for different sizes of the box surrounding the spherical N_p as shown in the figure 3.20 a.

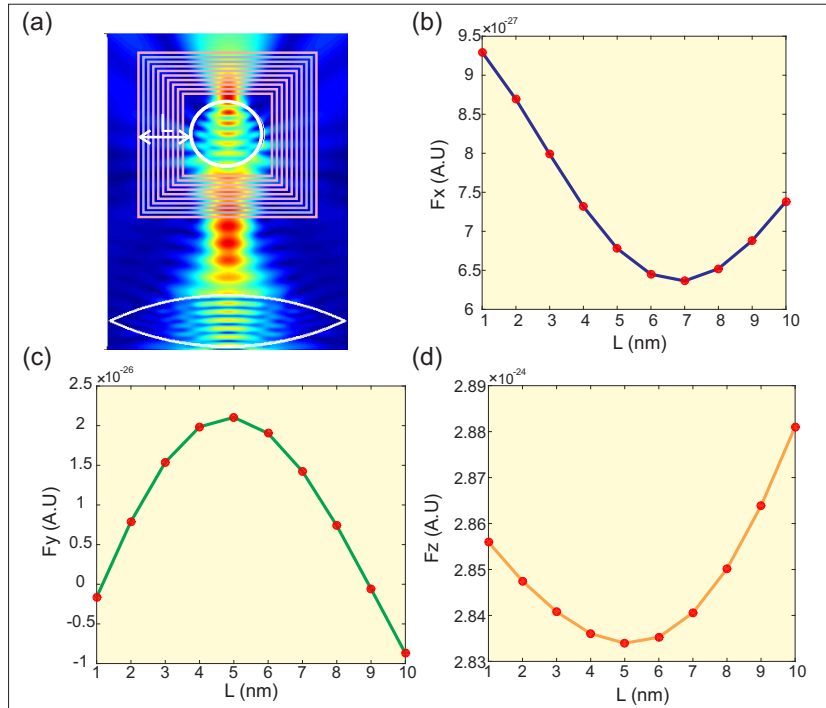


Figure 3.20: (a) Schema of a biconvex microlens with sphere surrounded by different boxes. (b),(c),(d) values variations of F_x , F_y , F_z respectively.

We calculated the force for each box dimension and we achieved a good results, that are presented on figure 3.20 b,c,d, where the three force components are plotted versus the box size. As shown, the variations of these component amplitudes are very small and a maximum deviation of $F_x = 0.39\%$ A.U, $F_y = 0.17\%$ A.U, $F_z = 0.0165\%$ A.U is obtained. This clearly demonstrates the conservative character of the optical force. This proves that our code is valid with logical results.

3.7 Conclusions

In this chapter, we described all concepts and theoretical fundamentals (basics of electromagnetic theory, numerical tools, Yee algorithm,...) to understand the method used to model light-matter interaction (FDTD algorithm) and to deduce the MST expression

that leads to the determination of optical forces. We also made tests and verified our code and all the numerical tools we used. These theoretical tools will be exploited in the next chapter to compare experimental results of optical trapping against simulations.

Chapter 4

Application 1: Optical tweezers based on fibred Bowtie Nanoaperture Antenna (BNA)

4.1 Introduction

This chapter deals with the $3D$ optical trapping of submicron particles. The originality of this work deals with the use of a fibred nanotweezers based on a Bowtie Nanoaperture Antenna (BNA). We show here optical trapping of nano-objects still observable with a conventional microscope without fluorescence imaging techniques (preliminary step before switching to smaller particles). This study represents, to our knowledge, the first demonstration of an all-fiber optical nano-tweezer (which is not limited by diffraction). Optically-induced heating of the tip is weak enough to not affect the particle motion within the close environment of the tip. This represents promising perspectives in the optical manipulation of physical and biological entities down to the nanoscale. The re-

cent achievement of optical trapping with plasmonic nano-antennas [89, 90] introduces the prospect of the manipulation of deeply sub-wavelength entities in a highly controlled and reproducible manner. However, the resulting optical architectures proposed so far are limited to nano-antennas fabricated on planar surfaces and optically excited with bulky optics (microscope objectives, polarizers, diaphragm, ...).

One notices that 3D optical trapping of polystyrene nanoparticle (diameter of 50 nm) was proposed very recently [7] using a quite similar configuration based on the combination of a BNA and a SNOM tip. No theoretical investigations on the optical forces were presented in that paper. Trapping was demonstrated through far-field measurements of the fluorescence emission modifications induced by the particle position as shown in figure 4.1.

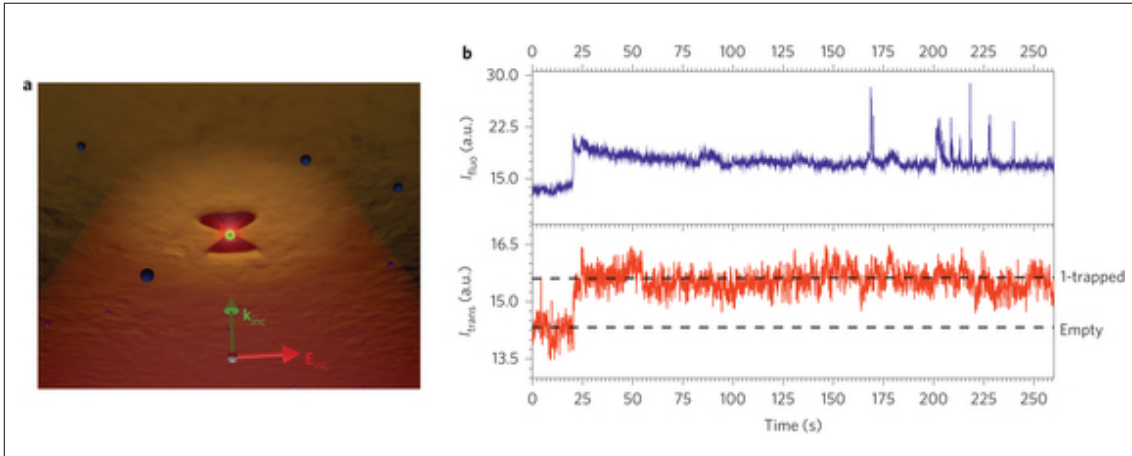


Figure 4.1: Schema of the experimental configuration of BNA tip. (b) Experimental time traces showing the transmission through the BNA at 1064 nm (red curved) and the fluorescence from the trapped bead (blue curve). The increase in both transmission and fluorescence corresponds to the trapping of a single 20 nm PS bead.[7]

Various optical tweezers involving fiber microtips [91, 63], and multicore lensed fibers [92] have been demonstrated for the 3D optical trapping of particles of a few micron size. The 3D optical trapping of sub-micron particles with a fiber system has recently been achieved with the development of fiber 3D bottle beams [93] and plasmonic lenses [94]

which are techniques based on diffraction limited focusing (Rayleigh criterion).

Our theoretical study is done in parallel with experimental study in our team by Thierry Grosjean and Ali El Eter. Let us see in the following section(4.2) the reasons of using BNA.

4.2 Bowtie Nanoaperture Antenna properties

The choice of the BNA is motivated by the fact that, at resonance, it exhibits high electromagnetic field confinement together with electric intensity enhancement in its gap zone. These two characteristics are necessary to expect optical force enhancement leading to a possible trapping of very small nanoparticles. When engraved at the apex of a metal coated tapered optical fiber, this BNA can be used both a nano-emitter [95] or a nano-collector [96]. Its polarization properties are of interest due to the fact that its resonance can only be induced with electric field directed along its axis (metallic arms direction). Consequently, this BNA on tip was proposed as an efficient near-field optical probe [51] that allows selective detection of the electric near-field components. As mentioned before, the Nano-Optics team of FEMTO-ST also proposed this BNAT as a nano-tweezers to trap microsized latex particles.

The resonance properties of BNA antennas were studied in [97] where a guided mode inside the BNA was demonstrated to be at the origin of this resonance that occurs at the cutoff wavelength of the fundamental guided mode. The latter is polarized along the metallic arms of the BNA and it can only be excited by an incident beam having the same polarization. Consequently, the BNA acts as a nanopolarizer with axis direction is parallel to the metallic arms.

4.3 Bowtie Nanoaperture Antenna design on fiber SNOM tip

In order to make faithful numerical simulations, we have considered the exact fabricated BNAT geometry to be introduced in our model. Experimentally, a polymer tip (30 micrometer long, radius of curvature of 0.5 micrometer at tip apex) was considered to receive the BNA at its apex. This kind of tip is now commercially manufactured by LOVALITE startup based in Besançon. The tip is first obtained by photopolymerization at the cleaved end facet of a monomode ($\lambda \simeq 1064$ nm wavelength) glass fiber[98]. The angle of the tip body is about 14° . Next, the probes are metal coated with a few nanometer thick titanium adhesion layer followed by a 150 nm thick aluminum layer to ensure robustness to optically-induced heating due to in-fiber illumination figure 4.2 a. Aluminum is chosen for its high conductivity at infrared frequencies leading to a strong antenna effect.

The metal layer thickness was measured to be 100 nm at the tip apex. Note that the uncertainty of the metal layer thickness has no incidence onto the BNA resonance properties [97]. To avoid surface roughness at the tip apex, the metal layer is abraded over a thickness of about 70 nm by beam (FIB) from the tip side and inspected by scanning electron microscopy (SEM). The FIB system used for this experiment is a dual beam FEI Helios 600i with a Raith Elphy Multibeam attachment. This procedure, tested on several tips, has a good reproducibility. These results in a flat homogeneous surface at the tip apex that is a few hundreds of nanometers wide figure 4.2 b. Finally, a 165 nm wide BNA with square gap of about 45 nm large and 45 flare angles is fabricated at the apex of the tip by FIB milling. Figures 4.2 c,d display scanning electron micrographs of the resulting fiber device.

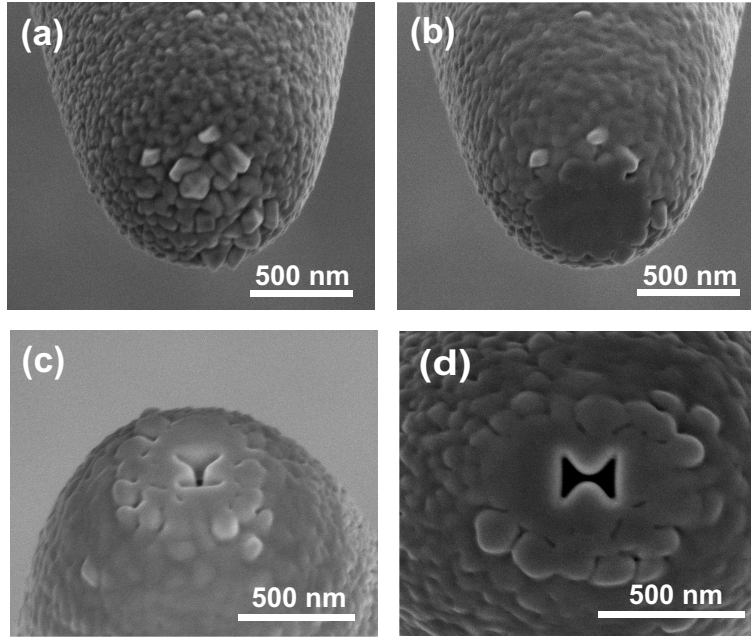


Figure 4.2: (a-d) SEM micrographs of the fiber-integrated nano-tweezer based on a BNA fabricated at the apex of a SNOM tip: side view of the fiber metal-coated SNOM tip (a) before and (b) after initial FIB processing to flatten the tip apex: the rough metallic surface of the rounded apex is milled from the side to be finely polished. (c) and (d) side and top views of the BNA at the tip apex, respectively (obtained by FIB milling from the top) [8].

The BNA is to be resonant at a wavelength of $\lambda \simeq 1064$ nm when it is immersed in water (refraction index n of 1.315). This wavelength is located in a transparency spectral window of water. In our theoretical study, the design process is performed using three-dimensional "Finite Difference Time Domain" method (3D FDTD) [69] and the permittivity of the metal (aluminum) is defined with a Drude model. Figure 4.3 b shows the resonance spectrum of the fiber-integrated BNA in water. The BNA is excited with an incoming gaussian beam inside the tip (fundamental guided mode of the fiber). We only modeled the last 2 micrometers of the tip body before the apex.

The input beam is polarized along the symmetry axis of the BNA that passes through each metal triangles tip (called polarization axis of the BNA), and described by a single temporal pulse. The time-varying optical fields are calculated at a single grid cell at

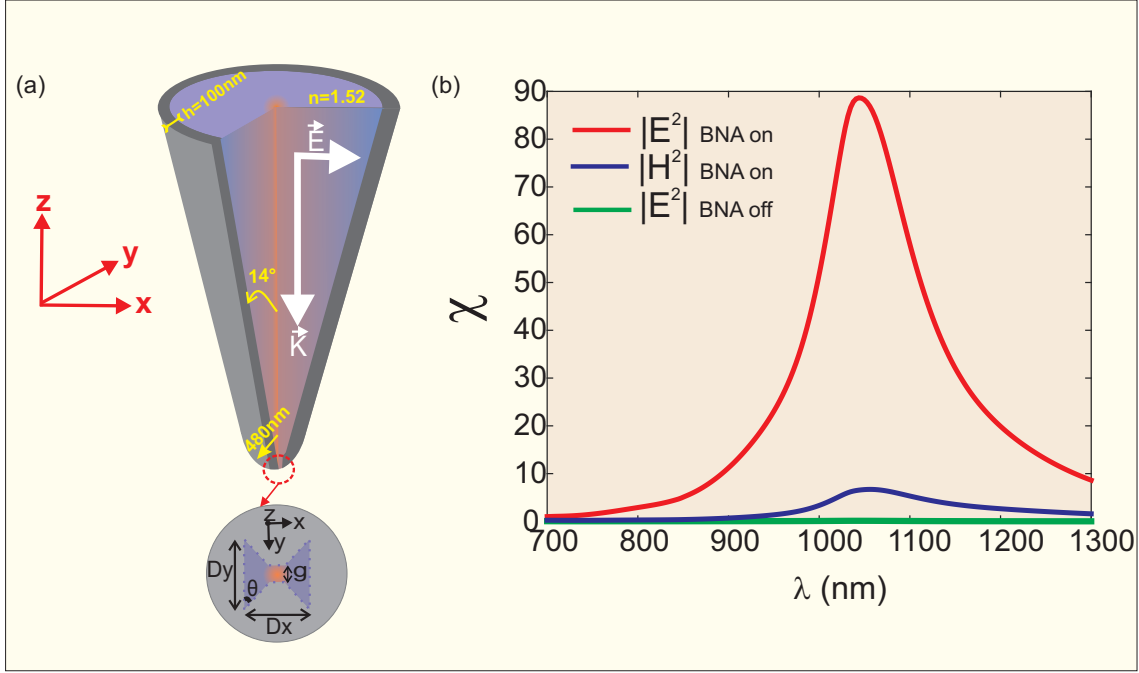


Figure 4.3: (a) Schema of the end part of a polymer tip with half angle cone of 14° and apex radius of 480 nm. The polymer has an optical refractive index $n = 1.52$ and the tip is supposed to be coated by a 100 nm -thick aluminum layer. The permittivity of the latter is defined with a Drude model where the plasma frequency is set to $w_p = 1.973 \times 10^{16}$ and the dumping term to $\Gamma = 2.198 \times 10^{14}$ rad/s. The geometrical parameters of the BNA are : $D_x = 135$ nm, $D_y = 165$ nm and the gap $g = 45$ nm. b) Calculated near-field (at 15 nm above the BNA) electric intensity enhancement of the BNAT shows a maximum of 90 at $\lambda \simeq 1064$ nm.

the middle of the BNA feed gap. The spectrum of the electric field is then calculated by Fourier-transforming this result ($I(\lambda)$) (where $I = |E|^2$) and normalizing it by the spectrum calculated with the same procedure without metal with only the polymer tip ($I_v(\lambda)$). This leads to the definition of the electric intensity enhancement factor χ_e as:

$$\chi_e = \frac{I}{I_v} \quad (4.1)$$

We see that the BNA induces at $\lambda \simeq 1064$ nm a maximum $\chi_e = 90$ enhancement of the optical electric intensity.

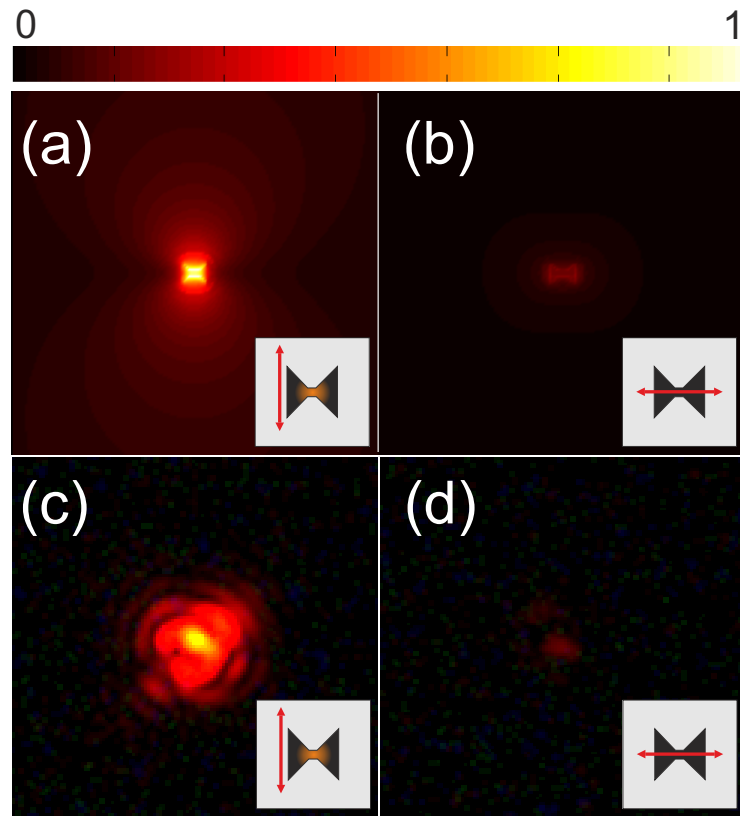


Figure 4.4: (a,b) Simulation of the distribution of optical electric field (amplitude) in a transverse plane (perpendicular to the tip axis) taken 15 nm away from the tip ($\lambda = 1064$ nm), for two perpendicular polarization directions of the incoming waves (see arrows in insets). (c,d) Far-field experimental images of the fiber tip output for two perpendicular polarization directions of the in-fiber illumination (BNA on and off resonance, see arrows in the insets)[8].

Figures 4.4 a and b show the simulation of the electric-field distribution (amplitude) produced by the BNA at $\lambda \simeq 1064$ nm for an incident polarization parallel (on-resonance) and perpendicular (off-resonance) to the polarization axis of the BNA, respectively. The fields are calculated at a transverse (XY)-plane (perpendicular to the tip symmetry axis (Oz)) 15 nm away from the tip apex. The electric field enhancement is induced at the BNAs feed gap by a resonant optical capacitive effect in-between the two closely spaced metal triangles of the BNA, which leads to a charge distribution in the gap zone corresponding to an oscillating electric dipole [96, 99].

The dipolar properties of the BNA, which are common to all gap-based nano-antennas, associate the generation of a tiny "hot spot" to a high polarization sensitivity of the nanostructure: the tight optical confinement is canceled and the intensity maximum over the antenna is greatly reduced when the BNA is excited with optical waves polarized perpendicularly to its polarization axis see figure 4.4 b. It achieved good agreement with experimental results as shown in figures 4.4 c,d [8]. Also, the spatial distributions of the electric intensity of the BNAT in longitudinal planes xOz and yOz are presented on figure 4.5. It confirms the strong confinement inside the BNA gap. Instead of plotting the electric intensity, we plot its fifth root in order to get clear insight on the confinement.

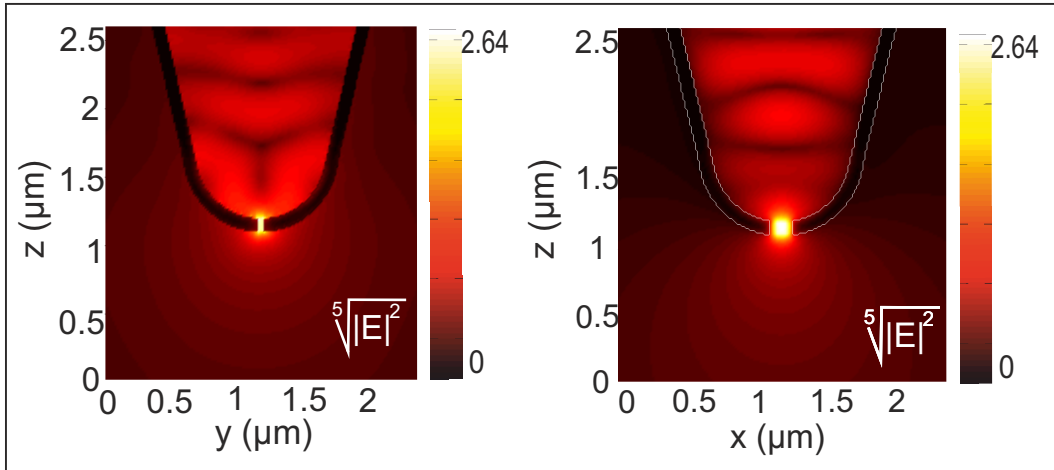


Figure 4.5: Fifth root of the electric field intensity distributions in longitudinal planes : xOz and yOz passing through the tip axis.

4.4 Experimental set-up

The experimental set-up developed in the frame of this study is shown in figure 4.6. The BNA on fiber SNOM tip is mounted vertically onto a manual microstage. It is immersed in a cuvette filled with a suspension of 0.5-micrometer large polystyrene latex beads (Alfa Aesar) in water. To stay monodisperse, the particles are inserted into a cationic

surfactant solution of cetyltrimethylammonium bromide (CTAB, > 99% pure, Merck) at a concentration of 5×10^{-4} M [100]. The cuvette is designed to provide 0.17 millimeter-thick flat and transparent walls at two opposite sides and at the bottom for a double cross imaging procedure. The overall system is mounted onto an inverted microscope, equipped with a ($\times 40$, $NA = 0.5$) objective, for imaging the light spot at tip apex with a CCD camera. Note that the fiber SNOM tip is placed close to the cuvette walls to limit aberrations of the imaging systems. A polarization converter is used to define and modify the orientation of the incident polarization on the BNA. The fiber is carefully fixed on holders to prevent polarization changes during experiments. The fiber polarizer is set-up to achieve successively the two desired perpendicular polarization states, which lead to the maximum and minimum tip optical signal outputs. During this adjustment procedure, the tip emission spot is imaged with the vertical far-field imaging channel shown in figure 4.6. The two polarizer adjustments leading to the two orthogonal polarizations are recorded for the following trapping experiments.

4.5 Numerical study

Before discussing trapping experiments, we will show the numerical results that we obtained from FDTD simulations with respect to the configurations experimentally considered. We start by the study of the force calculation exerted by the BNA on tip on a polystyrene bead of 250nm radius. Second, we will extend our numerical investigations to point out the efficiency of the BNAT to trap smaller particles. For this purpose, the trapping of $R=30$ nm latex bead is studied. Finally, the potential is determined in order to quantify the trapping efficiency by comparing it to the Brownian one and effect of the particle weight is also discussed.

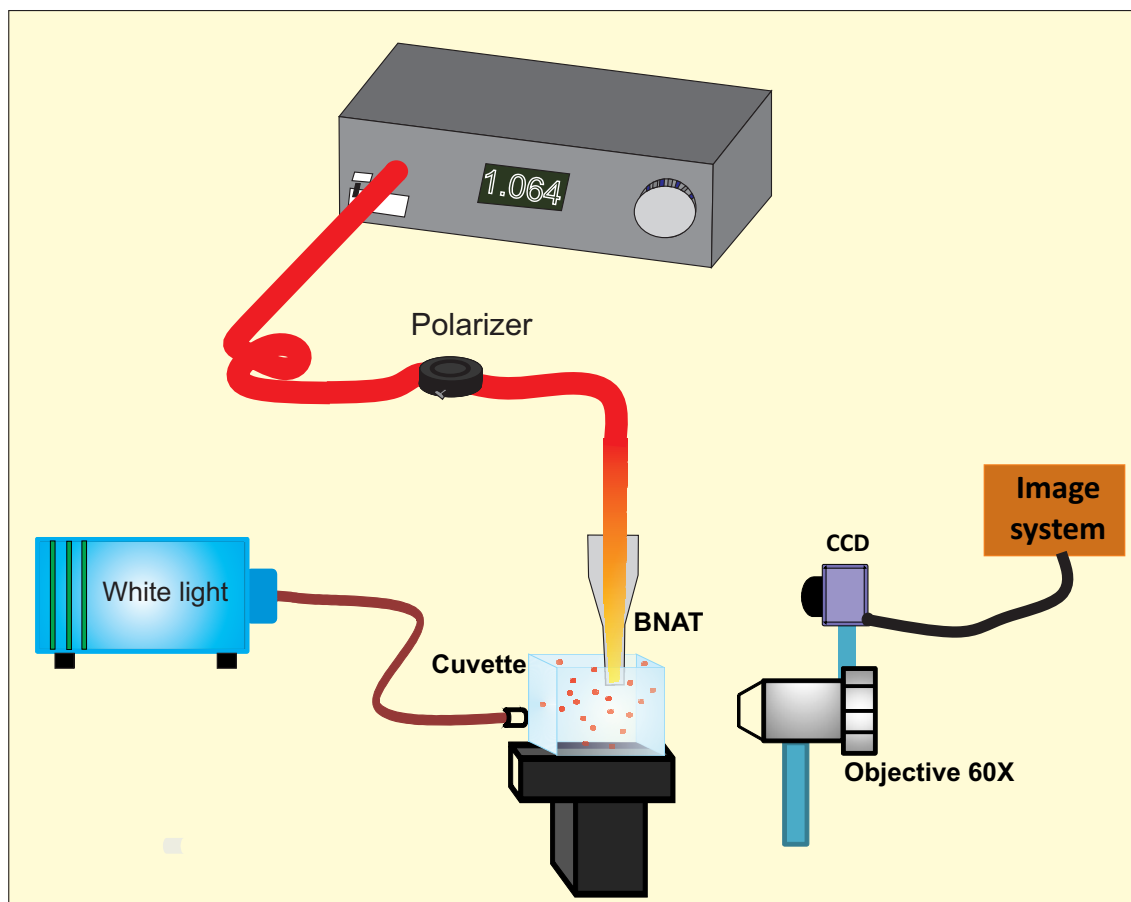


Figure 4.6: Schema of the experimental setup used to the visualization of the particle trapping with the BNAT. Two illumination sources are used: first one thanks to laser @ $\lambda = 1064$ nm that is injected inside the fiber to induce the BNA resonance. The second is a white-light source used to directly illuminated the bowl that contains the suspended particles in water. The visualization of the particle position is obtained through a conventional optical system combining a microscope objective with a CCD camera.

4.5.1 Study of large particle trapping $R = 250$ nm

4.5.1.1 Optical force calculations

First, we study the optical force produced on 250 nm-radius latex particle ($n = 1.45$). The calculation window dimension is $(2.4, 2.4, 2.58)\mu\text{m}$ in x , y and z directions respectively and it is delimited by perfectly matched layer (PML) absorbing boundaries conditions. A

uniform 3D meshing with $\Delta x = \Delta y = \Delta z = 15$ nm is applied to describe the structure (BNAT + dielectric bead). A subgridding technique is employed to faithfully characterize the permittivity of the dielectric nano-bead [101]. The three components of the optical force are then calculated through the eq. 3.18 as mentioned previously in (3.4.2) for different positions of the particle when the latter is moving in a xOz and yOz longitudinal planes.

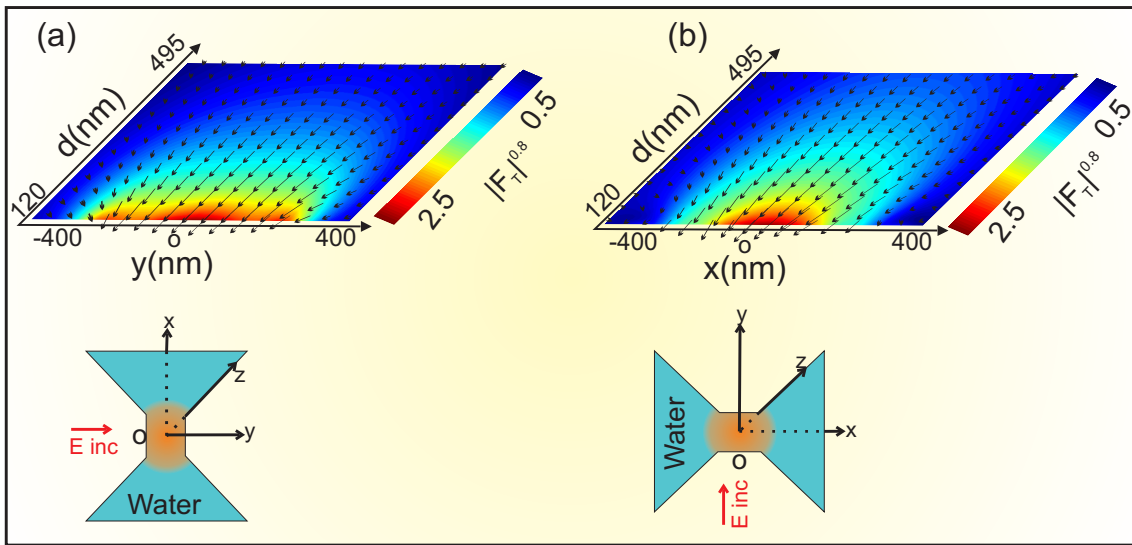


Figure 4.7: Calculated optical forces for latex nanoparticle of radius $R = 250$ nm. (a) Distribution of the force amplitude (0.8 power in order to better see the large variations at small distances) in the yOz plane as a function of the BNAT-latex particle distance d . (b) same as (a) but in the xOz plane.

These results are presented on figure 4.7 a and b where the tangential component \vec{F}_T (\vec{F}_{xz} in (a) and \vec{F}_{yz} in (b)) is indicated by black arrows. We have considered 961 different positions of the particle (i.e. 961 3D-FDTD simulations) where each simulation needs 10 hours CPU-time and more than 5.9Go memory. The color background corresponds to $|\vec{F}_T|^{0.8}$ where the 0.8 power is chosen in order to soften the large variations at small distances. Note that normal component (\vec{F}_y in (a) and \vec{F}_x in (b)) falls to zero. We can observe in figure 4.7 a and b, the arrows converge towards the center of (BNAT) due to gradient pulling force even if the latex nanoparticle is far from the tip axis in both

xOz and yOz . The normalization of the optical force was done by dividing it by the total energy of the incident guided mode inside the tip (Poynting vector flux through a transverse section of the fiber). In order to point out 3D trapping and trajectories of the particle before it is trapped, we also calculate the optical force in two transverse planes (xOy) at two different BNAT to bead distances.

We first consider that the particle is located at small distance ($d = 45$ nm). The obtained three components (F_x, F_y, F_z) of the exerted force by the BNAT are shown in figure 4.8 a where the F_z component is mapped in color level while the black arrows indicate the transverse component (F_x, F_y). Figure 4.8 b show the cross-sections made over the figures 4.8 a, along the Oy -axis which corresponds to the direction of the BNA metallic arms (i.e. to the incident beam polarization direction that induces the BNA resonance). As it can be seen, for $d = 45$ nm, an efficient lateral trapping is obtained in the central zone where all arrows converge toward the center of the figure i.e. the tip axis. In addition, the vertical component (F_z) is positive (as obtained previously in figure 4.7) meaning an attractive force between the BNAT and the latex spherical bead. Unfortunately, the lateral force becomes centrifugal outside a rectangular-shaped area (see the rectangle in black dashed line on figure 4.8 a) meaning a leakage of the particle away from the BNAT. The symmetry of this zone can be deduced from the convolution of the electromagnetic near-field gradient more precisely the Maxwell stress tensor which has the same symmetry properties as the BNA (C_{2v}) by the particle circular symmetry (projection of the spherical symmetry on the xOy plane).

The result has then a (C_{2v}) symmetry properties. The dimensions of this rectangle exactly corresponds to the particle positions for which the vertical projection of the particle on the tip contains the electromagnetic near-field of the BNA. In other terms, if we assume that this near-field is only localized at the BNA edges, the particle positions arise

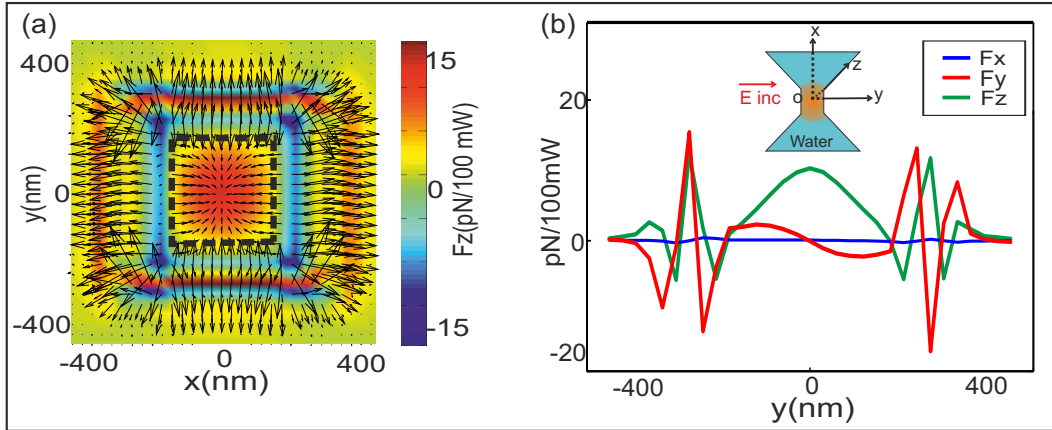


Figure 4.8: (a) is map of the optical force in the plane located at $d = 45$ nm from the tip . The arrows indicate the tangential force component in xOy plane while the color level is associated with the vertical component. (b) Is cross-sections made over the Figures (a), along the Oy -axis which corresponds to the direction of the BNA metallic arms (i.e. to the incident beam polarization direction that induces the BNA resonance).

from $(x = -R + D_x/2)$ to $(x = R - D_x/2)$ in the x -direction and from $(y = -R + D_y/2)$ to $(y = R - D_y/2)$ in the y -direction leading to a rectangle sides of $(L_x = 2R - D_x = 365)$ nm and $(L_y = 2R - D_y = 335)$ nm. Nevertheless, there are many oscillations (instabilities) that appear outside this rectangular area. They are directly linked to the BNA-particle interaction when the curved edge of this latter intersects the BNA electromagnetic near-field. The width of these oscillations is linked to the spatial extension of the electromagnetic near-field around the BNA. In a first approximation, this corresponds to the BNA dimensions (D_x, D_y) .

Let us now consider large BNAT to nano-bead distance ($d = 195$ nm). In this case, we have exploited the symmetry of the structure so that only $\frac{1}{4}$ part of the total area is considered. This leads to decrease the total number of simulations from 961 to only 256. We can note that the oscillations (instabilities) disappear as result of less direct interaction between the BNA and the particle. Moreover, we achieve stable trapping at this distance. We can see very clearly that arrows are always directed toward the center of the BNAT due the gradient force.

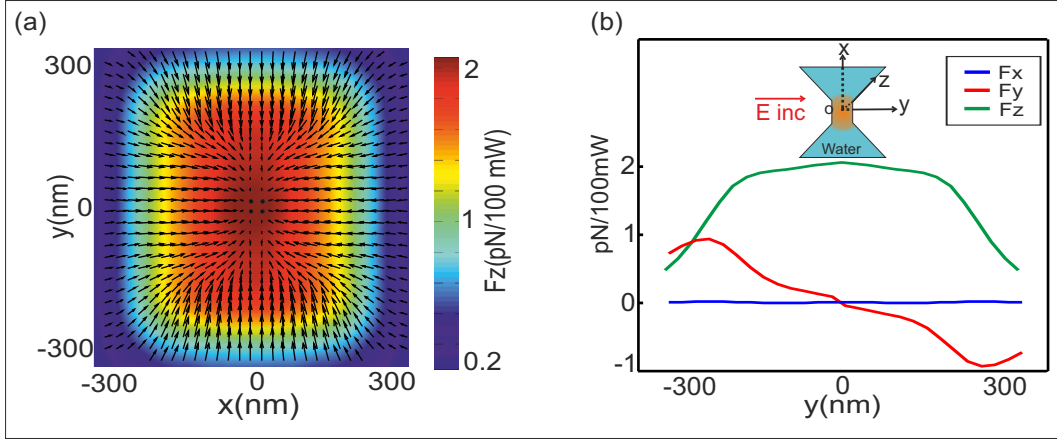


Figure 4.9: (a) is map of the optical force in the plane located at $d = 195$ nm from the tip . The arrows indicate the tangential force component in xOy plane while the color level is associated with the vertical component. (b) Is cross-sections made over the Figures (a), along the Oy -axis which corresponds to the direction of the BNA metallic arms (i.e. to the incident beam polarization direction that induces the BNA resonance).

To determine if this force is sufficient to overcome the Brownian motion, we should calculate the corresponding potential as it will be shown in the following section (4.5.1.2)

4.5.1.2 Potential calculations

The conservative character of the optical force allows to express it through: $\vec{F} = -grad(U)$. Where U is the potential that is defined to vanish at infinity. From this equation, the potential can be numerically calculated as:

$$U(r_0) = - \int_{\infty}^{r_0} \vec{F}(r) \vec{dr} \quad (4.2)$$

To evaluate this integral we need to calculate the force along a continuous path from the infinity to the considered position of the bead. This is clearly impossible. We have made the assumption that infinity distance corresponds to the largest tip-to-bead distance allowed by the FDTD simulations (due to the finite size of the calculation window) and

verifying that, at this position, the force value is very weak compared to small BNAT -to-bead-distance. Consequently, the calculated potential value will be larger than the exact one. We used eq.4.2 to calculate the potential well in two longitudinal planes xOz and yOz . The potential is presented in the two planes in kT units where $k = 1.3806488 J.K^{-1}$ is the Boltzmann constant and T is the absolute temperature taken to be $T=298^{\circ}K$.

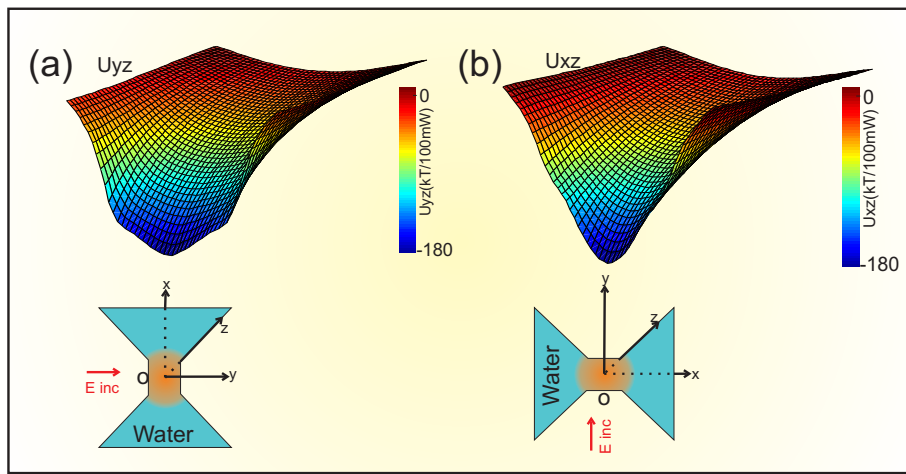


Figure 4.10: Calculated potential well for latex nanoparticle of radius $R = 250$ nm. (a) The associated potential showing a 180 kT well at $d = 120$ nm in yOz plane. (b) same as (a) but in the xOz plane.

Thus, we did integration of trajectory started from farthest position of latex nanoparticle in the longitudinal planes xOz and yOz (at the corner of the calculation window). Currently, efficient trapping requires a minimum of 10 kT [4, 5] potential well if the particle weight is neglected. This last point will be discussed in the following. In our case, this can be achieved with less than 6 mW incident power inside the fiber (see figure 4.10 a and b). One notice that this power is of the same order of magnitude as in the case of coaxial plasmonic aperture studied in [5].

4.5.1.3 Buoyancy calculations of the nanoparticle

The trapping efficiency can also be discussed in terms of force strength without considering the potential. In fact, the maximum theoretical value of the vertical force is $F_z^{max} = 12 \text{ pN}/100\text{mW}$ corresponding to a particle-BNA distance of $d = 45 \text{ nm}$ see figure 4.13. However, trapping is obtained with a minimum light power that can, at least, induce an optical force that allows compensation of the residual weight of the latex sphere in water. The latter is calculated, through the Archimedes' principle that is illustrated in figure 4.11.

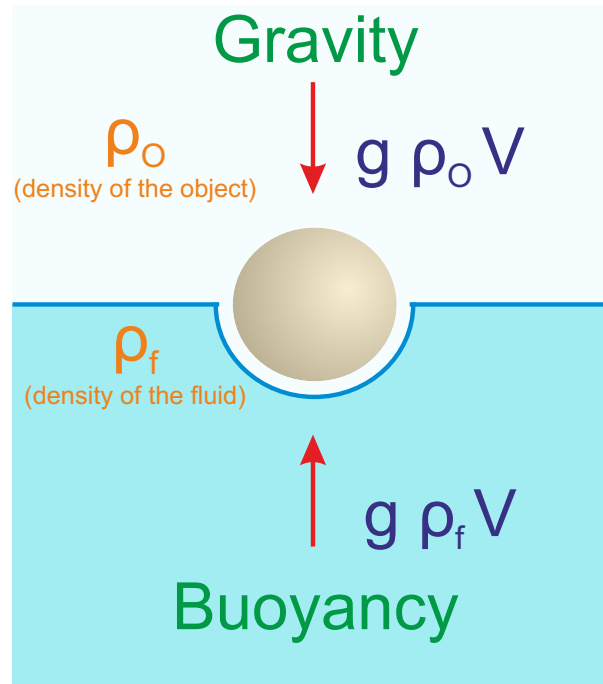


Figure 4.11: Archimedes' principle

The residual weight P_r of the latex sphere in water is calculated by using the following equation:

$$P_r = P_o - P_f \quad (4.3)$$

Where P_o and P_f are the weight of the object "gravity force" and weight of displaced fluid "buoyancy force" respectively. These two quantities satisfy the two following equations:

$$P_o = g \cdot \rho_o \cdot V$$

$$P_f = g \cdot \rho_f \cdot V$$

Where $g = 9.8 \frac{N}{m^2}$ is gravitational acceleration, $\rho_o = \rho_{latex} = 2.634 \text{ g/cm}^3$ and $\rho_f = \rho_{water} = 1 \text{ g/cm}^3$, are volumetric mass densities of latex sphere and water respectively, $V = \frac{4}{3} \cdot \pi \cdot R^3$ is the volume of latex sphere. Thus, we found the residual weight of the latex sphere in water to be equal to $P_r = 1.048 \times 10^{-15} \text{ N}$. Practically, optical forces must be greater to inhibit the Brownian motion of the particle. Consequently, an injected power of only 1 mW leads to an optical force hundred times larger than P_r .

4.6 Experimental vs numerical results

Our theoretical results are in a very good agreement with experiments done by our team [8] where similar BNA on tip was used to successfully trap latex nanoparticles of 250 nm radius. As shown on figure 4.12, optical trapping is obtained when the BNA resonates with injected light power of only 1.2 mW.

In fact, this value is smaller than 3.3 mW that corresponds to the theoretically calculated one needs to get a potential well of 10 kT. Indeed, the latter was determined for a distance $d = 45 \text{ nm}$ instead of a BNA-particle contact. Also from the experimental results, the trapping was never been achieved when the particle comes from the lateral

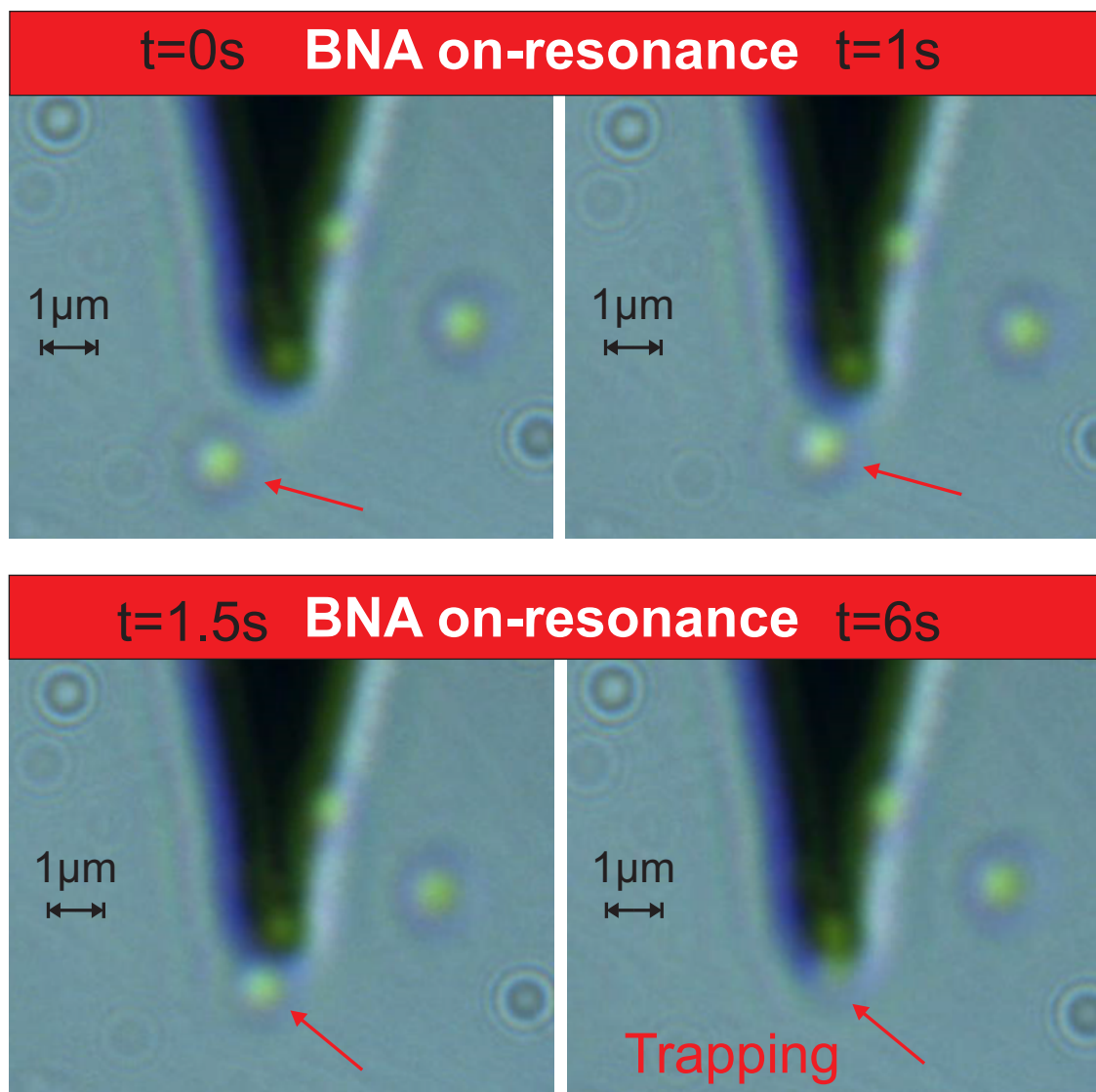


Figure 4.12: Time evolution of the trapping process showing four different positions of the latex particle when the BNA resonates.

side. In fact, the particle was first ejected upwards and then it went down to get into the potential well following a quasi-axial path in front of the tip. This is in very good agreement with results of figures 4.7 a,b and 4.10 a,b which clearly show that 3D trapping can be achieved except if the nanoparticle approaches the tip from the lateral side (see also figure 4.8). The privileged trapping path is then along the tip axis due to efficient attractive vertical force.

In addition, additional experiments were done by T. Grosjean and A. El Eter to qualitatively study the trapping as a function of the light power. Due to the polarization sensitivity of the BNA's resonance, one experimentally modified the light energy near the BNA by manipulating the polarization of the incident beam. The trapping occurred but the particle directly leaved the BNAT. They have estimated the effective power of the light part that is incident on the BNA to 0.7 mW. This theoretically corresponds to a potential well of only 2.1 kT at a tip-particle distance of $d = 45$ nm that is not sufficient to keep the particle in trap.

Due to the high spatial confinement of light in the BNA gap, one can expect possible trapping of smaller particles. Nevertheless, experiments were first done with bigger particles in order to make a direct visualization of the trapping through conventional optical system (diffraction limited beams) as shown on figure 4.12. Nonetheless, trapping of smaller nano-particles by BNAT will be theoretically studied in the following.

4.7 Comparison between conventional metal coated SNOM and BNAT as optical tweezers

Usually, SNOM probes are made of metal coated tapered optical fibers where a cylindrical hole is engraved at their apexes. Such probes were proposed as optical tweezers [4]. Nevertheless, as it will be discussed later, large aperture radius is needed to get electromagnetic resonance inside the cylindrical hole. This kind of SNOM tips are commonly not used because they induce small resolution in the near-field imaging process.

Nonetheless, we have performed numerical simulations to compare the optical forces generated by such a hole aperture tip with the BNAT ones. Let us first emphasize the

force behavior along the BNAT axis. As shown on figure 4.13 a, efficient and monotonic pulling force is obtained for small distances meaning that the trapping corresponds to a bead pressed against the BNA with a potential well of almost 300 kT as shown on figure 4.13 b. This potential well value is sufficient to overcome Brownian motion and allows to trap nanoparticle.

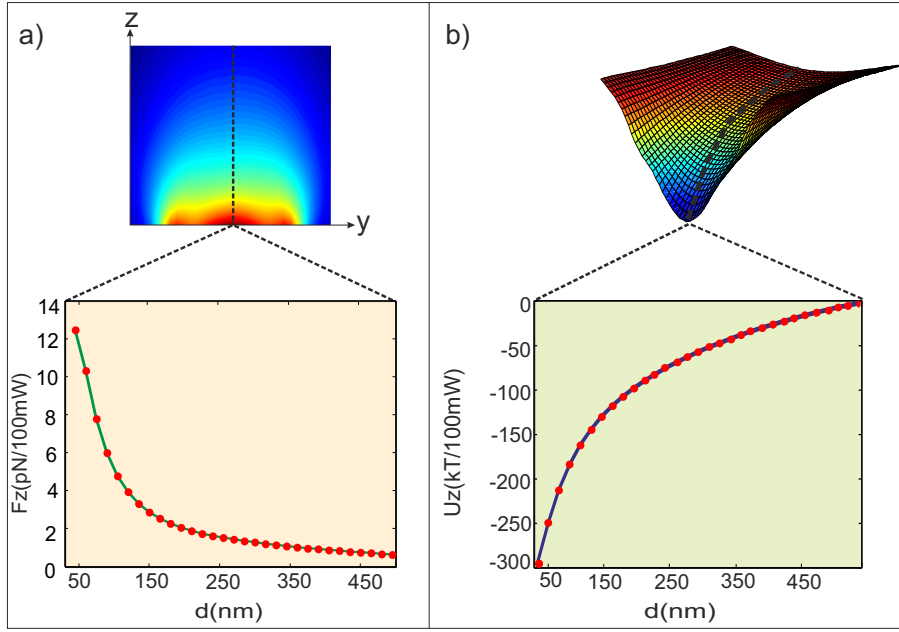


Figure 4.13: (a) Numerical results of vertical force of $R = 250$ nm as a function of the BNAT-particle distance when the latter moves along the tip axis. Smaller values of d are considered in order to quantify the pulling force near the tip apex ($F = 12$ pN/100mW @ $d = 45$ nm). (b) the corresponding potential showing a well of 300kT at $d = 45$ nm.

Two different configurations of hole aperture tip (HAT) are considered: Let us emphasize that the force exerted by a cylindrical aperture having the same opened area as the BNA and larger one exhibiting the same resonance wavelength as the BNAT. Figure 4.14 a presents the electric near-field enhancement factor in both cases. One can clearly see that the small HAT ($R = 56$ nm) did not show any resonance (see solid blue line) in the considered spectral range ($\lambda \in [700 - 1300]$ nm). Consequently, no light confinement is obtained and very small optical force is obtained at $\lambda = 1064$ nm along the tips axis (see solid blue line on figure 4.14 b). On the contrary, if we increase the aperture hole

radius to $R = 150 \text{ nm}$, electric near-field resonance (see dashed red line on figure 4.14 a) appears around $\lambda = 1064 \text{ nm}$ resulting from the excitation at its cutoff wavelength of the fundamental guided mode of the hole aperture waveguide [102]. Consequently, efficient gradient force can be obtained along the tip axis at this resonance but it remains 2 times smaller than the BNAT one. Unfortunately, the transverse spatial extension of the EM at resonance plays a negative role if we attempt to trap a single particle. For all the above reasons, BNAT seems to be more appropriate to act as both optical tweezer and NF probe with resolution estimated to its gap dimension [96].

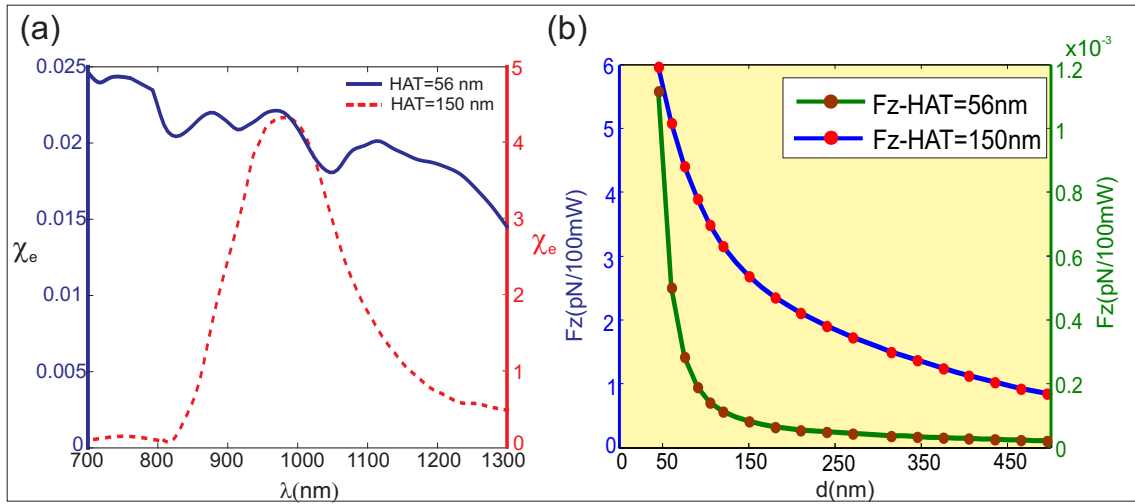


Figure 4.14: (a) Calculated near-field (at 15 nm above the HAT) electric intensity enhancement of the HAT in two case:1) HAT =56 nm blue solid line not show any resonance.2) HAT=150 nm shows a maximum of 0.023 at $\lambda \simeq 1064 \text{ nm}$. (b) Numerical results of vertical force of $R = 250 \text{ nm}$ as a function of the cylindrical aperture-particle distance when the latter moves along the tip axis. Green curve corresponds to same opened area as the BNA, blue curve corresponds to same resonance of BNA

In fact, the light confinement in this case is very weak compared to the BNAT case but the transmitted light power is larger because the opened area is 7 times greater. Note that such a large diameter cylindrical aperture tip can hardly be used in a SNOM imaging experiments because it allows very low resolution and can hardly lead to a good lateral trapping of small particles.

4.8 Study of small particle trapping

As presented previously in (4.5.1.1) and (4.5.1.2) for the calculation of the optical force and the potential for the large radius, we used the same procedures to numerically study the case of two smaller spherical latex particles with radius of $R = 100$ nm and $R = 30$ nm respectively. First, the numerical simulation in longitudinal planes xOz and yOz are performed. Obtained results for the force and potential are presented on figures 4.15 and 4.16. The trapping is demonstrated for both particles. Nevertheless, the force gradients are different from one to the other. For the particle of radius $R = 100$ nm, one can see the occurrence of a non monotonic evolution of the force versus the distance d as shown in figure 4.15 c with a depletion between $d = 45$ nm and $d = 135$ nm at $d = 75$ nm.

Nevertheless, as seen on the figure 4.15 c, a small potential well (only $U = -140$ kT) is obtained, leading to a pulling force that will press against the BNAT similarly to the case of 250 nm-radius particle. This becomes completely different for the smallest studied particle of radius $R = 30$ nm as shown in figure 4.16. A change of the vertical force sign occurs for $d < 139$ nm meaning a repulsive force on the particle see figure 4.16 c. At this distance, the potential exhibits a well of $U = -47$ kT meaning a trapping of the particle without tip contact as shown on figure 4.16 d. We believed that this can only be due to an increase of the radiation pressure relative to the gradient force. In fact, the particle is too small to induce a modification of the spatial distribution of the EM near-field generated by the BNAT. In this case, the particle can be seen as completely opaque so that gradient force decreases (as for a metallic particle).

Then, we calculated the optical force exerted on the particles in a transverse plane xOy placed at two different distances from the BNAT. In both cases, these distances correspond to a stable trapping position of the particle along the z -axis. The $R = 100nm$

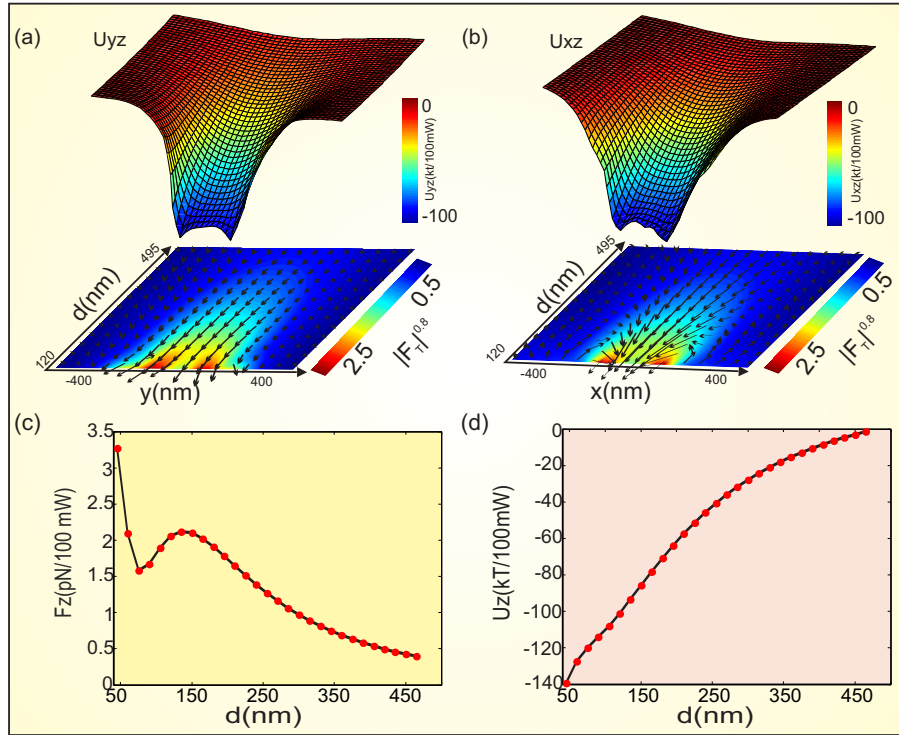


Figure 4.15: Calculated optical forces for latex nanoparticle of radius $R = 100$ nm. (a) bottom : distribution of the force amplitude (0.8 power in order to better see the large variations at small distances) in the yOz plane as a function of the BNAT-latex particle distance d . (a) top : the associated potential showing a 100 kT well at $d = 120$ nm. (b) same as (a) but in the xOz plane. (c) vertical force as a function of the BNAT-particle distance when the latter moves along the tip axis. Smaller values of d are considered in order to quantify the pulling force near the tip apex ($F = 3.5$ pN/100mW @ $d = 45$ nm). (d) the corresponding potential showing a well of 140kT at $d = 45$ nm.

particle is located at small distance ($d = 45$ nm) and for the smaller particle $R = 30$ nm at the distance ($d = 105$ nm). The obtained three components (F_x, F_y, F_z) are shown in figures 4.17 a and 4.18 a where the F_z component is mapped in color level while the black arrows indicate the transverse component (F_x, F_y). Figures 4.17 b, 4.18 b show the cross-sections made over the figures 4.17 a, 4.18 a, along the Oy -axis which corresponds to the direction of the BNA metallic arms (i.e. to the incident beam polarization direction that induces the BNA resonance). As the same calculation of the particle $R = 250$ nm, we have considered 961 different positions of the particles (i.e. 961 3D-FDTD simulations).

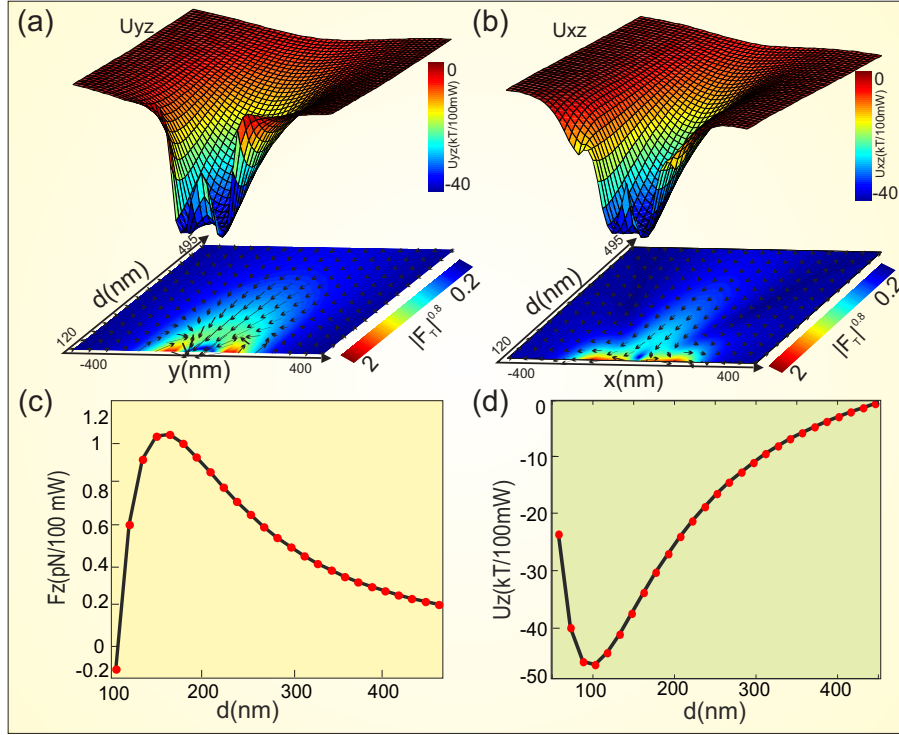


Figure 4.16: Calculated optical forces for latex nanoparticle of radius $R = 30$ nm. (a) bottom : distribution of the force amplitude (0.8 power in order to better see the large variations at small distances) in the yOz plane as a function of the BNAT-latex particle distance d . (a) top : the associated potential showing a 40 kT well at $d = 120$ nm. (b) same as (a) but in the xOz plane.(c) vertical force as a function of the BNAT-particle distance when the latter moves along the tip axis. Smaller values of d are considered in order to quantify the pulling force near the tip apex ($F = 1.2$ pN/100mW @ $d = 105$ nm). (d) the corresponding potential showing a well of 47kT at $d = 105$ nm.

As it can be seen from figure 4.17, the particle with radius $R = 100$ nm shows not efficient lateral trapping in the central zone where all arrows converge toward the rectangle edge. This happens as result of the interaction between the BNAT and the particle. Since, the particle has small radius and at small distance from the tip apex the electromagnetic field leads to instability of optical trapping. For the $R = 30nm$ radius particle, the xOy plane is placed at $d = 105nm$ that correspond to a stable trapping along the z -direction as mentioned before. The obtained force components in this plane are plotted in figure 4.18a (bottom) where all arrows are also indicating efficient lateral trapping of the particle. In addition, the vertical component (F_z) minimum in this plane at $d = 105$ nm.

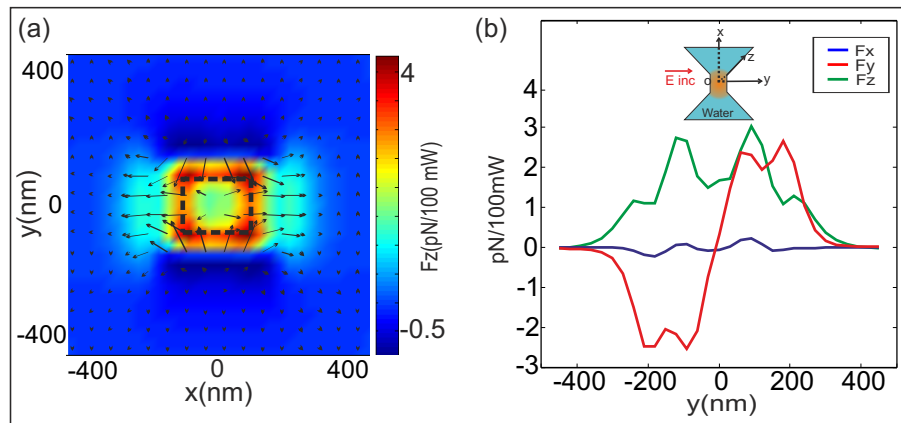


Figure 4.17: (a) is map of the optical force in the plane located at $d = 45$ nm from the tip of $R = 100$ nm. The arrows indicate the tangential force component in xOy plane while the color level is associated with the vertical component. (b) is cross-sections made over the figure (a), along the Oy -axis which corresponds to the direction of the BNA metallic arms (i.e. to the incident beam polarization direction that induces the BNA resonance).

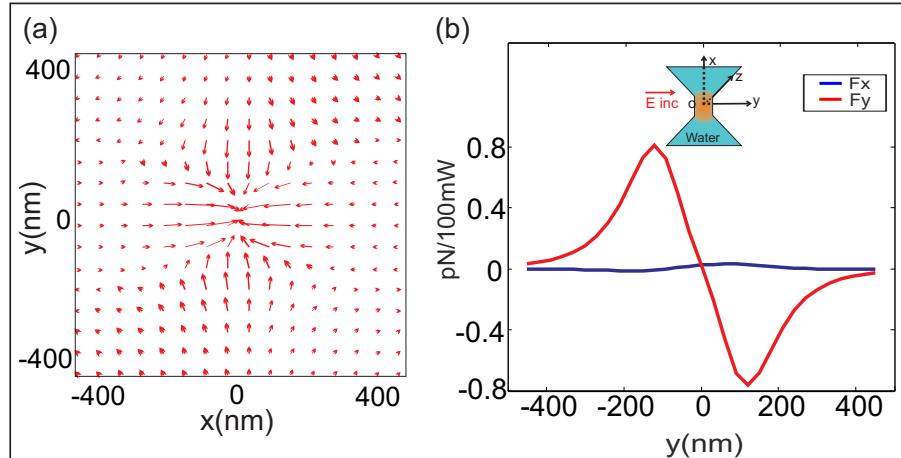


Figure 4.18: (a) The optical force in the plane located at $d = 105$ nm from the tip of nanoparticle with $R = 30$ nm where the arrows indicate the tangential force component in xOy plane. (b) is cross-sections made over the figure (a), along the Oy -axis which corresponds to the direction of the BNA metallic arms (i.e. to the incident beam polarization direction that induces the BNA resonance).

4.9 Conclusion

In summary, we have theoretically and numerically studied the optical trapping of polystyrene latex particles thanks to a standalone fibred optical tweezers based on the combination of a metal coated SNOM probe and a bowtie nanoaperture antenna engraved at its apex. Experiments well agree with numerical simulations performed within a latex particle radius of $R = 250$ nm where trapping has been studied as a function of the illumination light power. Supplementary numerical simulations show that this configuration is able to trap smaller particles even if the involved potential wells are lower. We continue our theoretical and experimental investigations to highlight and better understand the trapping process in the case of nanosized particles where it is expected but under certain constraints (appropriate initial spatial position of the particle and substantial light power) without risking destruction of the BNAT by optical heating for example.

Chapter 5

Application 2: Optical tweezers based on Diabolo Antenna (DA)

5.1 Introduction

In this chapter, we are interested to address another kind of nano-antenna as efficient optical tweezers. In fact, even if monopole, dimmer, bowtie-shaped or bowtie nano-aperture antennas are good candidates to confine light down to the nano-scale, only electric field confinement occurs within such structures. To exacerbate the optical force, it is possible to increase both the electric and the magnetic field confinement. Metallic nanorings [103, 104] or diabolo nano-antenna (DA)[105] were recently proposed as magnetic field detectors due to their specific magnetic properties. The DA was recently proposed to generate huge magnetic near-field when illuminated by linearly polarized wave along its axis. The Nano metal structure able to generate greatly enhanced electromagnetic fields in order to their form and composition [10, 106]. Recent demonstrated in nano optics is nano-antenna, bowtie Nano antenna (BA) [107, 55] and Bowtie Aperture Antenna

(BAA) [108], which can confine and enhance the electric field. Additionally, in recent study confinement and enhancement magnetic field by applying Babinet's principle, in near infrared by using the complement of a Bowtie Aperture Antenna (BAA) called diabolo antenna (DA) [9] have been investigated. Figure 5.1 c shows optical plasmonic trapping of 350 nm polystyrene particles with nanoblock pairs. The plasmonic trapping takes place in the red cycles of (c). Bright scattered light is observed around pairs. When nanoparticles pass sufficiently close to pairs, they get trapped and appear as bright scattering centers [9].

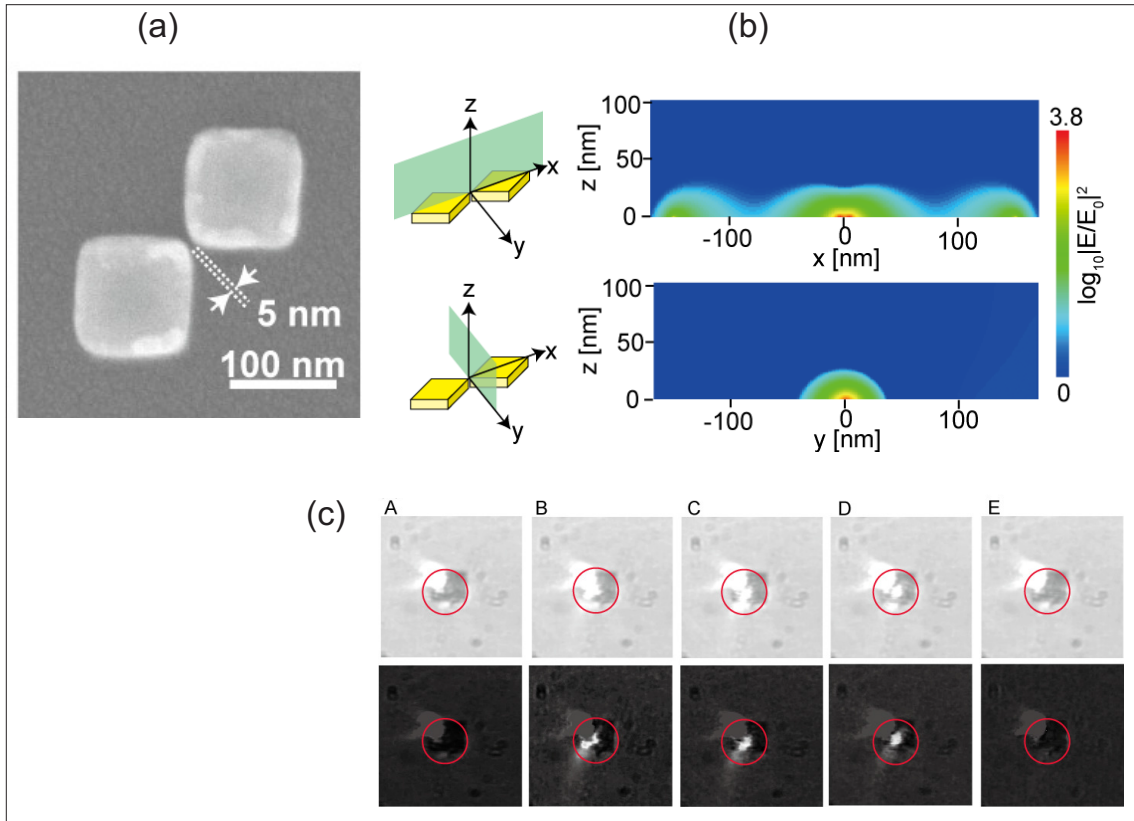


Figure 5.1: (a) SEM of pairs of gold nanoblocks with 5 nm gaps. (b) Calculated near-field distributions near a model gold nanoblock pair at an 800-nm incident wavelength. Block size = $80 \times 80 \times 30$ nm and gap distance = 5 nm for xz plane yz plane on the pair as shown to the left side of panels respectively. (c) Optical plasmonic trapping of 350 nm polystyrene particles with nanoblock pairs [9].

Babinet's principle is a traditional concept of the light wave theory. It had been

used to make simple analysis of some diffraction problems [109, 110] and implemented as an approximation for meta materials with limited thickness [111, 112]. By using nano designed plasmonic dipole antennas, gold nanoparticles with 10 nm trapped [113, 60, 114]. The study of Diabolo Antennas (DA) interested of the electric and magnetic field enhancement. It contribute of increase the optical forces which generated on dielectric nano particles to exploited it for optical trapping.

Numerical 3D-(FDTD) simulation results demonstrate the high confinement of the electromagnetic field in the vicinity of the DA. We propose here to exploit this enhancement of the magnetic field for the trapping of Nps as small as 25nm radius. Results show that, by adjusting the DA geometry, it is possible to get a double electro-magnetic confinement in the vicinity of the DA gap zone. Moreover, the trapping process depends on the Np dimensions and that, for specific geometries, trapping without contact can be achieved. This doubly resonant structure opens the way for the design of a novel generation of efficient optical nano-tweezers.

5.2 Diabolo nano-Antenna (DA) properties

The diabolo antenna is inspired by the principle of Babinet, which specifies that electromagnetic field diffraction by any aperture in an infinitely thin layer of perfect metal, are the same as those diffracted by the complementary structure [115], provided replacing the magnetic field by the electric field and vice versa. To numerically check this principle, we consider the case of a DA for which the complementary structure is a BNA as shown in figure 5.2 a and b. BNA allows electric field enhancement ¹ due to a capacitive effect (charge accumulation at the edges of the metallic arms (see figure 5.2 c)) while the DA

¹Let us recall that electric or magnetic enhancement factors (χ_e and χ_m) are defined, as in the previous chapter, as the ratio of the square modulus of the field with DA to the same quantity without DA

can be seen as an inductive component allowing charge to travel between these arms (see figure 5.2 d). Let us note that the two above effects (capacitive or inductive) are induced by the EM field component that is directed along the antenna-axis that is defined by the metallic arm axis. Numerical simulations were performed in two different cases: DA and BNA made on perfect conductor or on real metal (gold for instance). Near-field (5 nm above the NA) enhancement spectra of the electric and magnetic fields are presented on figure 5.3 for $D=135\text{nm}$, $G=15\text{nm}$ and $T=20\text{nm}$. As it can be seen, the Babinet principle is almost verified in the near-field only for perfectly conductor while a discrepancy appears in the case of gold. This can be attributed to the EM field penetration inside the metallic part of the NA.

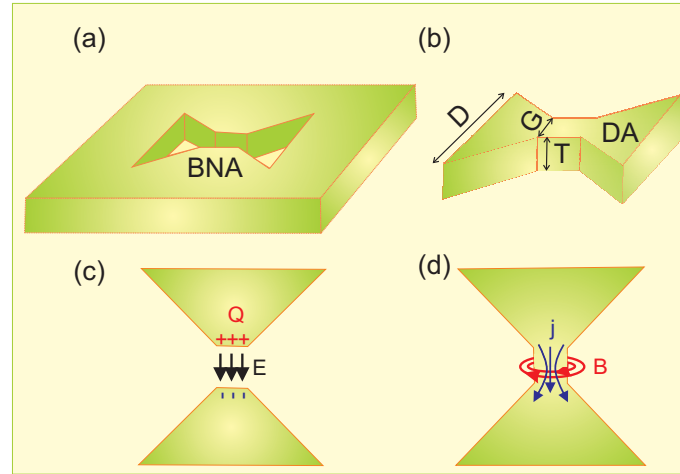


Figure 5.2: (a) 3D view BNA and (b) its complementary DA nano antenna. (c, d) Physical principles of EM field confinement appears in the bowtie nanoaperture and diabolo nanoantennas.

5.3 Optimization of the diabolo antenna geometry

As mentioned in the previous chapter, optical trapping is commonly performed in liquid in order to compensate the particle weight by the buoyancy. Consequently, we have performed 3D simulation of DA placed in water as function of DA geometrical dimensions.

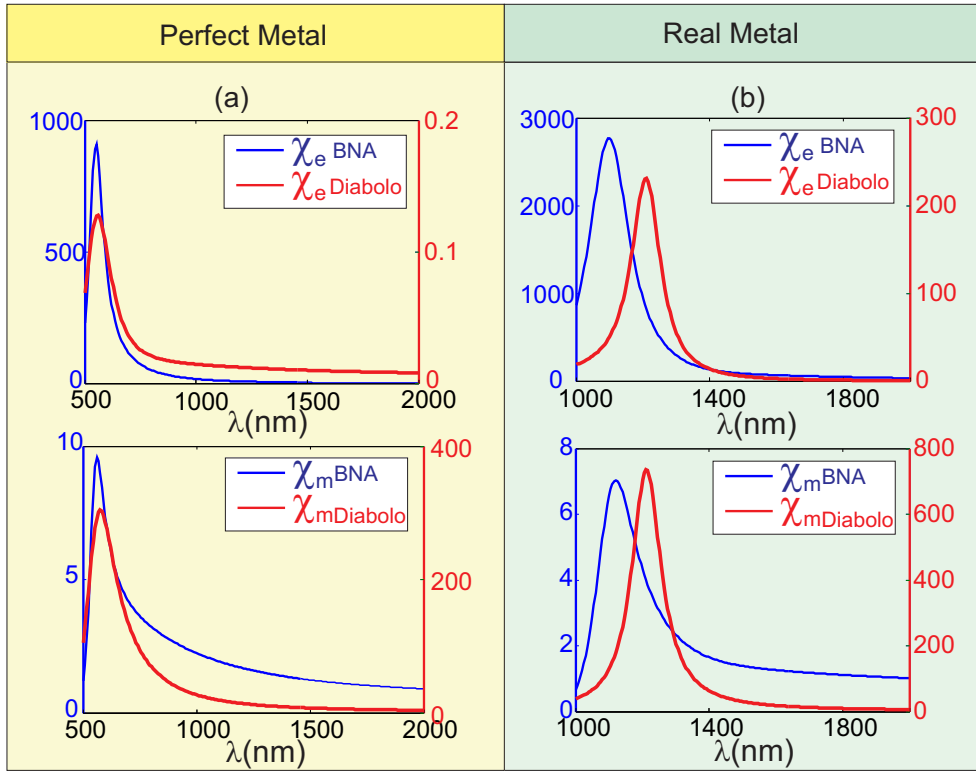


Figure 5.3: Near-field electric and magnetic spectral responses of Diabolo nanoantenna (DA) and its complementary structure Bowtie nanoaperture antenna (BNA) .(a) Perfect metal.(b) Real metal.

The figures 5.4 a,b show the electric and magnetic spectral responses of different DA length D with fixed $G = 25$ and $T = 20$ nm. Four different values of D are considered: $D = (135, 145, 155, 165)$ nm to point out the influence of this parameter on both the enhancement factor and the resonance wavelength value. The results demonstrate very clearly the high magnetic field enhancement compared to the electric field one as shown in figure 5.4 a,b. We note from this figure that electric and magnetic resonances occur at the same wavelength value whatever the NA length. This result is very important since we attempt to get simultaneous electric and magnetic confinement. In addition, the electric field enhancement factor seems to be independent of the D parameter while the magnetic one linearly increases with D .

Similar studies were performed by varying, first, the gap size G (see figure 5.5) keeping

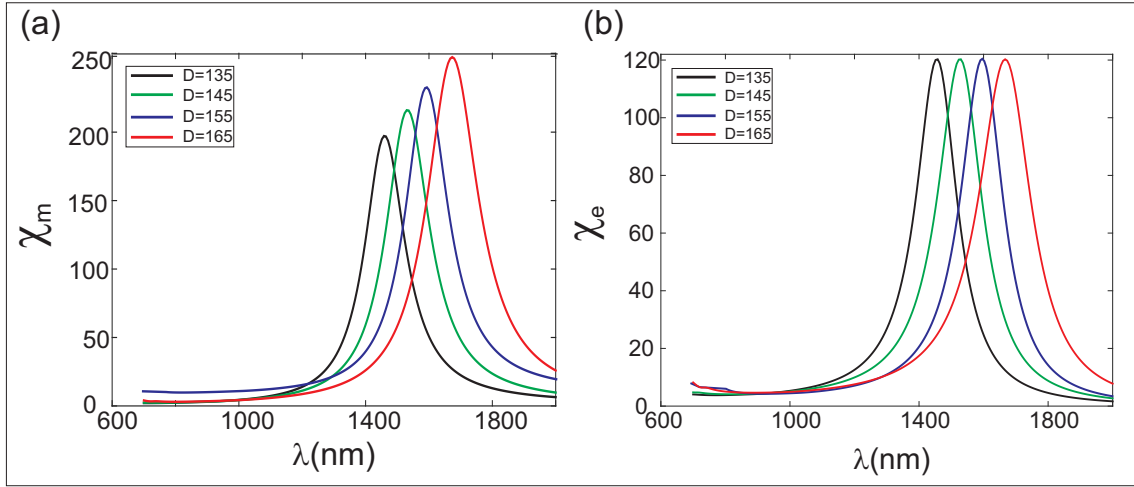


Figure 5.4: (a)Magnetic and (b)Electric spectral responses as a function of length D with fixed value of $G = 25$ and $T = 20$ nm of a gold DA immersed in water.

$D = 135$ nm and $T = 20$ nm and, second, the thickness T (see figure 5.6) for fixed values of $D = 135$ nm and $G = 25$ nm. We can notice, that in both cases, the resonance wavelength evolves by decreasing G and/or when T increases. In addition, the grow of the resonance wavelength (RW) is always accompanied by an increasing of the electric and magnetic field enhancements. Results of figures 5.4,5.5,5.6 can be exploited to fix the geometry of the DA as a function of the desired value of the RW. To elucidate the relation between the RW/enhancement factor and these geometrical parameters, we took the RW and maximum factor of enhancement values varying with DA geometrical parameters as shown in figure 5.7 a,b,c. The obtained results showed almost linearly behaviors in each DA parameters except DA thickness T .

From these studies, and according to the technological constraints and optical sources that are available in our team, we have fixed the DA geometry to a total length $D = 135$ nm.

Let us notice that this geometry can be adapted as function of the surrounding media. The DA resonance wavelength evolves linearly with the refractive index of the media

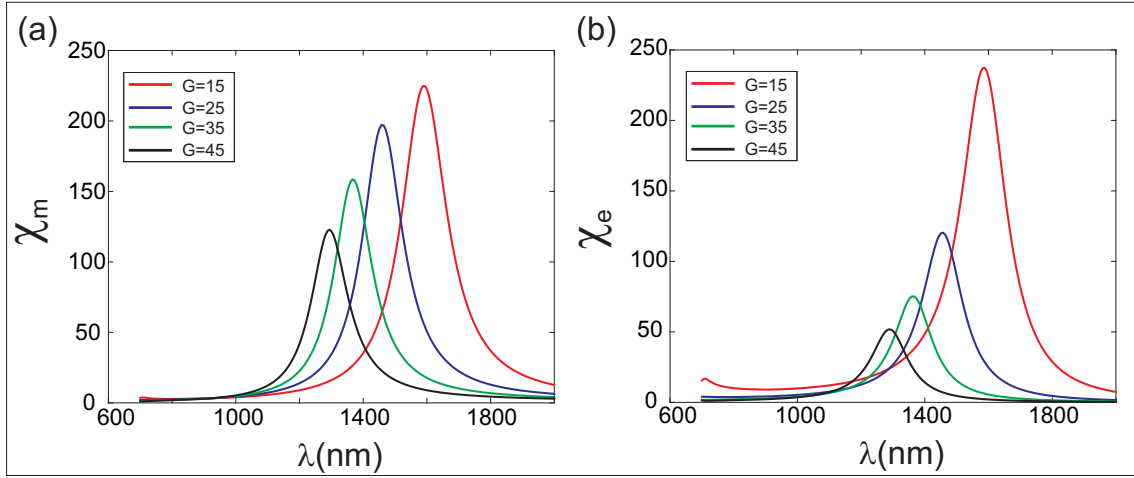


Figure 5.5: (a)Magnetic and (b)Electric spectral responses as a function of gap G with fixed value of $D = 135$ and $T = 20$ nm of a gold DA immersed in water.

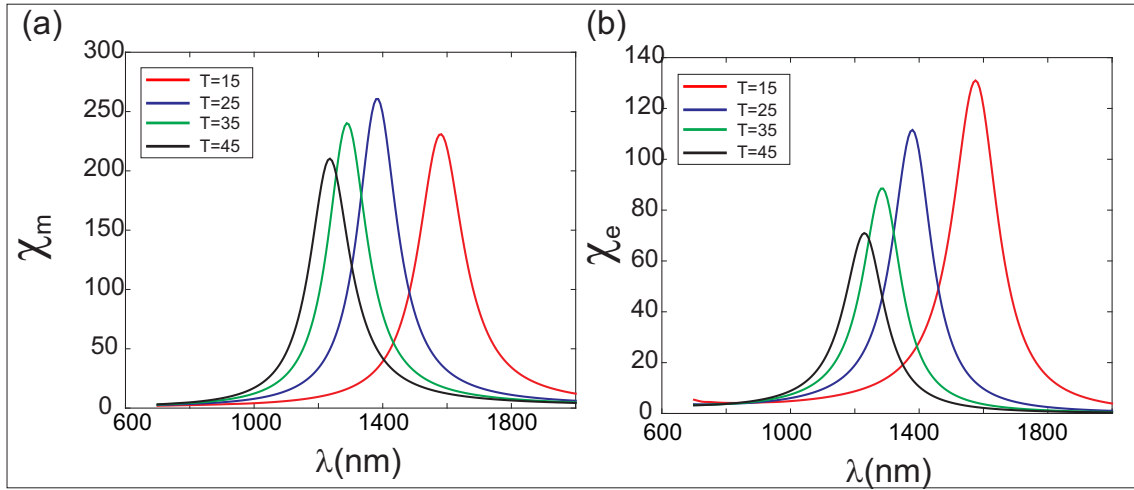


Figure 5.6: (a)Magnetic and (b)Electric spectral responses as a function of gap T with fixed value of $D = 135$ and $G = 25$ nm of a gold DA immersed in water.

($\lambda_{res}^{H_2O} \times n_{air} = \lambda_{res}^{air} \times n_{H_2O}$) as it can be seen from figure 5.8 where the cases of air and water are compared. The enhancement factors of the magnetic and electric fields are given in figure 5.8 a and 5.8 b respectively when the illumination is a plane wave linearly polarized along the DA axis (magnetic resonance is induced). As expected, both fields are efficiently enhanced over a broadband spectral range (resonance with small quality factor ~ 10). Indeed, one obtains $\chi_e^{air} = 171.7$ and $\chi_e^{H_2O} = 120.3$ at $\lambda_{res}^{air} = 1112$ nm

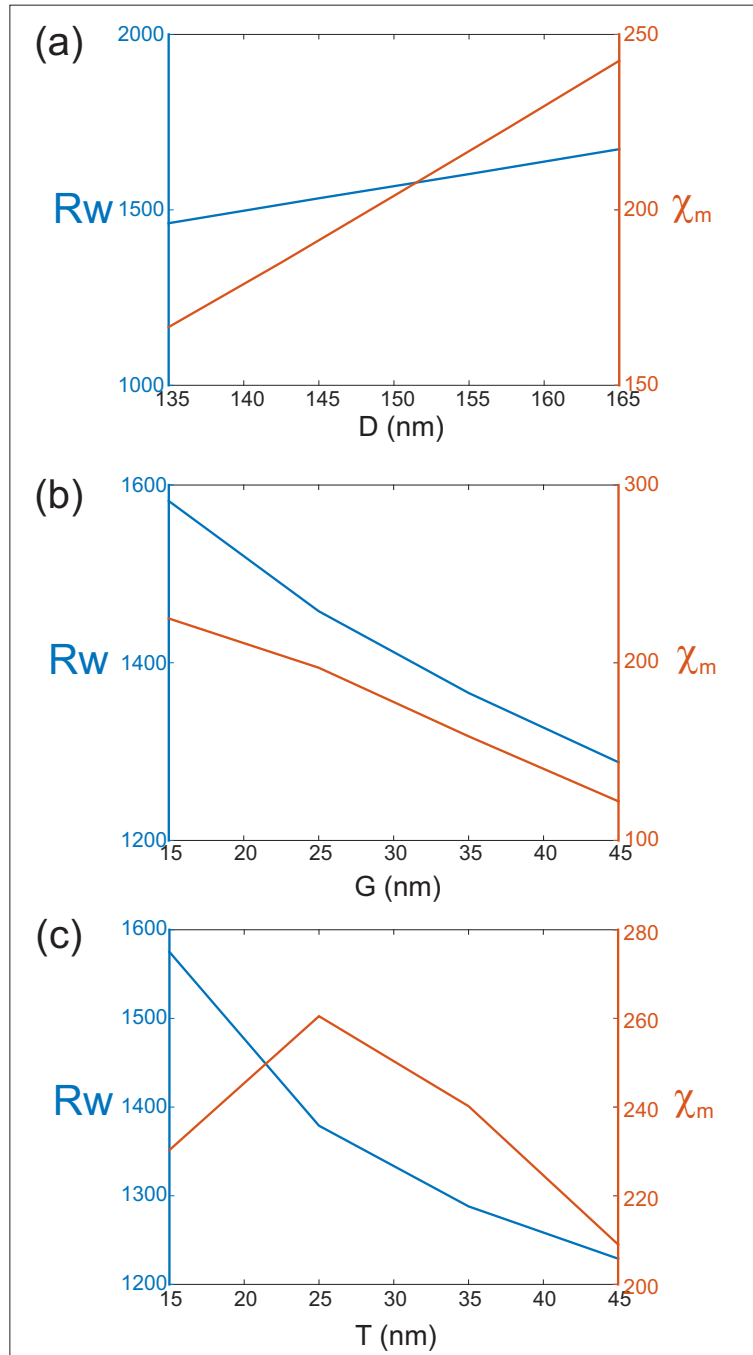


Figure 5.7: The relation between RW/enhancement factor and DA geometrical parameters a) DA length D. b) DA gap G. c) DA thickness T.

and $\lambda_{res}^{H_2O} = 1458 \text{ nm}$ respectively. Moreover, the magnetic field responses presented in figure 5.8a show larger enhancements than for the electric field with $\chi_m^{air} \simeq 285.8$ and $\chi_m^{H_2O} \simeq 197.2$ at the resonance wavelengths.

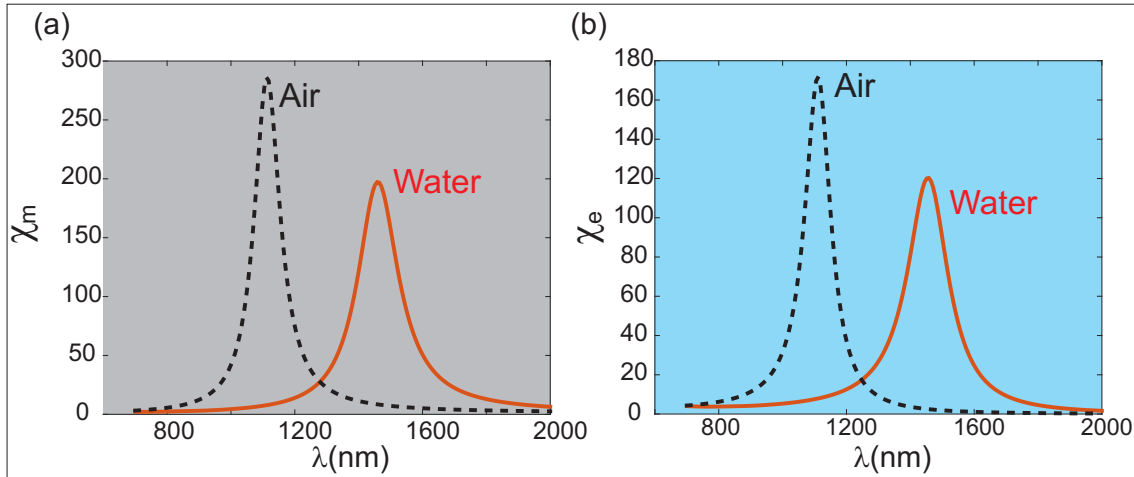


Figure 5.8: (a)Magnetic and (b) electric spectral responses of a gold DA with $D = 135$ nm, $G = 25$ and $T = 20$ nm immersed in air (black dashed lines) and in water (red solid lines).

Figure 5.9 a presents the distribution of magnetic and electric fields in water at ($\lambda_{res}^{water} = 1458$ nm) along a transverse (xOy) plane 5 nm above the DA (transmission side). As expected, an enhanced magnetic field is obtained all around the metal gap while the enhancement of the electric intensity arises mainly at the corners of the nanoantenna. The highly confined distribution of the magnetic field around the metal gap shows that the resonance mode (probably a localized plasmon resonance) incurred by the diabolo nanoantenna is linked with an effective wavelength much smaller than the vacuum wavelength. This property may be happened as result of the triangular geometries of the diabolo nanoantenna since triangular and conical structures are known to support plasmon modes of very small wavelengths [116, 117]. The equivalent field distributions in a vertical xOz and yOz are presented on figure 5.9 c,d,e,f respectively. They confirm the strong confinement of the magnetic field all around the gap zone while the electric field is slightly more confined at the corners than at the DA center. The white arrows of figure 5.9 f show the direction of the tangential magnetic field that is rotating around the DA axis as due to the presence of an oscillating electric current between the DA metallic arms inside the metal gap.

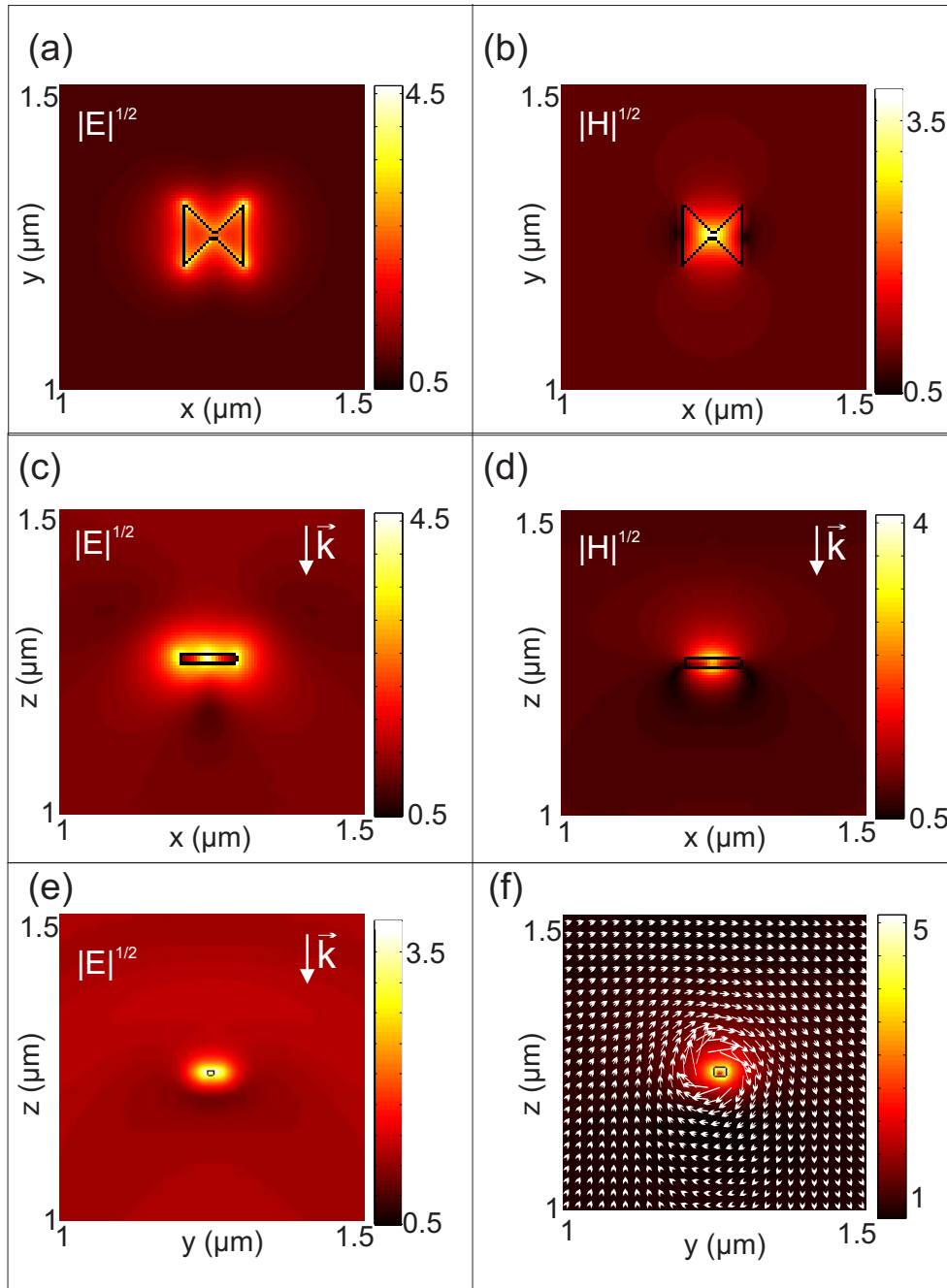


Figure 5.9: (a),(b) Show the magnetic and electric field distributions at resonance immersed in water ($\lambda_{res}^{water} = 1458 \text{ nm}$) along a transverse (xOy) plane and (c),(d),(e),(f) in the longitudinal planes (xOz, yOz) at 5 nm above the DA.

5.4 Optical force calculations with the diablo antenna

In this paragraph, we first study the optical force exerted by a plane wave on a self-suspended DA in air and in water. We will show how the EM field redistribution, induced by the DA resonance, acts on the DA and enhances the radiation pressure. In a second part, we consider the DA as a nano-tweezer deposited on a flat interface substrate to trap spherical nano-beads.

5.4.1 Optical force on self-suspended diablo antenna

First, we have calculated the optical force generated on the DA when it is illuminated by a plane wave linearly polarized along its axis (x-axis here to induce the DA resonance) and along the perpendicular direction (off-resonant DA). Indeed, the redistribution of the EM field around the DA due to its resonance can lead to enhance the radiation pressure. This is verified through the results presented in figure 5.10 where longitudinal (along the illumination direction) resulting force, per unit of incident power (here $100mW$) on the DA, is shown for the two cases as a function of the wavelength. A maximum of force only appears when the DA resonates and its value is almost 121 times greater than the off-resonance case for a DA immersed in air and 91 times larger in water.

The same phenomenon exists for other Np geometries provided electromagnetic (electric and/or magnetic) resonance of the Np. Indeed, the more is the scattering cross section of the Np, the more the modification of the electromagnetic field around it is important and the more the radiation pressure can be large. In order to exploit this field redistribution (high confinement at the gap zone), we will consider a tied DA to a flat substrate in order to see how it can act as a tweezer for the trapping of Nps.

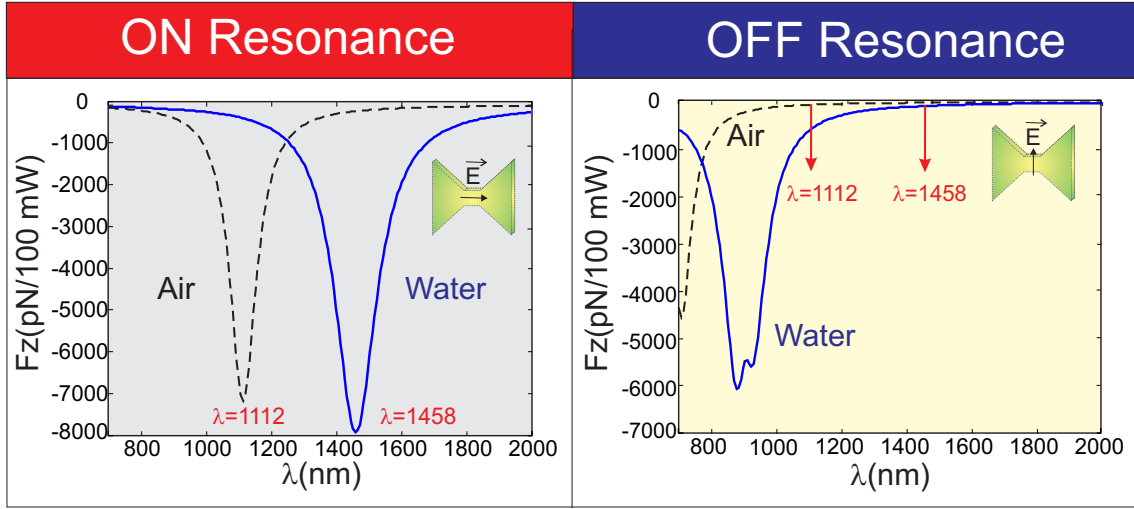


Figure 5.10: Numerical results of the optical force of DA immersed in air (black dashed lines) and in water (blue solid lines) as a function of the wavelength in two cases: 1) DA on resonance 2) DA off resonance.

5.4.2 Optical force exerted by a diabolo antenna on nanoparticle

After these preliminary results on the DA itself, we propose to use it as an efficient optical tweezers where forces are exalted by doubly increasing and confining the electric and the magnetic fields. From the last section (5.3), we obtained large enhancement factors of both electric and magnetic fields that could lead to increase the optical forces exerted on Nps placed in front of the DA. A sketch of the proposed gold Diabolo antenna is shown in figure 5.11. The Diabolo antenna is supposed to be deposited onto a glass substrate $n_s = 1.49$ and surrounded by a liquid (water $n_{water} = 1.315$) that holds the NPs. As mentioned previously, the presence of the liquid is essential to compensate the Np weight by the buoyancy. First, we have calculated electric and magnetic near field spectral response of the DA on substrate. Figure 5.12 give the enhancement factors of the magnetic and electric fields respectively when the incident polarization is directed along the DA axis. The magnetic field enhancement presented in figure 5.12 shows larger efficiency than for the electric field with $\chi_m \simeq 169.3.5$ and $\chi_e \simeq 126.1$ at the resonance

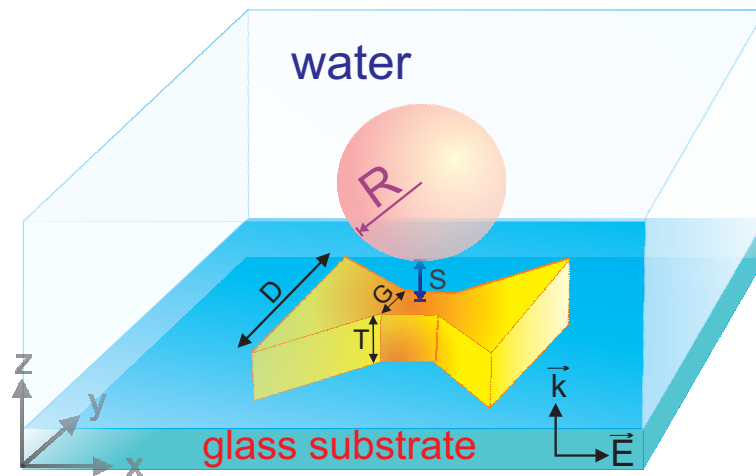


Figure 5.11: Schematic of the diablo nano-antenna D is the total length in both x and y directions, G is the gap size and T is the thickness in z direction onto a glass substrate and N_p as sphere with radius R surrounded by water.

wavelengths that passes from $\lambda = 1458 \text{ nm}$ in the case of self-suspended DA in water to $\lambda_{res} = 1523 \text{ nm}$ for the DA on substrate. This variation of the RW is similar to what it was theoretically expected [118] and experimentally observed [119] with another kind of nano-antenna, namely a BNA made in aluminum.

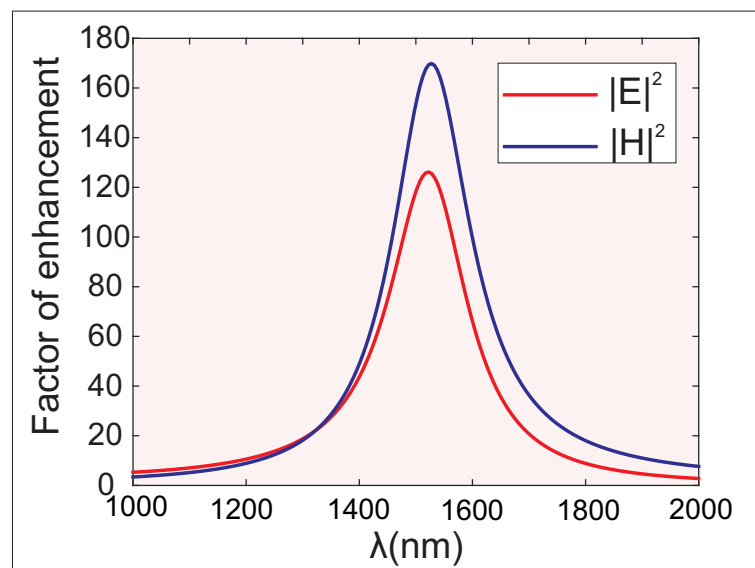


Figure 5.12: Magnetic and electric spectral near-field responses of a gold DA with $D = 135 \text{ nm}$, $G = 25$ and $T = 20 \text{ nm}$ deposited on a glass substrate and immersed in water.

At the first glance and compared to the enhancement of the electric field generated at the vicinity of the BNA, the DA seems to be more able to act as a nanotweezer. Unfortunately, there is a major discrepancy between the two nano-antennas: contrarily to the BNA, the electromagnetic field exerted on the Np presents a predominant part (radiation pressure) when it is far from the nano-antenna. Thus, we expect an efficient trapping only for small DA-to-Np distances. In addition, the effect of this background illumination may lead, according to the Np dimension, to a trapping position without contact (compensation of the radiation pressure by the gradient force). To investigate all these assumptions, we have made extensive simulations to quantify the force exerted on dielectric Np. We presents here three different studies where only the Np position along the vertical axis passing by the DA center (perpendicular to the substrate plane) is considered. The calculated vertical force F_z (the only non zero component of the force) is normalized by the total energy impinging the DA. In the first study, the radius of the Np is fixed while its position varies together with the illumination wavelength. In the second study, the distance S is fixed and the two other parameters vary (R and λ). Last study is done when fixing the wavelength and varying R and S. The corresponding results are shown of figures [5.13](#), [5.14](#) and [5.15](#).

We found that optical trapping of the Np depends on all these parameters. For each case, two different zones, the attractive and the repulsive ones, are pointed out with a separation line of zero vertical force corresponding to the trapping of the Np. According to the coordinate system in figure [5.11](#) a negative value of F_z corresponds to an attractive force while positive one leads to push the Np away from the DA.

In figure [5.13](#), four values of the Np radius are considered: R=30, 40, 55 ,70 and 90 nm. For R=30 nm, figure [5.13](#) a shows that attractive force occurs at small distance S for small values of the wavelength (<1800 nm). The yellow line represents the separation

between the two zones. One notes that when trapping occurs, it corresponds necessarily to a contact between the DA and the Np because the potential well is located on the DA.

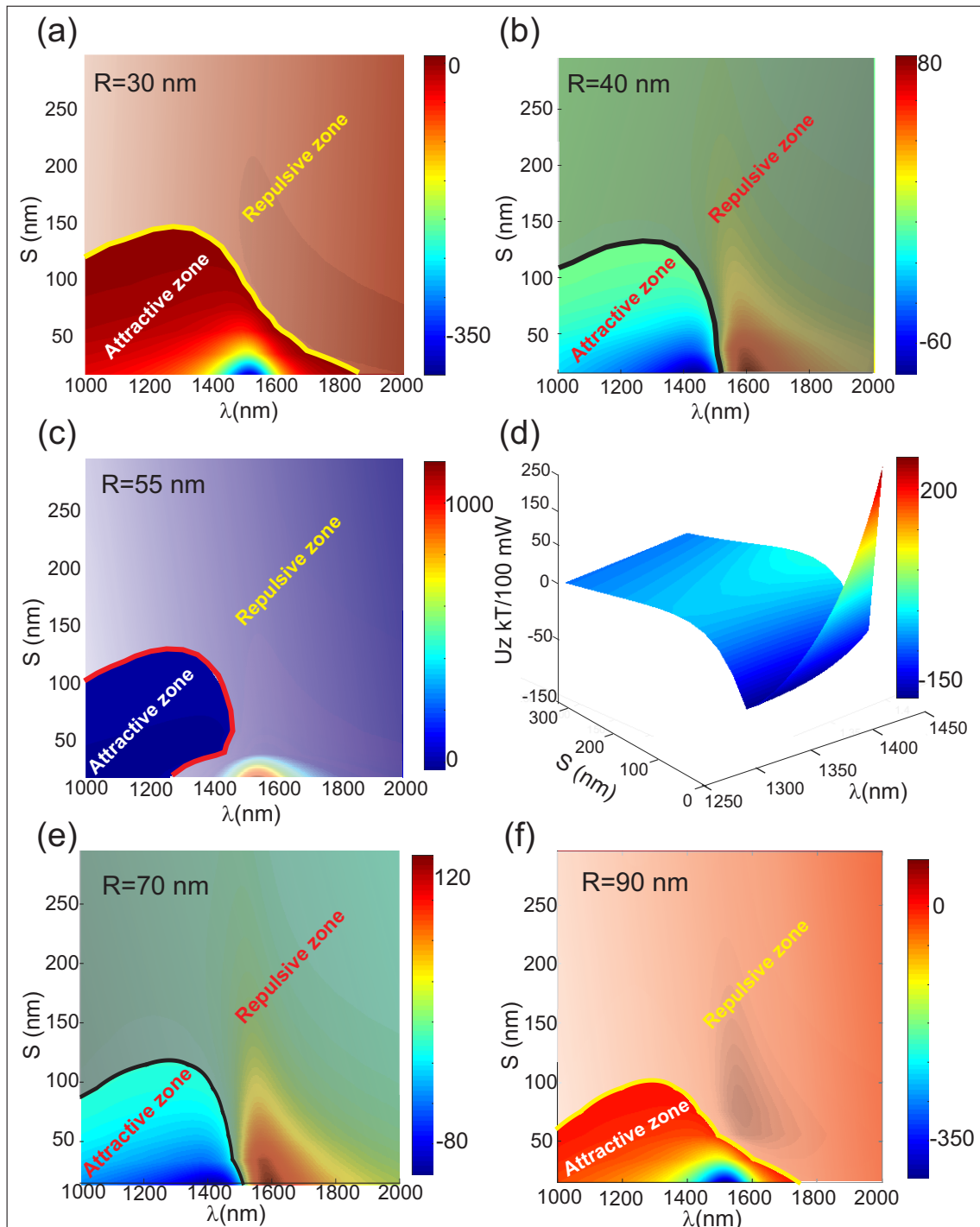


Figure 5.13: Map of vertical force numerical results presented as a function of the DA-to- N_p distance S and the wavelength illuminations λ for different N_p radius: a) $R=30$ nm. b) $R=40$ nm. c) $R=55$ nm. e) $R=70$ nm. f) $R=90$ nm. d) Show the potential well of N_p with $R=55$ nm.

If we increase the radius value to $R=40\text{nm}$, the attractive zone becomes limited to wavelengths smaller than λ_{res} . In fact, as shown on figure 5.13 b, F_z vanishes at resonance. This can be due to the fact that the radiation pressure becomes larger while the gradient force is kept the same. According to figures 5.9 a and b, the trapping is then induced by the magnetic field confinement that occurs at the DA center. For $R=55\text{ nm}$ (see figure 5.13 c), a very interesting phenomenon appears for $\lambda \in [1300; 1470]\text{ nm}$ where the attractive zone is surrounded by a repulsive one when S increases. This means that a stable trapping can be obtained without contact. Figure 5.13 d presents the potential corresponding to figure 5.13 c where a potential well ($U = -150\text{kT}/100\text{ mW}$) is obtained only for small values of S . We have verified that this trapping at distance phenomenon is also obtained for $R \in [50, 65]\text{ nm}$ but for different wavelength intervals as it will be shown in the following. When the Np radius increases (see figures 5.13 e and f), the attractive zone shifts toward larger values of the wavelength due to the efficient overlap between the Np and the electric field of the DA generated at its corners. By the way, another value of R exists for which the vertical force vanishes at resonance (here $R=70\text{ nm}$ as seen on figure 5.13 e).

In figure 5.14, four values of the DA-to-Np distance are considered: $S=15, 55, 95$ and 155 nm . For $S=15\text{nm}$, figure 5.14 a shows that attractive force occurs at small distance S for all Np radius and small values of the wavelength $\lambda \in [1000, 1800]\text{nm}$. The attractive zone and repulsive zone are separated by the red line. When we increase the distance S from 55nm to 95nm , the attractive zone becomes smaller and it is globally blue-shifted as shown on figures 5.14 b and c. The maximum of the repulsive force always appears at the resonance wavelength due to the funnel effect (see figure 5.14 c) induced by the DA and leading to an increase of the radiation pressure on the Np. For larger distance values $S (>155\text{nm})$ the attractive zone almost vanishes in the considered wavelength range and the Np is pushed away from the DA as shown in figures 5.14 d. This phenomena, as

expected, occurs as result of the background illumination.

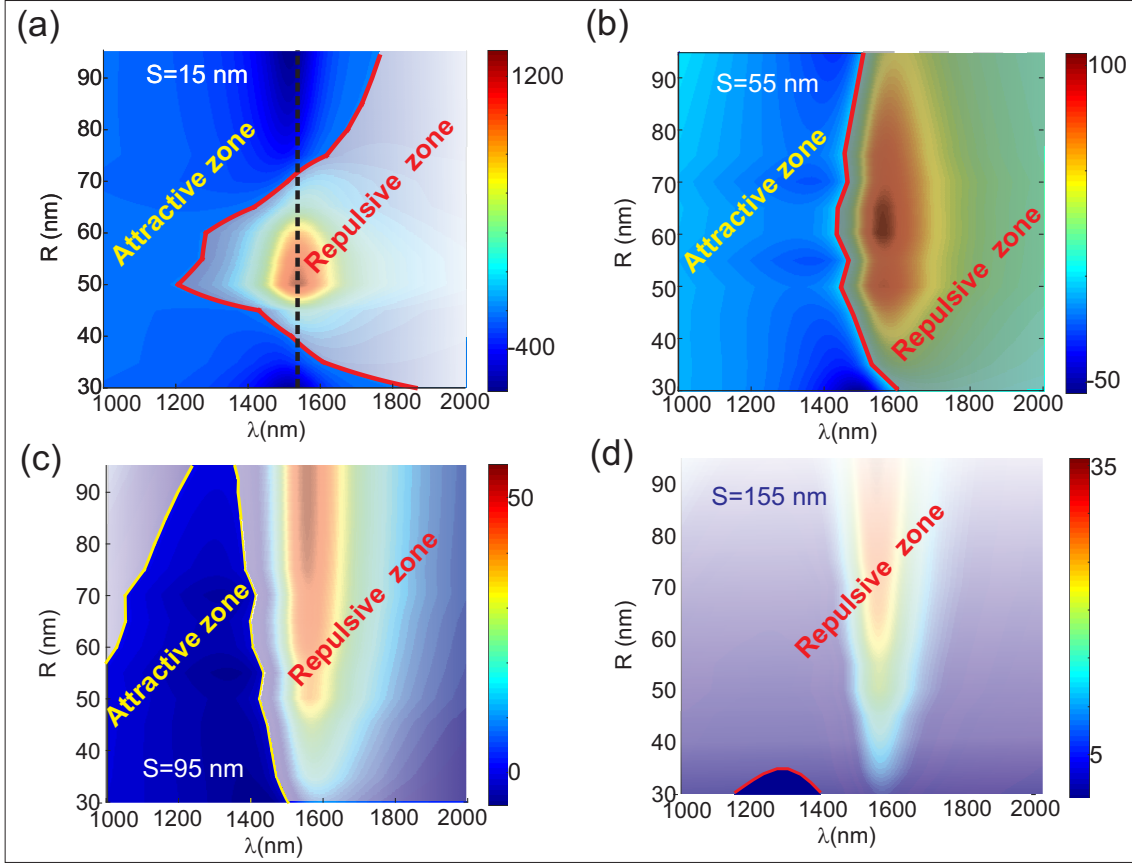


Figure 5.14: Map of vertical force numerical results presents as a function of the Np radius R and the wavelength illuminations λ for different DA-to-Np distance S : a) $S=15$. nm b) $S=55$. nm c) $S=95$. nm d) $S=155$ nm.

Experimentally, it is more adequate to set the operation wavelength and to see how the trapping can occur as a function of the Np radius. For this purpose, we present on figure 5.15 the variations of the vertical force for three different values of the wavelength when both R and S vary. Figure 5.15 a corresponds to a wavelength smaller than the resonance one. In this case, a stable trapping at distance (red solid line on figure 5.15 a) may occur for $R \in [50\text{nm}; 65\text{nm}]$ providing smaller initial DA-to-Np distance than 100nm. This can be ensured by increasing the concentration of Nps in the liquid.

At the RW, the repulsive zone spreads over almost the total window and two small

attractive areas remain for $R > 70\text{nm}$ and $R < 40\text{nm}$ only at $S < 90\text{ nm}$. At this peculiar wavelength, only trapping with contact may occur and Nps such $R \in [40, 70\text{nm}]$ are never trapped figure 5.15 b. This configuration can be exploited to make a Np sorting with respect to their dimension. For larger wavelength value (here $\lambda = 1800\text{nm}$), only repulsive zone exists due to the absence of any light confinement. The radiation pressure is then predominant and only pushing force acts on the Np as shown in figure 5.15c.

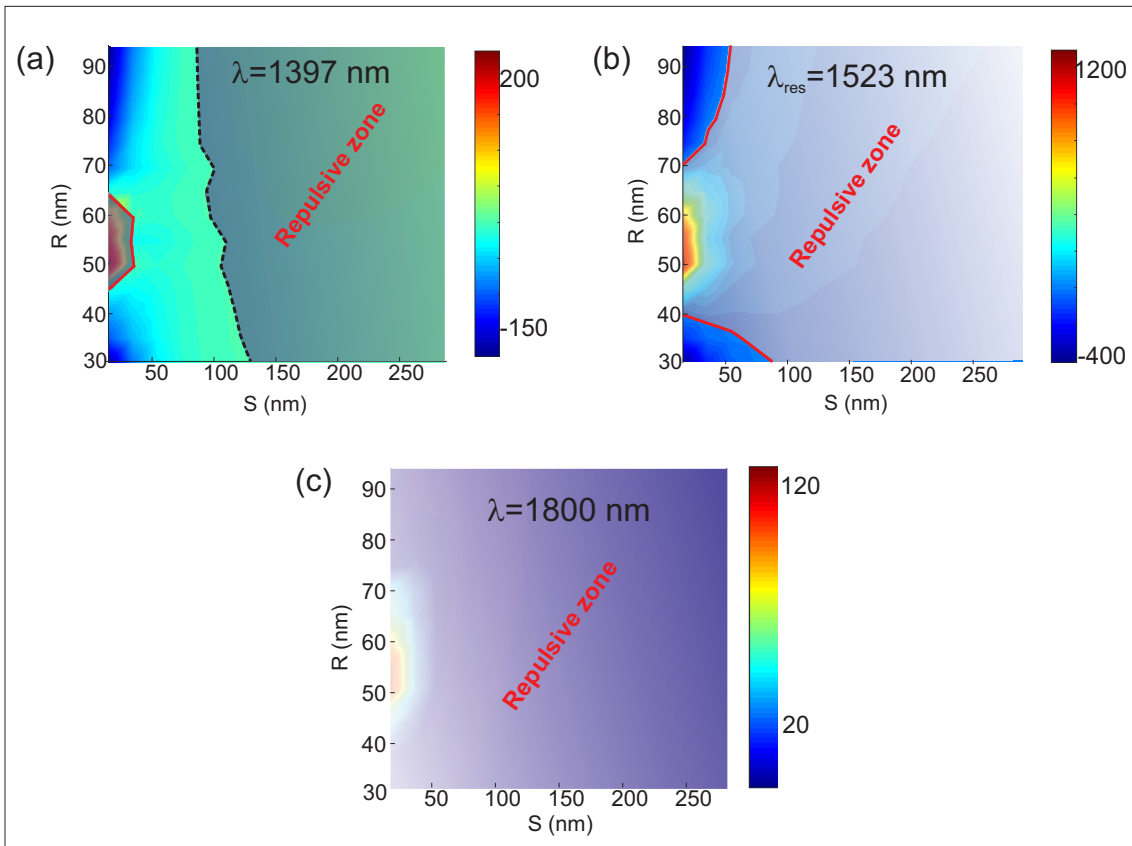


Figure 5.15: Map of vertical force numerical results presents as a function of Np radius and DA-to-Np distance S for different operation wavelengths: a) $\lambda = 1397\text{ nm}$ b) $\lambda_{res} = 1523\text{ nm}$ c) $\lambda = 1800\text{ nm}$.

To get more physical insight on the DA-Np interaction at the resonance wavelength, we plot on figure 5.16 a cross-section made on the result of along figure 5.14 a. This plot gives the optical force exerted on the Np as a function of its radius (R) when it is placed in front of a resonant DA (at $\lambda = 1523\text{ nm}$) and at a fixed distance $S = 15\text{ nm}$. This will

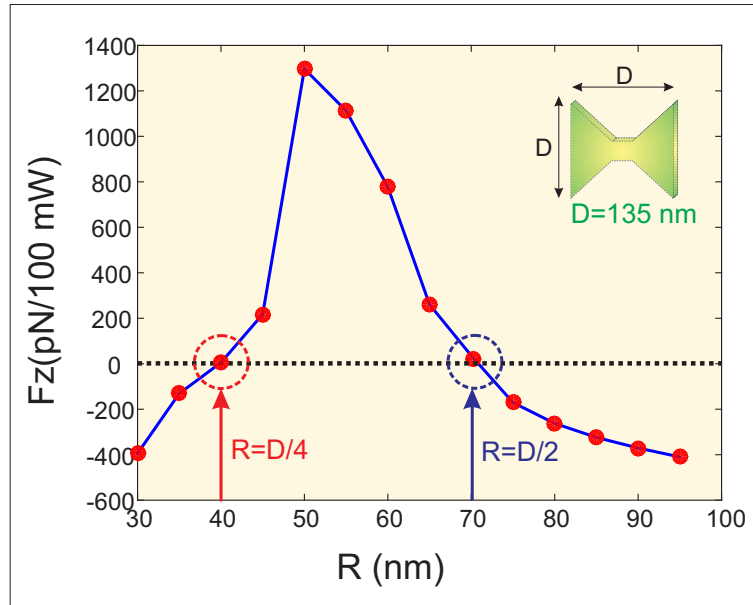


Figure 5.16: Numerical results of vertical force presents as a function of the size of the Np placed at 15 nm far from the DA along its axis. One notice that the permittivity of the Np is modeled with a subgridding technique in order to accurately describe its geometry.

give us the Np radius for which trapping occurs (corresponding to zero vertical force) at this specific distance. The first value ($R=40$ nm) almost corresponds to the quarter of DA length while the second ($R=70$ nm) is obtained for a Np size that almost corresponds to the DA one ($D = 135$ nm). These two values are indicated by red and blue arrows respectively in figure 5.16.

In order to point out a possible manipulation of a Np by a DA, we extract three different scenarios that correspond to (a) a pushing, (b) trapping at distance or (c) trapping at contact that can exist for a given Np (fixed R) only by changing the operation wavelength. Four values of the Np dimension are considered ($R=50, 55, 60$ et 65) in the range where trapping at distance can occur. As shown in figure 5.17 where the potential is plotted as a function of S , one can always find a wavelength value to induce each scenario. In all cases, the trapping at distance exhibits a potential well larger than $10kT$ providing an illumination power larger than 5 mw. The latter value correspond to the energy part

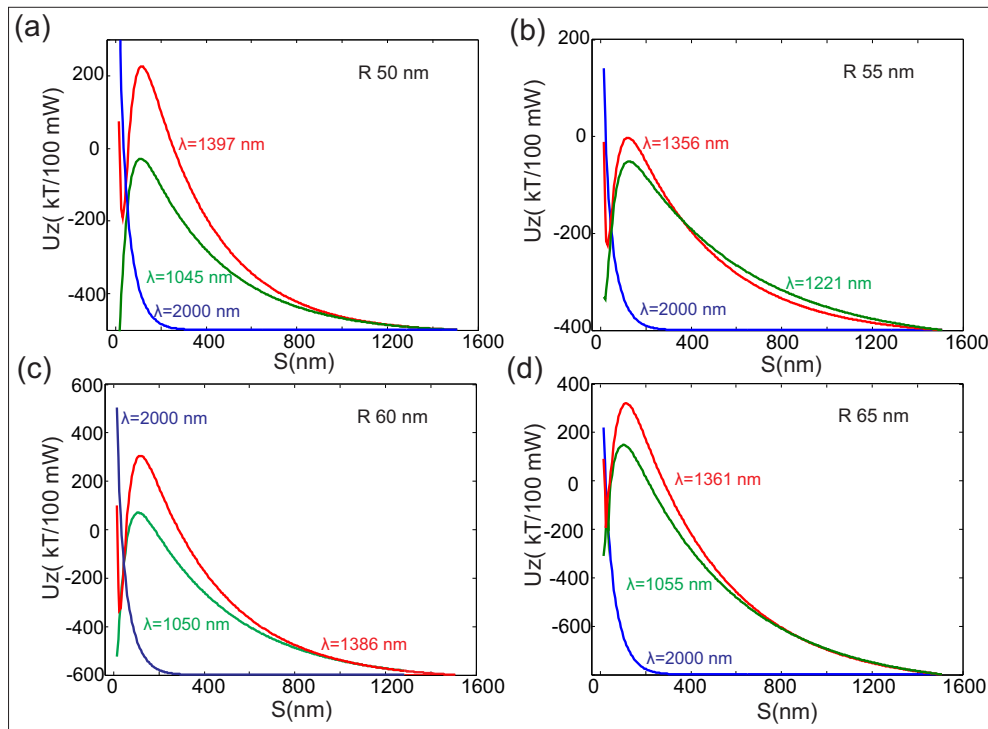


Figure 5.17: (a),(b),(c) and (d) The potential results of different Nps radii (50,55,60,65) nm shows three case of the optical trapping with different operation wavelength:1) Red solid lines are trapping at distance.2) Green solid lines are trapping at contact. 3) Blue solid lines are no trapping (radiation pressure).

that is incident on the DA. High focusing system will be probably required to fulfill this condition. In all figures, the red curves represent the trapping at distance process where a potential well exists for $S \neq 0$ while green curves represent the case of trapping with contact where the potential well occurs for $S < 15$ nm. Along this axis, there is no lateral components of the force and the vertical one is non zero. Where, this potential well value is sufficient to overcome of Brownian motion and trap NP at a distance as shown in figure 5.17. On the contrary, the blue curves correspond to wavelength values for which the NP is pushed away from the DA (no trapping).

5.5 Conclusion

In summary, we have theoretically and numerically studied the optical trapping of polystyrene Nps by using Diabolo nanoantenna (DA). This later show that this configuration is able to confine the two electromagnetic fields (electric and magmatic fields) with high factor of enhancement. Numerical simulations are performed to determine the mechanical interaction between the DA and a polystyrene Nps. Optical force exerted on the NP has been studied as a function of size, wavelength and distance. This study show the ability to trap small Nps with different cases: trapping at a distance, trapping at contact and trapping at resonance wavelength for small ($R < 40\text{nm}$) or big ($R > 70\text{nm}$) NPs. This study demonstrate that it is possible to manipulate NPs by simply changing the operation wavelength. The design of the DA can be optimized to fulfill the experimental constraints (sources and detectors) with respect to the NP dimension.

Chapter 6

General Conclusion and perspectives

This PhD work can be divided into two major parts dedicated to study some features of the interaction between electromagnetic waves and nanostructures.

In the first part, we implemented the Finite Difference Frequency Domain (FDFD) to calculate the eigenmodes of dielectric nanostructures. This method appears to be complementary to the already developed codes based on FDTD algorithm for the resolution of eigenproblems in electromagnetic wave. In fact, contrarily to the FDTD, it can handle any frequency dependent properties of materials such as dispersion and the simulations in frequency domain are faster when only responses for a few frequencies are required. Several tests were performed to validate our FDFD-matlab code by comparing with other published results. Exploitation of this code was done through the optimization of the design of waveguides exhibiting high confinement in the core such as slot waveguide or ridge waveguide. In addition, the FDFD algorithm is useful for the analysis of light behavior in PC (Photonic Crystal) structures. It is very easy to extend the code by including the periodic boundaries (Bloch-Floquet) conditions that can also be implemented in the derivative operators instead of Dirichlet or Neumann boundary conditions. But,

the simulation takes very long time in comparison with Plane Wave Expansion method (PWE) [16]. In fact, the band diagram is obtained by varying the wavevector along the edge of the first reduced Brillouin zone. Thus, for each propagation constant value that must correspond to the edge of the first reduced Brillouin zone, the CPU-time calculation exceeds 20 minutes so that a band diagram of only 100 points spends over more than 3 hours while the same band diagram is obtained in 15 seconds with the PWE.

The second part was devoted to the study of the optical forces exerted by nanostructures on nano-particles. This theoretical study was performed through a numerical code developed within our research team. This later is based on the resolution of Maxwell's equations by the method of finite differences in the time domain (FDTD). We have adapted the FDTD code to record all the electromagnetic fields components over the six faces of the box that enclosing the nanoparticle. We built a matlab-code to calculate the optical force through Maxwell's stress tensor. After validation of our code through some tests and comparison with published results, our first application addressed the modeling of experiments of optical trapping conducted by Ali El Eter and Thierry Grosjean from our research team. We modified our FDTD code to integrate the used configuration that is composed of a fibred optical tweezers based on the combination of a metal coated SNOM probe and a Bowtie Nanoaperture Antenna (BNA) engraved at its apex. Geometrical parameters of the BNA were optimized theoretically to get a resonance wavelength at $\lambda = 1064 \text{ nm}$. The same designed BNA tip was fabricated and used to trap polystyrene latex particles. Our theoretical results achieved good agreement with experimental one for the trapping of latex nanoparticle with radius $R = 250 \text{ nm}$ showing a potential well of $3 \text{ kT}/mW$. Supplementary numerical simulations were performed to investigate the ability of such configuration to smaller particles $R = 100, 30 \text{ nm}$. Obtained numerical results showed smaller potential well ($140\text{kT} /100 \text{ mW}$ and $47\text{kT}/100 \text{ mW}$) respectively meaning that higher power illuminations are needed.

The second application was dedicated to study other nanoantenna namely the metallic Diabolo nanoantenna (DA). This specific nanoantenna can exhibit large enhancement and confinement of both magnetic and electric near-fields. This doubly resonant structure opens the way for the design of a novel generation of efficient optical nano-tweezers. Through the same method as in the first application, we calculated the optical force exerted on small size nanoparticle. Two cases of resonant and non-resonant DA (according to the illumination polarization direction) were studied in order to point out the effect (enhancement) of the DA resonance on the radiation pressure exerted on the DA itself. This configuration showed the ability of nanoparticle manipulation. Furthermore, the obtained results showed that the trapping process greatly depends on the particle parameters (size, DA-to-particle distance, wavelength illumination). For specific geometries, we can get trapping without contact, trapping at contact or nanoparticle pushed away from the DA. The design of the DA can be optimized to fulfill the experimental constraints (sources and detectors) with respect to the nanoparticle dimension.

Perspectives: As it is common to all thesis in physics, the developed work is never completely finished and some perspectives should be considered. For example, the FDFD code that was exploited to calculate the properties of dielectric waveguides must be extended to the case of metallo-dielectric structures such as coaxial or plasmonic nano-waveguides [70, 102]. On the other hand, theoretical and experimental investigations should be performed to highlight and better understand the trapping of nanosized particles that is expected only under certain constraints (appropriate initial spatial position of the particle and substantial light power) without risking destruction of both nanoantenna and particle by optical heating for example. In addition, there is a very interesting challenging study of optical trapping of resonant (dielectric or metallic) particles. In this case, the coupling between the nanoantenna and the nanoparticle can not be neglected and resonance wavelength shift may occur affecting the trapping process. Different cou-

pling regimes can be studied according to the mismatching between the resonances of the nanoantenna and the nanoparticle. Experiments must also be done in parallel to valid the theoretical studies.

Bibliography

- [1] Zhaoming ZHU et Thomas BROWN : Full-vectorial finite-difference analysis of microstructured optical fibers. *Opt. Express*, 10(17):853–864, Aug 2002.
 - [2] A. ASHKIN, J. M. DZIEDZIC, J. E. BJORKHOLM et Steven CHU : Observation of a single-beam gradient force optical trap for dielectric particles. *Opt. Lett.*, 11(5):288 – 290, May 1986.
 - [3] Patrick C. CHAUMET, Adel RAHMANI et Manuel NIETO-VESPERINAS : Optical trapping and manipulation of nano-objects with an apertureless probe. *Phys. Rev. Lett.*, 88:123601, Mar 2002.
 - [4] Lukas NOVOTNY, Randy X. BIAN et X. Sunney XIE : Theory of nanometric optical tweezers. *Phys. Rev. Lett.*, 79:645 – 648, Jul 1997.
 - [5] Amr A. E. SALEH et Jennifer A. DIONNE : Toward efficient optical trapping of sub-10-nm particles with coaxial plasmonic apertures. *Nano Lett.*, 12:5581 – 5586, 2012.
 - [6] Yuanjie PANG et Reuven GORDON : Optical trapping of 12 nm dielectric spheres using double-nanoholes in a gold film. *Nano Letters*, 11(9):3763–3767, 2011. PMID: 21838243.
-

-
- [7] J. BERTHELOT, S. S. Aćimovi, M. L. JUAN, M. P. KREUZER, J. RENGER et R. QUIDANT : Three-dimensional manipulation with scanning near-field optical nanotweezers. *Nature Nanotechnology*, 9:295 – 299, 2014.
- [8] Ali ELETER, Nyha M. HAMEED, Fadi I. BAIDA, Roland SALUT, Claudine FILIATRE, Dusan NEDELJKOVIC, Elie ATIE, Samuel BOLE et Thierry GROSJEAN : Fiber-integrated optical nano-tweezer based on a bowtie-aperture nano-antenna at the apex of a snom tip. *Opt. Express*, 22(8):10072 – 10080, Apr 2014.
- [9] Yoshito TANAKA et Keiji SASAKI : Optical trapping through the localized surface-plasmon resonance of engineered gold nanoblock pairs. *Opt. Express*, 19(18):17462–17468, Aug 2011.
- [10] L. NOVOTNY et B. HECHT : *Principles of nano-optics*. Cambridge University Press, 2006.
- [11] W. QIU, M.-P. BERNAL, A. NDAO, C. GUYOT, N.M. HAMEED, N. COURJAL, H. MAILLOTTE et F.I. BAIDA : Analysis of ultra-compact waveguide modes in thin film lithium niobate. *Applied Physics B*, 118(2):261–267, 2015.
- [12] Zhaoming ZHU et Thomas G. BROWN : Multipole analysis of hole-assisted optical fibers. *Optics Communications*, 206(4?6):333 – 339, 2002.
- [13] Y. Q. YE et Y. JIN : Enhanced transmission of transverse electric waves through subwavelength slits in a thin metallic film. *Phys. Rev. E*, 80:036606, 2009.
- [14] T. ANDO, H. NAKAYAMA, S. NUMATA, J. YAMAUCHI et H. NAKANO : Eigenmode analysis of optical waveguides by a yee-mesh-based imaginary-distance propagation method for an arbitrary dielectric interface. *Lightwave Technology, Journal of*, 20(8):1627–1634, Aug 2002.
-

-
- [15] Shangping GUO, Feng WU, Sacharia ALBIN, Hsiang TAI et Robert ROGOWSKI : Loss and dispersion analysis of microstructured fibers by finite-difference method. *Opt. Express*, 12(15):3341–3352, Jul 2004.
- [16] John D. JOANNOPOULOS, Steven G. JOHNSON, Joshua N. WINN et Robert D. MEADE : *Photonic Crystals: Molding the Flow of Light. second edition.* 2008.
- [17] Shangping GUO, Feng WU, Sacharia ALBIN et Robert ROGOWSKI : Photonic band gap analysis using finite-difference frequency-domain method. *Opt. Express*, 12(8):1741–1746, Apr 2004.
- [18] A. CHRIST et Hans L. HARTNAGEL : Three-dimensional finite-difference method for the analysis of microwave-device embedding. *Microwave Theory and Techniques, IEEE Transactions on*, 35(8):688–696, Aug 1987.
- [19] K. BIERWIRTH, N. SCHULZ et F. ARNDT : Finite-difference analysis of rectangular dielectric waveguide structures. *IEEE Transactions on Microwave Theory and Techniques*, 34(11):1104–1114, Nov 1986.
- [20] N. SCHULZ, K. BIERWIRTH, F. ARNDT et U. KOSTER : Finite-difference method without spurious solutions for the hybrid-mode analysis of diffused channel waveguides. *IEEE Transactions on Microwave Theory and Techniques*, 38(6):722–729, Jun 1990.
- [21] Man-Leung LUI et Zhizhang CHEN : A direct computation of propagation constant using compact 2-d full-wave eigen-based finite-difference frequency-domain technique. In *Computational Electromagnetics and Its Applications, 1999. Proceedings. (ICCEA '99) 1999 International Conference on*, pages 78–81, 1999.
-

- [22] Y.Z. HE et F.G. SHI : Finite-difference imaginary-distance beam propagation method for modeling of the fundamental mode of photonic crystal fibers. *Optics Communications*, 225(13):151 – 156, 2003.
- [23] Vilson R. ALMEIDA, Qianfan XU, Carlos A. BARRIOS et Michal LIPSON : Guiding and confining light in void nanostructure. *Opt. Lett.*, 29(11):1209 – 1211, Jun 2004.
- [24] Shun-Der WU et Elias N. GLYTSIS : Volume holographic grating couplers: rigorous analysis by use of the finite-difference frequency-domain method. *Appl. Opt.*, 43(5): 1009–1023, Feb 2004.
- [25] Yen-Chung CHIANG, Yih-Peng CHIOU et Hung chun CHANG : Finite-difference frequency-domain analysis of 2-d photonic crystals with curved dielectric interfaces. *Lightwave Technology, Journal of*, 26(8):971–976, April 2008.
- [26] Yen-Chung CHIANG, Yih-Peng CHIOU et Hung-Chun CHANG : Improved full-vectorial finite-difference mode solver for optical waveguides with step-index profiles. *Lightwave Technology, Journal of*, 20(8):1609–1618, Aug 2002.
- [27] Shun-Der WU et Elias N. GLYTSIS : Finite-number-of-periods holographic gratings with finite-width incident beams: analysis using the finite-difference frequency-domain method. *J. Opt. Soc. Am. A*, 19(10):2018–2029, Oct 2002.
- [28] G.R. HADLEY : High-accuracy finite-difference equations for dielectric waveguide analysis i: uniform regions and dielectric interfaces. *Lightwave Technology, Journal of*, 20(7):1210–1218, Jul 2002.
- [29] Yinchao CHEN, Kunquan SUN, B. BEKER et R. MITTRA : Unified matrix presentation of maxwell's and wave equations using generalized differential matrix operators [em engineering education]. *Education, IEEE Transactions on*, 41(1):61–69, Feb 1998.
-

-
- [30] Weng Cho CHEW et William H. WEEDON : A 3d perfectly matched medium from modified maxwell's equations with stretched coordinates. *Microwave and Optical Technology Letters*, 7(13):599–604, 1994.
- [31] Yih-Peng CHIOU, Yen-Chung CHIANG et Hung-Chun CHANG : Improved three-point formulas considering the interface conditions in the finite-difference analysis of step-index optical devices. *Lightwave Technology, Journal of*, 18(2):243–251, Feb 2000.
- [32] Ronald W. GAMACHE, Carey RAPPAPORT et Mohammad FARID : "a comparison of fdfd and fem methods applied to the buried mine problem". In *Excerpt from the Proceedings of the COMSOL Users Conference 2006 Boston*, 2006.
- [33] Elsie BARAKAT, Maria-Pilar BERNAL et Fadi Issam BAIDA : Theoretical analysis of enhanced nonlinear conversion from metallo-dielectric nano-structures. *Opt. Express*, 20(15):16258–16268, Jul 2012.
- [34] Kane YEE : Numerical solution of initial boundary value problems involving maxwell's equations in isotropic media. *Antennas and Propagation, IEEE Transactions on*, 14(3):302–307, May 1966.
- [35] Umran S. INAN et Robert A. MARSHALL : *Numerical Electromagnetics The FDTD Method*. Cambridge University Press, 2011.
- [36] P. LUSSE, P. STUWE, J. SCHULE et H-G UNGER : Analysis of vectorial mode fields in optical waveguides by a new finite difference method. *Lightwave Technology, Journal of*, 12(3):487–494, Mar 1994.
- [37] Clément GUYOT, Gwenn ULLIAC, Jean DAHDAH, Wentao QIU, Maria-Pilar BERNAL, Fadi BAIDA et Nadège COURJAL : Optical characterization of ultra-
-

-
- short bragg grating on lithium niobate ridge waveguide. *Opt. Lett.*, 39(2):371–374, Jan 2014.
- [38] Qianfan XU, Vilson R. ALMEIDA, Roberto R. PANEPUCCI et Michal LIPSON : Experimental demonstration of guiding and confining light in nanometer-size low-refractive-index material. *Opt. Lett.*, 29(14):1626–1628, Jul 2004.
- [39] WWW.NANOLN.COM.
- [40] Nadège COURJAL, Blandine GUICHARDAZ, Gwenn ULLIAC, Jean-Yves RAUCH, Benattou SADANI, Hui-Hui LU et Maria-Pilar BERNAL : High aspect ratio lithium niobate ridge waveguides fabricated by optical grade dicing. *Journal of Physics D: Applied Physics*, 44(30):305101, 2011.
- [41] P.N. LEBEDEV : The experimental study of the pressure of the light. *Annalen der Physik*, 6:433, 1901.
- [42] Jiunn-Nan HWANG : A compact 2-d fdtd method for modeling microstrip structures with nonuniform grids and perfectly matched layer. *Microwave Theory and Techniques, IEEE Transactions on*, 53(2):653–659, Feb 2005.
- [43] E. F. NICHOLS et G. F. HULL : The pressure due to radiation. *Astrophysical Journal*, 17:315, 1903.
- [44] A. ASHKIN : Acceleration and trapping of particles by radiation pressure. *Phys. Rev. Lett.*, 24:156 – 159, Jan 1970.
- [45] A. ASHKIN et J. M. DZIEDZIC : Optical levitation by radiation pressure. *Applied Physics Letters*, 19(8):283–285, 1971.
- [46] A. ASHKIN : Forces of a single-beam gradient laser trap on a dielectric sphere in the ray optics regime. *Biophysical Journal*, 61(2):569 – 582, 1992.
-

-
- [47] Keir C. NEUMAN et Steven M. BLOCK : Optical trapping. *Review of Scientific Instruments*, 75(9):2787–2809, 2004.
- [48] Alexander JESACHER, Severin FÜRHAPTER, Stefan BERNET et Monika RITSCHMARTE : Diffractive optical tweezers in the fresnel regime. *Opt. Express*, 12(10):2243–2250, May 2004.
- [49] Francesca ANSELMINI, Cathie VENTALON, Aurélien BÈGUE, David OGDEN et Valentina EMILIANI : Three-dimensional imaging and photostimulation by remote-focusing and holographic light patterning. *Proceedings of the National Academy of Sciences*, 108(49):19504–19509, 2011.
- [50] A. CONSTABLE, Jinha KIM, J. MERVIS, F. ZARINETCHI et M. PRENTISS : Demonstration of a fiber-optical light-force trap. *Opt. Lett.*, 18(21):1867 – 1869, Nov 1993.
- [51] T-P. VO, M. MIVELLE, S. CALLARD, A. RAHMANI, F. BAIDA, D. CHARRAUT, A. BELAROUCI, D. NEDELJKOVIC, C. SEASSAL, G.W. BURR et T. GROSJEAN : Near-field probing of slow bloch modes on photonic crystals with a nanoantenna. *Opt. Express*, 20(4):4124 – 4135, Feb 2012.
- [52] Giorgio VOLPE, Monika NOACK, Srdjan S. AĆIMOVIĆ, Carsten REINHARDT et Romain QUIDANT : Near-field mapping of plasmonic antennas by multiphoton absorption in poly(methyl methacrylate). *Nano Letters*, 12(9):4864–4868, 2012. PMID: 22894567.
- [53] K. OKAMOTO et S. KAWATA : Radiation force exerted on subwavelength particles near a nanoaperture. *Phys. Rev. Lett.*, 83:4534 – 4537, Nov 1999.
- [54] Ursula SCHRÖTER et Alain DEREUX : Surface plasmon polaritons on metal cylinders with dielectric core. *Phys. Rev. B*, 64:125420, Sep 2001.
-

-
- [55] P. J. SCHUCK, D. P. FROMM, A. SUNDARAMURTHY, G. S. KINO et W. E. MOERNER : Improving the mismatch between light and nanoscale objects with gold bowtie nanoantennas. *Phys. Rev. Lett.*, 94:017402, Jan 2005.
- [56] Daniel COURJON et Claudine BAINIER : *Le champ proche optique: théorie et applications*. 2001.
- [57] J. GUCK, R. ANANTHAKRISHNAN, H. MAHMOOD, T. J. MOON, C. C. CUNNINGHAM et J. KAS : optical stretcher: A novel laser tool to micromanipulate cells. *Biophysical Journal*, 81:767 – 784, 2001.
- [58] D. G. GRIER : A revolution in optical manipulation. *Nature*, 424:810 – 816, 2003.
- [59] Giovanni VOLPE, Romain QUIDANT, Gon çal BADENES et Dmitri PETROV : Surface plasmon radiation forces. *Phys. Rev. Lett.*, 96:238101, Jun 2006.
- [60] A. N. GRIGORENKO, N. W. ROBERTS, M. R. DICKINSON et Y. ZHANG : Nanometric optical tweezers based on nanostructured substrates. *Nature Photonics*, 2:365 – 370, 2008.
- [61] Allen H. J. YANG, Sean D. MOORE, Bradley S. SCHMIDT, Matthew KLUG, Michal LIPSON et David ERICKSON : Optical manipulation of nanoparticles and biomolecules in sub-wavelength slot waveguides. *Nature*, 457:71 – 75, 2009.
- [62] Fan WANG, Wen Jun TOE, Woei Ming LEE, David MCGLOIN, Qiang GAO, Hark Hoe TAN, Chennupati JAGADISH et Peter J. REECE : Resolving stable axial trapping points of nanowires in an optical tweezers using photoluminescence mapping. *Nano Lett.*, 12:5581 ? 5586, 2013.
- [63] Hongbao XIN, Yayi LI, Lingshan LI, Rui XU et Baojun LI : Optofluidic manipulation of escherichia coli in a microfluidic channel using an abruptly tapered optical fiber. *Applied Physics Letters*, 103(3):–, 2013.
-

-
- [64] F. J. VALDIVIA-VALERO et M. NIETO-VESPERINAS : Optical forces on cylinders near subwavelength slits: effects of extraordinary transmission and excitation of mie resonances. *Opt. Express*, 20(12):13368 – 13389, Jun 2012.
- [65] Francisco Javier Valdivia VALERO et Manuel Nieto VESPERINAS : Optical forces on resonant metallic cylinders near supertransmitting slits illuminated by a photonic nanojet. *American Insitute of Physics*, 1475:176, 2012.
- [66] Charithra RAJAPAKSE, Fan WANG, Tiffany C. Y. TANG, Peter J. REECE, Sergio G. LEON-SAVAL et Alexander ARGYROS : Spectroscopy of 3d-trapped particles inside a hollow-core microstructured optical fiber. *Opt. Express*, 20(10):11232 – 11240, May 2012.
- [67] Jean-Baptiste DECOMBE, Serge HUANT et Jochen FICK : Single and dual fiber nano-tip optical tweezers: trapping and analysis. *Opt. Express*, 21:30521, 2013.
- [68] P.M. BENDIX, L. JAUFFRED, K. NORREGAARD et L.B. ODDERSHEDE : Optical trapping of nanoparticles and quantum dots. *Selected Topics in Quantum Electronics, IEEE Journal of*, 20(3):15–26, May 2014.
- [69] TAFLOVE : *The Finite-Difference Time-Domain Method*. Norwood, MA: Artech House, 1995.
- [70] F.I. BAIDA et D. Van LABEKE : Light transmission by subwavelength annular aperture arrays in metallic films. *Optics Communications*, 209(1?3):17 – 22, 2002.
- [71] Dianwen ZHANG, X. YUAN, S. TJIN et S. KRISHNAN : Rigorous time domain simulation of momentum transfer between light and microscopic particles in optical trapping. *Opt. Express*, 12(10):2220 – 2230, May 2004.
- [72] Robert GAUTHIER : Computation of the optical trapping force using an fdtd based technique. *Opt. Express*, 13(10):3707 – 3718, May 2005.
-

-
- [73] Armis ZAKHARIAN, Masud MANSURIPUR et Jerome MOLONEY : Radiation pressure and the distribution of electromagnetic force in dielectric media. *Opt. Express*, 13(7):2321 – 2336, Apr 2005.
- [74] Yasuhiro HARADA et Toshimitsu ASAKURA : Radiation forces on a dielectric sphere in the rayleigh scattering regime. *Optics Communications*, 124(5?6):529 – 541, 1996.
- [75] Zhirong LIU et Daomu ZHAO : Radiation forces acting on a rayleigh dielectric sphere produced by highly focused elegant hermite-cosine-gaussian beams. *Opt. Express*, 20(3):2895–2904, Jan 2012.
- [76] R. COURANT, K. FRIEDRICHS et H. LEWY : On the partial difference equations of mathematical physics. *IBM J. Res. Dev.*, 11(2):215–234, mars 1967.
- [77] A. TAFLOVE et S. C. HAGNESS : *Computational Electrodynamics, the Finite-Difference TimeDomain Method*. Artech House, Norwood, MA, second edition édition, 2005.
- [78] Charles KITTEL : *Introduction to solid state physics*. John Wiley & Sons, Inc, 7th edition édition, 2005.
- [79] David F. EDWARDS : *Handbook of Optical Constants of Solids*. Academic Press, Burlington, 1997.
- [80] R. HOLLAND : Threde: A free-field emp coupling and scattering code. *Nuclear Science, IEEE Transactions on*, 24(6):2416–2421, Dec 1977.
- [81] Alvin BAYLISS et Eli TURKEL : Radiation boundary conditions for wave-like equations. *Communications on Pure and Applied Mathematics*, 33(6):707–725, 1980.
- [82] Bjorn ENGQUIST et Andrew MAJDA : Absorbing boundary conditions for numerical simulation of waves. *Proceedings of the National Academy of Sciences*, 74(5):1765–1766, 1977.
-

-
- [83] Gerrit MUR : Absorbing boundary conditions for the finite-difference approximation of the time-domain electromagnetic-field equations. *Electromagnetic Compatibility, IEEE Transactions on*, EMC-23(4):377–382, Nov 1981.
- [84] Lloyd N TREFETHEN et Laurence HALPERN : Well-posedness of one-way wave equations and absorbing boundary conditions. *Math. Comput.*, 47(176):421–435, octobre 1986.
- [85] Robert L HIGDON : Absorbing boundary conditions for difference approximations to the multi-dimensional wave equation. *Math. Comput.*, 47(176):437–459, octobre 1986.
- [86] K.K. MEI et Jiayuan FANG : Superabsorption-a method to improve absorbing boundary conditions [electromagnetic waves]. *Antennas and Propagation, IEEE Transactions on*, 40(9):1001–1010, Sep 1992.
- [87] LIAO Zhen FENG, HUANG Kong LIANG, YANG Bai PO et YUAN Yi FAN : A transmitting boundary for transient wave analyses. *SCIENCE CHINA Mathematics*, 27(10):1063, 1984.
- [88] Jean-Pierre BERENGER : A perfectly matched layer for the absorption of electromagnetic waves. *Journal of Computational Physics*, 114(2):185 – 200, 1994.
- [89] Maurizio RIGHINI, Giovanni VOLPE, Christian GIRARD, Dmitri PETROV et Romain QUIDANT : Surface plasmon optical tweezers: Tunable optical manipulation in the femtonewton range. *Phys. Rev. Lett.*, 100:186804, May 2008.
- [90] Kai WANG, Ethan SCHONBRUN, Paul STEINVURZEL et Kenneth B. CROZIER : Scannable plasmonic trapping using a gold stripe. *Nano Letters*, 10(9):3506–3511, 2010. PMID: 20715811.
-

- [91] Zhihai LIU, Chengkai GUO, Jun YANG et Libo YUAN : Tapered fiber optical tweezers for microscopic particle trapping: fabrication and application. *Opt. Express*, 14(25):12510–12516, Dec 2006.
- [92] Carlo LIBERALE, Paolo MINZIONI, Francesca BRAGHERI, Francesco De ANGELIS, Enzo Di FABRIZIO et Ilaria CRISTIANI : Miniaturized all-fibre probe for three-dimensional optical trapping and manipulation. *Nature Photonics*, 1(12):723 – 727, 2007.
- [93] Samir K. MONDAL, Sudipta Sarkar PAL et Pawan KAPUR : Optical fiber nano-tip and 3d bottle beam as non-plasmonic optical tweezers. *Opt. Express*, 20(15):16180–16185, Jul 2012.
- [94] Yuxiang LIU, Felix STIEF et Miao YU : Subwavelength optical trapping with a fiber-based surface plasmonic lens. *Opt. Lett.*, 38(5):721–723, Mar 2013.
- [95] Mathieu MIVELLE, Pierre VIKTOROVITCH, Fadi I. BAIDA, Ali El ETER, Zhihua XIE, Than-Phong VO, Elie ATIE, Geoffrey W. BURR, Dusan NEDELJKOVIC, Jean-Yves RAUCH, Ségolène CALLARD et Thierry GROSJEAN : Light funneling from a photonic crystal laser cavity to a nano-antenna: overcoming the diffraction limit in optical energy transfer down to the nanoscale. *Opt. Express*, 22(12):15075–15087, Jun 2014.
- [96] M. MIVELLE, I. A. IBRAHIM, F. BAIDA, G. W. BURR, D. NEDELJKOVIC, D. CHARRAUT, J-Y. RAUCH, R. SALUT et T. GROSJEAN : Bowtie nano-aperture as interface between near-fields and a single-mode fiber. *Opt. Express*, 18(15):15964 – 15974, Jul 2010.
- [97] I. A. IBRAHIM, M. MIVELLE, T. GROSJEAN, J.-T. ALLEGRE, G. W. BURR et F. I. BAIDA : Bowtie-shaped nanoaperture: a modal study. *Opt. Lett.*, 35(14):2448 – 2450, Jul 2010.
-

-
- [98] Renaud BACHELOT, Carole ECOFFET, Denis DELOEIL, Pascal ROYER et Daniel-Joseph LOUGNOT : Integration of micrometer-sized polymer elements at the end of optical fibers by free-radical photopolymerization. *Appl. Opt.*, 40(32):5860 – 5871, Nov 2001.
- [99] Eric X. JIN et Xianfan XU : Obtaining super resolution light spot using surface plasmon assisted sharp ridge nanoaperture. *Applied Physics Letters*, 86(11):–, 2005.
- [100] C FILIÂTRE, C PIGNOLET, A FOISSY, M ZEMBALA et P WARSZYŃSKI : Electrodeposition of particles at nickel electrode surface in a laminar flow cell. *Colloids and Surfaces A: Physicochemical and Engineering Aspects*, 222(1â3):55 – 63, 2003. A collection of papers presented at the International Symposium on Electrokinetic Phenomena, Cracow, Poland, August 18-22, 2003.
- [101] Weihua ZHANG, Lina HUANG, Christian SANTSCHI et Olivier J. F. MARTIN : Three-dimensional subgidding algorithm for fdtd. *IEEE, Trans. Ant. and Propagat.*, 45:422429, 1997.
- [102] F. I. BAIDA, A. BELKHIR, D. VAN LABEKE et O. LAMROUS : Subwavelength metallic coaxial waveguides in the optical range: Role of the plasmonic modes. *Phys. Rev. B*, 74:205419, Nov 2006.
- [103] M.A. SUAREZ, T. GROSJEAN, D. CHARRAUT et D. COURJON : Nanoring as a magnetic or electric field sensitive nano-antenna for near-field optics applications. *Optics Communications*, 270(2):447 – 454, 2007.
- [104] Dongxing WANG, Tian YANG et Kenneth B. CROZIER : Charge and current reservoirs for electric and magnetic field enhancement. *Opt. Express*, 18(10):10388–10394, May 2010.
-

-
- [105] T. GROSJEAN, M. MIVELLE, F. I. BAIDA, G. W. BURR et U. C. FISCHER : Diabolo nanoantenna for enhancing and confining the magnetic optical field. *Nano Letters*, 11(3):1009–1013, 2011. PMID: 21319837.
- [106] J. ZHOU, Th. KOSCHNY, M. KAFESAKI, E. N. ECONOMOU, J. B. PENDRY et C. M. SOUKOULIS : Saturation of the magnetic response of split-ring resonators at optical frequencies. *Phys. Rev. Lett.*, 95:223902, Nov 2005.
- [107] Robert D. GROBER, Robert J. SCHOELKOPF et Daniel E. PROBER : Optical antenna: Towards a unity efficiency near-field optical probe. *Applied Physics Letters*, 70(11):1354–1356, 1997.
- [108] Eric X. JIN et Xianfan XU : Enhanced optical near field from a bowtie aperture. *Applied Physics Letters*, 88(15):–, 2006.
- [109] BORN et E. WOLF : *Principles of Optics*. Cambridge University Press, 2002.
- [110] Patrick C. CHAUMET, Adel RAHMANI, Anne SENTENAC et Garnett W. BRYANT : Efficient computation of optical forces with the coupled dipole method. *Phys. Rev. E*, 72:046708, Oct 2005.
- [111] T. ZENTGRAF, T. P. MEYRATH, A. SEIDEL, S. KAISER, H. GIESSEN, C. ROCKSTUHL et F. LEDERER : Babinet’s principle for optical frequency metamaterials and nanoantennas. *Phys. Rev. B*, 76:033407, Jul 2007.
- [112] Ju-Hyung KANG, Kipom KIM, Ho-Seok EE, Yong-Hee LEE, Tae-Young YOON, Min-Kyo SEO et Hong-Gyu PARK : Low-power nano-optical vortex trapping via plasmonic diabolo nanoantennas. *Nature communications*, 2011.
- [113] Weihua ZHANG, Lina HUANG, Christian SANTSCHI et Olivier J. F. MARTIN : Trapping and sensing 10 nm metal nanoparticles using plasmonic dipole antennas. *Nano Letters*, 10(3):1006–1011, 2010. PMID: 20151698.
-

-
- [114] Lin JIA et Edwin L. THOMAS : Optical forces and optical torques on various materials arising from optical lattices in the lorentz-mie regime. *Phys. Rev. B*, 84:125128, Sep 2011.
- [115] Jacques BABINET : Memoires d'optique météorologique. *C.R., Acad. Sci., Paris*, 4:638–648, 1837.
- [116] Jörg P. KOTTMANN, Olivier J.F. MARTIN, David R. SMITH et Sheldon SCHULTZ : Spectral response of plasmon resonant nanoparticles with a non-regular shape. *Opt. Express*, 6(11):213–219, May 2000.
- [117] A. J. BABADJANYAN, N. L. MARGARYAN et Kh. V. NERKARARYAN : Superfocusing of surface polaritons in the conical structure. *Journal of Applied Physics*, 87(8): 3785–3788, 2000.
- [118] Elie M. ATIE, Tony TANNOUS, Thierry GROSJEAN et Fadi I BAIDA : High optical resonance sensitivity to its environment of a fibered bowtie nano-aperture antenna. *Applied Physics B*, 120(4), july 2015.
- [119] Elie M. ATIE, Zhihua XIE, Ali El ETER, Roland SALUT, Dusan NEDELJKOVIC, Tony TANNOUS, Fadi I. BAIDA et Thierry GROSJEAN : Remote optical sensing on the nanometer scale with a bowtie aperture nano-antenna on a fiber tip of scanning near-field optical microscopy. *Applied Physics Letters*, 106(15), April 2015.
-

Résumé :

Cette thèse constitue un ensemble de travaux et de réflexions sur la question de la modélisation d'expériences en nano-optique utilisant la méthode des différences finies dans le domaine fréquentiel (FDFD) et la méthode des différences finies dans le domaine temporel (FDTD). D'abord, un code FDFD bidimensionnel, dédié au calcul de modes propres de guides d'ondes optiques, à été mis en œuvre et testé à travers une comparaison avec des résultats publiés. Dans une deuxième grande partie, nous étudions le piégeage optique de petites particules (de taille microscopique) à l'aide d'une antenne à nano-ouverture papillon (BNA) gravée à l'extrémité d'une sonde de microscope optique métallisée. Le confinement de lumière obtenue à la résonance de la nano-antenne permet un piégeage 3-D des nanoparticules de latex. Une étude systématique à été menée pour quantifier la puissance de la lumière incidente nécessaire pour un piégeage stable. Un bon accord entre les résultats expérimentaux et numériques à été obtenu dans le cas d'une BNA opérant dans l'eau à $\lambda = 1064$ nm pour le piégeage de particules de latex de 250 nm de rayon. En outre, les résultats numériques pour de plus petites particules sont présentés et montrent qu'une telle configuration est capable de piéger des particules avec des rayons aussi petits que 30 nm. Troisièmement, nous avons étudié le processus de piégeage optique basé sur l'amélioration du confinement, non seulement du champ électrique comme dans le cas de la BNA, mais aussi du magnétique que peut exhiber l'antenne métallique type diabolos (DA). Cette dernière à été récemment proposée car elle présente une résonance avec un fort confinement magnétique. Nous avons amélioré le design afin qu'une double résonance, électrique et magnétique, ait lieu au centre de la nano-antenne. Ce double confinement à ensuite été exploité pour exalter le gradient de champ au voisinage de l'antenne et ainsi aboutir à de meilleures efficacités de piégeage (moins puissance). De plus, les résultats des simulations montrent que le processus de piégeage dépend fortement des dimensions des particules et que, pour des géométries particulières, un piégeage sans contact peut être réalisé. Cette structure doublement résonnante ouvre la voie à la conception d'une nouvelle génération de nano-pinces optiques à forte efficacité.

Mots-clés : FDFD, Mode propre, Guide d'onde, FDTD, Force optique, Piégeage optique, Nano ouverture, BNA, DA, Double résonance, Piégeage à la distance.

Abstract:

This thesis is a set of work and reflections on modeling the experiments in nano-optics by using the finite difference method in the frequency domain (FDFD), and in time domain (FDTD). First, a two-dimensional code FDFD, dedicated to the calculation the eigenmodes of optical waveguides, has been implemented and tested through a comparison with results found in the literature. In a second large part, we study the optical trapping of small particles (of microscopic size) by using a bowtie nanoaperture antenna (BNA) engraved at the end of a metal-coated near-field optical microscope tip. The confinement of light obtained at the resonance of the nano-antenna allows 3-D trapping of latex nanoparticles. A systematic study was conducted to quantify the power of incident light necessary for stable trapping. Good agreement between the experimental and numerical results was obtained in the case of a BNA operating in water at $\lambda = 1064$ nm for the trapping of latex particles having a radius of 250 nm-radius. In addition, numerical results for smaller particles are presented and show that such configuration is capable of trapping particles with radii reaching 30 nm. Third, we studied the optical trapping process based on improved confinement of the electric field as in the case of the BNA, but also of the magnetic field, by using a metallic diabolos shape antenna (DA). This latter has been recently proposed because it exhibits resonance with a strong magnetic field confinement. We have improved the design in such a way that a double resonance, electric and magnetic, takes place in the center of the nano-antenna. This dual confinement was then used in order to enhance the field gradient in its vicinity and thus obtain better efficiencies of the trapping (less power). In addition, the simulation results show that the trapping process is greatly dependent of the particles size, and also show that, for specific geometries, a trapping without contact can be achieved. This doubly resonant structure opens the way to the conception of a new generation of optical nano-tweezers with high efficiency.

Keywords: FDFD, Eigenmode, Waveguide, FDTD, Optical force, Optical trapping, Nanoaperture, BNA, DA, Double resonance, Trapping at distance